Dutch Offshore Wind Atlas applications for wind energy purposes

Giel Kerkhofs

TUDelft Delft University of Technology
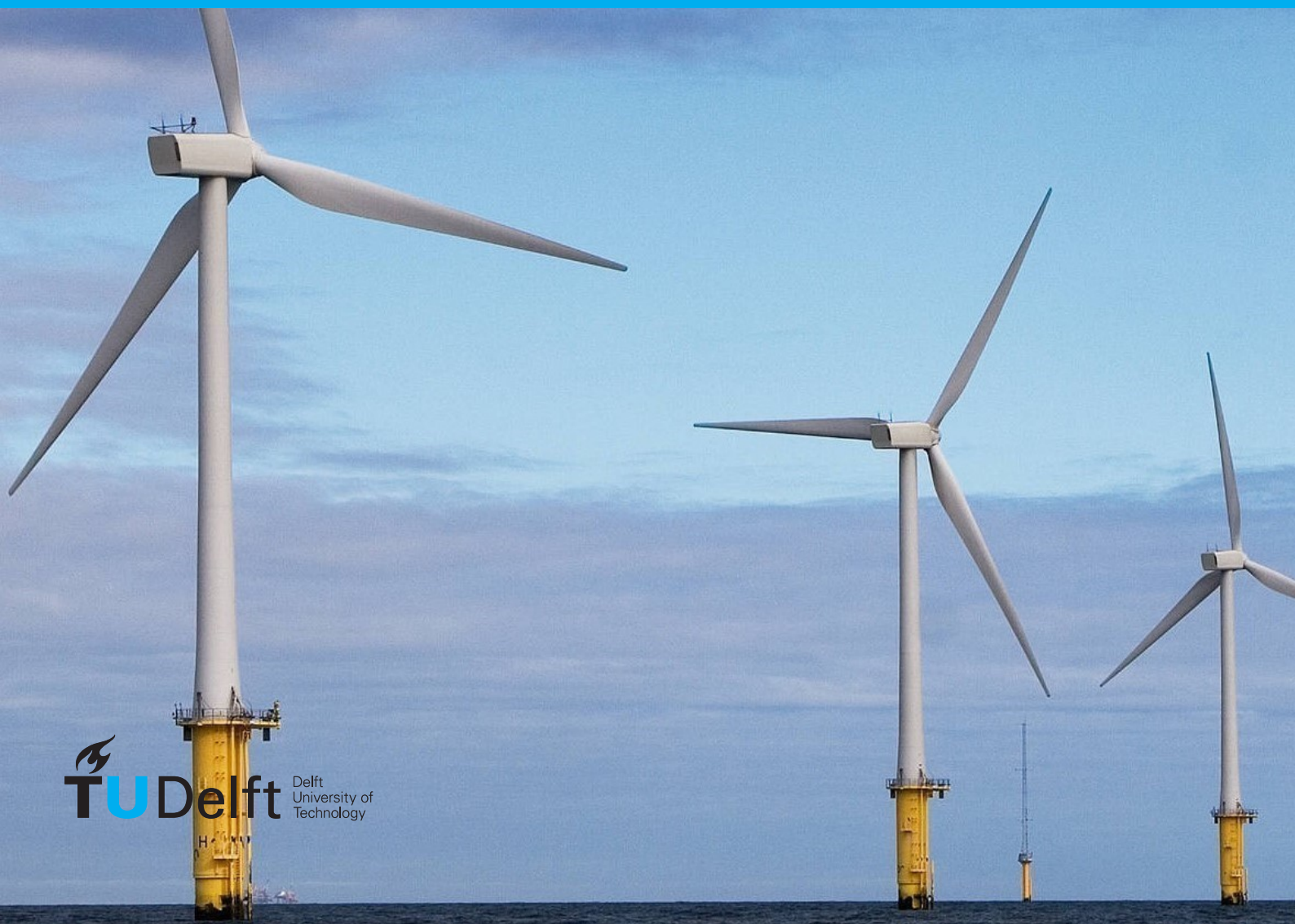
Dutch Offshore Wind Atlas applications for wind energy purposes

by

Giel Kerkhofs

to obtain the degree of Master of Science

at the Delft University of Technology

TUDelft

Acknowledgements

Writing my thesis during these challenging times would not have been possible without the help of some important people. I was fortunate enough to be able to write my thesis from home, surrounded by my family and girlfriend. They provided the support and environment I needed to focus on my thesis work.

I would like to thank Dr. Wim Bierbooms for his flexibility, expertise and guidance throughout my project. His feedback and ideas were not only interesting to discuss, but added a lot of detail to this report. Other people that contributed to the work are Dr. Michiel Zaaijer and prof. Simon Watson, whose feedback and ideas provided a fresh look on the subject, resulting in more detailed and interesting analyses. Additionally, this project would not have been possible without the people at KNMI who worked on the DOWA and researchers at Whiffle who provided the LES model for the DOWA. The measurement data for the validation was kindly provided by Wind @ Sea.

Giel Kerkhofs
Delft, May 2021

Contents

Nomenclature

Physics constants

ϵ	Ratio of molecular weight of water vapor and dry air	0.622
κ	Poisson constant	0.2854
ρ_0	Reference density of air	$1.225\frac{kg}{m^3}$
C_p	Specific heat of dry air at constant pressure	$1006\frac{J}{kg \cdot K}$
g	gravitational acceleration	$9.81\frac{m}{s^2}$
k	Von Kármán constant	0.4
p_0	Reference pressure	$1bar$
R_d	Specific gas constant of dry air	$287.058\frac{J}{kgK}$

Variables

α	Wind shear exponent	—
$\bar{\theta}$	average potential temperature	K
$\bar{U}$	Mean wind speed	$\frac{m}{s}$
η	Efficiency	—
$\frac{\partial s}{\partial x}$	Slope of hill	—
$\frac{dw}{dt}$	Vertical acceleration	$\frac{m}{s^2}$
ψ	Logarithmic stability correction function	—
ρ	Density of air	$\frac{kg}{m^3}$
σ	Stress	MPa
σ_u	Standard deviation of wind speed	$\frac{m}{s}$
σ_e	Equivalent zero-mean alternating stress	MPa
σ_m	Mean stress	MPa
σ_{ult}	Ultimate stress	MPa
θ	Potential temperature	K
θ_v	Virtual potential temperature	K
A	Rotor swept area	m^2
a	Weibull scale parameter	$\frac{m}{s}$
B	Buoyant force	N

b	S-N curve slope parameter	$-$
C	maximum stress	MPa
C_p	Power coefficient	$-$
D	Fatigue damage	$-$
E	Energy yield	GWh
e	Dimensionless energy yield	$-$
FF_{20}	Wind speed at height of $20m$	$\frac{m}{s}$
$FF_{h,c}$	Corrected wind speed at height h	$\frac{m}{s}$
FF_h	Wind speed at height h	$\frac{m}{s}$
H	Sensible heat flux	$\frac{J}{m^2 s}$
hur	relative humidity variable DOWA	$-$
I	Second area moment of inertia	m^4
I_{ref}	Reference turbulence intensity	$-$
k	Weibull shape parameter	$\frac{m}{s}$
L	Obukhov length	m
l	length	m
$L_{gradient}$	Obukhov length estimated through gradient Richardson number	m
lat	latitude variable DOWA	$\circ$
lon	longitude variable DOWA	$\circ$
M	Bending moment	Nm
m	Wind shear exponent	$-$
N	Number of load cycles until failure	$-$
n	Number of experiences load cycles	$-$
p	Air pressure	Pa
R	Rotor radius	m
r_v	Mixing ratio	$-$
Ri	Richardson number	$-$
S_a	Stress amplitude	MPa
T	Absolute temperature	K
T	Number of hours	$-$
T_v	Absolute virtual temperature	K
ta	air temperature variable DOWA	K
TI	Turbulence intensity	$-$
U	Wind speed	$\frac{m}{s}$

$U_0(l)$	Wind speed at height l above the hill	$\frac{m}{s}$
U_R	Wind speed at hub height	$\frac{m}{s}$
u_*	Friction velocity	$\frac{m}{s}$
U_{ci}	Cut-in wind speed	$\frac{m}{s}$
U_{co}	Cut-out wind speed	$\frac{m}{s}$
U_{ref}	Reference wind speed	$\frac{m}{s}$
$wdir$	wind direction variable DOWA	$\circ$
$wspeed$	wind speed variable DOWA	$\frac{m}{s}$
x	Dimensionless wind speed	$-$
x_R	Dimensionless wind speed at hub height	$-$
x_{ci}	Dimensionless cut-in wind speed	$-$
x_{co}	Dimensionless cut-out wind speed	$-$
y	Distance to neutral axis	m
z	Height	m
z'	Validity height of Obukhov length	m
z_R	Hub height	m

Acronyms

ASCAT Advanced Scatterometer

CFD Computational Fluid Dynamics

DOE/MSU Department of Energy/Montana State University

DOWA Dutch Offshore Wind Atlas

ECMWF European Centre for Medium-Range Weather Forecasts

EPL Europlatform

ERA ECMWF re-analysis

FAST Fatigue, Aerodynamics, Structures and Turbulence

FINO1 Forschungsplattform in Nord- und Ostsee Nr. 1

GRASP GPU-Resident Atmospheric Simulation Platform

HARMONIE HIRLAM ALADIN Research on Mesoscale Operation NWP in Euromed

HKN Hollandse Kust Noord

HKZ Hollandse Kust Zuid

IEC International Electrotechnical Commission

KNMI Koninklijk Nederlands Meteorologisch Instituut

KNW KNMI North Sea Wind

LEG Lichteiland Goeree

LES   Large Eddy Simulation

LiDAR Light Detection and Ranging

LLJ   Low level jet

MMIJ   Meteomast IJmuiden

NEWA   New European Wind Atlas

NORSEWInD Northern Seas Wind Index Database

NREL   National Renewable Energy Laboratory

NTM   Normal Turbulence Model

NWP   Normal Wind Profile

NWP   Numerical Weather Prediction

OWA-NEEZ Offshore Wind Atlas of the Netherlands' Exclusive Economic Zone

OWEZ   Windpark Egmond aan Zee

TNO   Nederlandse organisatie voor Toegepast-Natuurwetenschappelijk Onderzoek

WAsP   Wind Atlas Analysis and Application Program

WRF   Weather Research and Forecasting

List of Figures

List of Tables

Executive summary

The installed offshore wind energy capacity in Europe has been increasing rapidly over the past years, this trend is expected to continue thanks to the European green deal. In order to meet the future energy demand, new wind energy solutions such as increasing wind turbine size but also floating structures are being developed. This means that stability phenomena and their effects on wind turbine fatigue and energy yield are becoming increasingly important.

The aim of this thesis project is to define and quantify the applications and limitations of the Dutch Offshore Wind Atlas for wind energy purposes by using it to calculate the energy yield and fatigue damage of two reference wind turbines at multiple locations in the North Sea, with special attention for atmospheric stability.

Theory overview

The Dutch Offshore Wind Atlas (DOWA) project ran from July 2017 until December 2019, although new data is still being generated to add to the dataset. The atlas uses ERA5 reanalysis data as input for the HARMONIE model developed by the KNMI in order to simulate data on a $2.5km$ by $2.5km$ grid. One of the main focus points of the DOWA project were wind energy applications, which is why an LES model was nested in HARMONIE to more accurately model the regions around wind farms with a temporal resolution of 10 minutes.

The atmospheric stability can be quantified using the potential temperature at two heights, or the wind shear exponent based on the wind speed at two different heights as input. A third atmospheric stability parameter is the Obukhov length. This parameter is calculated through the Richardson number, which takes as input the wind speed and virtual potential temperature at two heights. The turbulence intensity is also an important stability parameter. Related to stability is the low level jet phenomenon, this can have severe consequences on the loading of a wind turbine. When calculating the annual energy yield of a wind turbine, it is important to correct the wind speeds for air density, wind shear and turbulence intensity as these parameters all affect the energy yield. Especially for wind turbines with large diameters, wind shear can become a significant source of error when only the wind speed at hub height is used. For fatigue calculations, the most important aspects to consider are the effects of the rainflow counting algorithm, the limitations of Miner's rule and finding the correct material properties. These material properties are of importance when trying to read the fatigue life off an S-N curve or a Goodman diagram. When calculating fatigue damage, the IEC standards always have to be taken into account. This is already partially implemented in FAST, the simulation tool used to obtain the time domain loads on the reference wind turbines.

Description of the dataset

The following variables are of importance for the calculations in this project: wind speed, wind direction, temperature, pressure, humidity and wind speed standard deviation. The latter is not available in DOWA. The DOWA data is available for 17 heights ranging from $10m$ to $600m$ for $234x217$ grid point. Measurement data is used for the locations of Borssele and HKZ using buoy measurements with a floating LiDAR. For the MMIJ location, met mast data is used.

Method

The analyses in this report will be performed for both the NREL $5MW$ offshore reference turbine and the IEA $15MW$ offshore reference turbine. A low level jet is identified when the absolute and relative difference between the maximum and minimum wind speed above and below the maximum wind speed is $0.5\frac{m}{s}$ and 5%, respectively. Then, the wind shear exponent can be calculated by fitting a power law to the vertical

wind speed profile for each simulation hour. The instances at which a LLJ occurs or where the power law fit has an error larger than 5% are excluded from the results. The Obukhov length takes both the wind speed and virtual potential temperature as input. Again, the low level jets are excluded. The temperature profile approach does not exclude low level jets, but assigns a score to each temperature change with height. Based on the sum of the scores, the profile is then classified as stable, neutral or unstable. Finally, turbulence intensity is calculated for the three wind farm locations based on LES outputs of wind speed mean and standard deviation. The method used to calculate the annual energy yield of a wind turbine is shown in the form of a flowchart in figure 1 while the method used to calculate fatigue damage is visualised in figure 2.
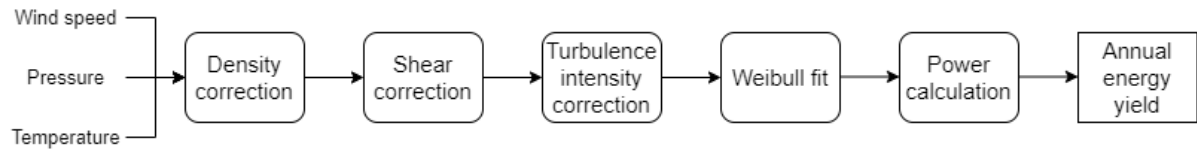
Figure 1: Method used to calculate the annual energy yield of a wind turbine
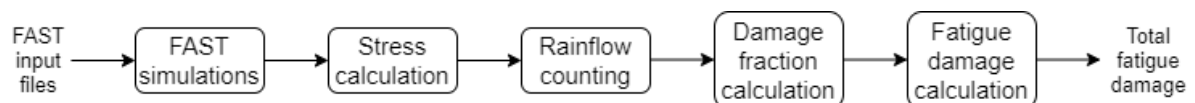
Figure 2: Method used to calculate the lifetime fatigue damage of a wind turbine

Results and validation

The results and validation for the $5MW$ reference turbine are shown in table 1 and table 2 for energy yield and fatigue, respectively.

Table 1: Validation of 5MW turbine energy yield results

Location	Parameter	Site measurements	DOWA 1 hour values	LES 10 minute values	DOWA/ measurements	LES/ measurements
Borssele	a [-]	10.7	10.5	10.1	0.98	0.95
	k [-]	2.1	2.1	2.0	1.01	0.93
	Energy yield [GWh]	23.7	23.1	21.8	0.98	092
HKZ	a [-]	9.8	9.8	9.7	1.00	0.99
	k [-]	2.2	2.2	2.1	0.98	0.96
	Energy yield [GWh]	21.3	21.3	20.7	1.00	0.97

Table 2: Validation of 5MW turbine energy fatigue results

Location	Parameter	Site measurements	DOWA 1 hour values	LES 10 minute values	DOWA/ measurements	LES/ measurements
Borssele	Edgewise fatigue damage	2.5354e-10	2.4564e-10	1.7985e-10	0.97	0.71
	Flap-wise fatigue damage	1.9075e-11	1.7036e-11	2.6675e-13	0.89	0.01
HKZ	Edgewise fatigue damage	2.1292e-10	2.1227e-10	1.6448e-10	1.00	0.77
	Flap-wise fatigue damage	1.0453e-11	1.0914e-11	1.2485e-13	1.04	0.01

Conclusions and recommendations

The DOWA has many applications for wind energy such as a comparison of locations across the North Sea to determine potential new wind farm sites. It can also be used to obtain a first estimate for the energy yield of a wind turbine or wind farm, or to get a general idea of the required wind farm lay-out to limit wake losses.

However, there are some limitations regarding the atmospheric stability and fatigue analysis that should be addressed before being able to get accurate results. Additionally, the full ten years of data should be included in the analyses and turbulence intensity values should be made available in the DOWA.

1

Introduction

Over the past 10 years, Europe's installed offshore wind turbine capacity has increased from $2GW$ to $22.1GW$ and it is expected to rise even more in the coming years. Of this total capacity, 77% ($16.9GW$) is installed in the North Sea. With this upward trend of installed capacity, the size of turbines and wind farms is increasing as well. The yearly average of the rated power of the newly installed wind turbines was $7.8MW$ in 2019, while this was only $3MW$ 10 years earlier. In terms of wind farm size, the capacity of a wind farm almost doubled from $313MW$ in 2010 to $621MW$ in 2019. The largest wind farm constructed in 2019 is the Hornsea One farm in the UK, with a $1.2GW$ capacity containing 171 turbines with a rated power of $7MW$ each [1]. Other trends in the offshore wind energy industry are the fact that wind farms move further from the coastline and the cost of energy is reducing. These trends are expected to continue over the next years as a consequence of the European green deal. In the green deal, special attention is paid to offshore renewable energy. The current plan is to increase the installed offshore wind capacity to $60GW$ by 2030 and $300GW$ by 2050 [2]. To achieve this, the European commission recommends complementing traditional wind energy with other technologies like floating wind energy. Floating wind energy is seen as the solution to build wind farms in far offshore locations that cannot be utilised by traditional bottom-fixed wind turbines due to large depths and soil conditions. With this development of floating wind energy, vertical axis wind turbines are actively being researched [3].

Although these trends are beneficial for the transition to green energy, they also pose some engineering challenges. First of all, the utilisation of floating wind turbines means more locations become available for a potential wind farm to be installed. These locations tend to be further offshore, meaning more data is needed in order to design these turbines and wind farms. Secondly, research on these floating applications has revealed the potential of vertical axis wind turbines. This type of wind turbine is more susceptible to fatigue, meaning fatigue can become a design driver [3]. This increases the need for accurate fatigue calculations. Thirdly, the increasing size of wind turbines and even technological advances in non-traditional forms of wind energy like kite power requires data at larger altitudes than meteorological masts in the North Sea can currently capture. Finally, the offshore environment tends to differ from the onshore environment in terms of stability. This is why special attention should be paid to its effect on wind turbines and the wind conditions in general.

For these design problems, extensive research is performed and models exist to perform accurate calculations regarding atmospheric stability, fatigue and energy yield. The problem is that these models need inputs for atmospheric conditions such as wind speed and turbulence intensity that match as closely as possible the conditions that will be encountered during the wind turbine lifetime. This data can be obtained by performing site measurements or other sources like wind atlases. Performing site measurements is expensive and can only cover a limited area in order to remain accurate. Many wind atlases exist, like the DOWA (Dutch Offshore Wind Atlas) and the NEWA (New European Wind Atlas). These atlases are relatively new but could have some important wind energy applications.

This thesis project aims to define and quantify the applications and limitations of the Dutch Offshore Wind Atlas for wind energy purposes by using it to calculate the energy yield and fatigue damage of two reference wind turbines at multiple locations in the North Sea, with special attention for atmospheric sta-

bility. The results of this analysis will then be validated against site measurements at multiple locations in order to draw conclusions on the accuracy and applicability of the DOWA.

In order to achieve this goal, an overview of the theory that will be used throughout the thesis work will be given in chapter 2. An overview of the datasets used for the analyses is provided in chapter 3. Once the theory and data is discussed, a method will be described for the analysis of the data. This method can be found in chapter 4 and is divided into three sections corresponding to the methods for atmospheric stability analysis, energy yield analysis and fatigue analysis. The results obtained with these methods are presented in chapter 5 and are primarily focused on the DOWA. Chapter 6 will then discuss the validation of these results against site measurements. Finally, the main conclusions and recommendations will be summarised in chapter 7.

2

Theory overview

This chapter will provide an overview of the theory that is used in the analyses that were performed during the research. In section 2.1, some of the most relevant North Sea wind atlases will be outlined. The chapter will then continue with a summary of the theory used for the atmospheric stability analysis in section 2.2 and related to this stability analysis, low level jets will be discussed in section 2.3. The theory behind the energy yield and fatigue analyses can be found in section 2.4 and section 2.5, respectively. Finally, as an extension on the theory behind fatigue, FAST will be discussed in section 2.6. In this section, the simulation tool will be summarised that will be used for the fatigue analysis.

2.1. North Sea Wind Atlases

In this section, an overview is given of wind atlases that cover the North Sea. The KNW (KNMI North Sea Wind) atlas will be discussed in subsection 2.1.1 while an overview of the DOWA (Dutch Offshore Wind Atlas) will be given in subsection 2.1.2. The section will conclude with the NEWA (New European Wind Atlas) in subsection 2.1.3. Several other wind atlases exist like the OWA-NEEZ (Offshore Wind Atlas of the Netherlands' Exclusive Economic Zone) or the NORSEWInD (Northern Seas Wind Index Database), but the three atlases discussed in the section are considered sufficient to present an overview of the state-of-the-art on this topic.

2.1.1. KNMI North Sea Wind Atlas

Figure 2.1 shows the flowchart of the KNW atlas. First of all, the ERA-Interim re-analysis data is obtained using global measurements. In this case, data is used of over 40 years. This gives a dataset with a resolution of $80km$ by $80km$ for each 6 hour period. This data is used to initialise the HARMONIE model, which outputs hourly data on a $2.5km$ by $2.5km$ grid. After that, the outputs of HARMONIE are checked with measurements from the Cabauw meteorological mast and it was found that the vertical shear of the horizontal wind speed is underestimated by about 15% in the HARMONIE model. This is corrected which then gives the final data to be used for the KNW atlas [4].
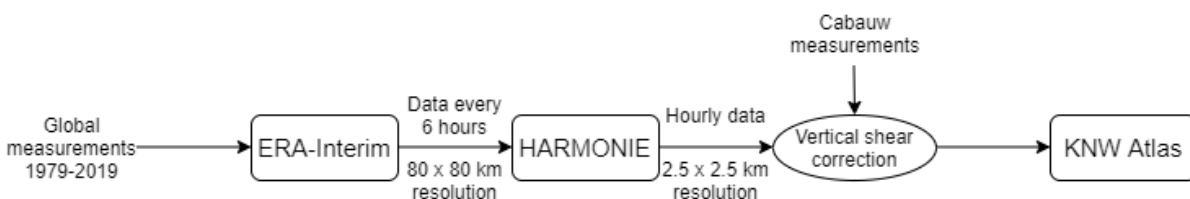
Figure 2.1: Flowchart of KNW atlas

3

This flowchart will be discussed in more detail in the following subsections. These subsections will discuss the domain and grid of the KNW atlas as well as the ERA-Interim dataset it uses as input. Furthermore, the HARMONIE model will be presented as well as a brief description of the dataset. This subsection will conclude with the validation of the KNW atlas.

Domain and grid

The KNW atlas is a wind atlas that covers the part of the North Sea starting at the Dutch and Belgian coastline and going north. This is shown in figure 2.2 with the enlarged version of the resolved atlas in figure 2.3. The blue square is the domain of HARMONIE, the weather forecasting model used in this atlas. The coloured domain is the domain of which the values are actually used for the analysis. The reason why the domain of HARMONIE is so much larger is to reduce the error in the initialisation.

Figure 2.2: Domain of HARMONIE and KNW atlas [5]

Figure 2.3: Mean wind speed output of the KNW atlas [4]
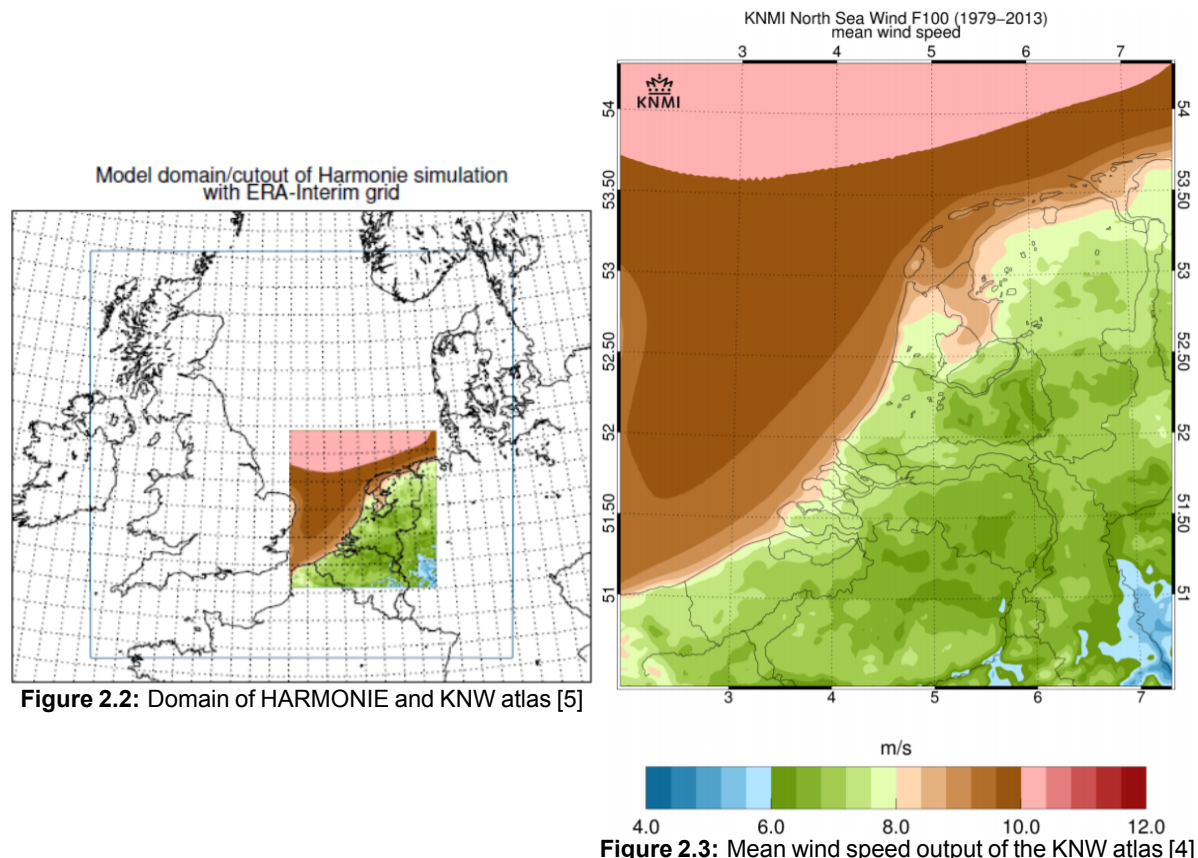
The ERA-interim reanalysis data has a grid with a resolution of $80km$ by $80km$ while the HARMONIE model has a resolution of $2.5km$ by $2.5km$. Because of this, the ERA-Interim data is used to initialise the HARMONIE model. This model is then run in order to give results with a resolution of $2.5km$ by $2.5km$. The output is a three-dimensional domain, meaning the results also vary with height. In the KNW atlas, 60 vertical grid points are available [5].

ERA-Interim

The basis of this atlas is ERA-Interim reanalysis data that is used to initialise the HARMONIE model. ERA-Interim is a reanalysis containing data from 1 January 1979 until 31 August 2019. This means that over 40 years of data can be accessed. A reanalysis describes the atmospheric state based on measurements and models that account for multiple factors including laws of physics [5][6]. The ERA-Interim project was stopped in August 2019 and replaced by ERA5. More information about this will be given in subsection 2.1.2 where the Dutch Offshore Wind Atlas (DOWA) will be discussed.

ERA-Interim is a global reanalysis released by the ECMWF (European Centre for Medium-Range Weather Forecasts). This reanalysis project was created to replace the ERA-40 reanalysis with ERA5, where ERA-Interim was used to prepare for this new project as an intermediate step [7]. The data that is of interest for this paper are the upper-air parameters, which are available for every six hour period. This is of interest since this limits the HARMONIE model, meaning it has to run for at least a six hour period before it can again be initialised with new data from ERA-Interim. However, surface parameters are also available for every three hour period.

The main goal of ERA-Interim was to improve the data assimilation with respect to the use of satellite data, as there were some problems in this regard during the ERA-40 project. ERA-Interim proved to be a significant improvement over ERA-40.

HARMONIE

The HIRLAM ALADIN Research on Mesoscale Operation NWP in Euromed (HARMONIE) model, also known by the name AROME, is a non-hydrostatic Numerical Weather Prediction (NWP) model used for mesoscale predictions, it has been used by the KNMI since 2012 [8][5].

Without going into the equations in too much detail, a NWP model aims to solve seven equations, the so-called equations of motion. Three of these equations describe the conservation of momentum (in three directions of the Cartesian coordinate system). There is also an equation for conservation of heat, conservation of moisture and conservation of mass. These six equations all describe a change in time of a certain variable based on input variables. That leaves one equation that does not change in time; the ideal gas law [9]. It was mentioned that HARMONIE is a non-hydrostatic NWP model. 'Non-hydrostatic' means that the hydrostatic approximation is not used and the full vertical momentum equation is solved. In a hydrostatic model, the full vertical momentum equation would be simplified by removing the total derivative $\frac{dw}{dt}$. This filters out vertically propagating acoustic waves such that a larger time step can be used. As the HARMONIE model does not use this simplification, it is computationally more expensive than a hydrostatic model [10].

Solving the seven equations of motion cannot be done analytically, since these equations are coupled, meaning they have to be solved simultaneously. That is why a numerical computer model is used. This model approximates the equations of motion by a numerical solution. It does this by first dividing the domain into grid cells. These are 'boxes' with a finite volume, within a cell one averaged value is calculated to represent the state in the box. The numerical model then steps through time with a finite time step, trying to find a solution for the numerical approximations of the equations of motion for every grid cell in the domain. An issue here is that the numerical solutions are based on an equilibrium with neighbouring cells and some information is needed about the initial state of the system. This means that boundary conditions and initial conditions have to be specified in order for the NWP model to start the numerical run. In the HARMONIE model used for the KNW atlas, these boundary and initial conditions come from ERA-Interim reanalysis data.

The HARMONIE model divides the domain into grid cells of $2.5km$ by $2.5km$ with a certain height. Then, it calculates a volume-averaged wind speed for every grid box. After a six hour period is simulated, the model is initialised with new ERA-Interim data, this is known as a 'cold start'. This means that for every six hour period, data is generated based on boundary conditions without taking into account the final value of the previous six hour period.

It was found that the HARMONIE model, just like the ERA-Interim data and most modern weather forecasting models, overestimates the vertical mixing of the wind especially under stable atmospheric conditions. This means that the increase of wind speed with height is underestimated. That is why a wind shear factor is reduced by 15% in the HARMONIE model. Equation 2.1 gives the formula that is used for this correction. In the equation, FF_{20} is the wind speed at a height of $20m$, FF_h is the wind speed at height h and $FF_{h,c}$ is the corrected wind speed at height h. Figure 2.4 shows a graph of the wind speed before (red dots) and after (blue squares) the shear correction is applied for a certain location and time. On the graph, the horizontal axis shows the wind speed and the vertical axis represents the height [5].

$$FF_{h,c} = FF_{20} + \frac{FF_h - FF_{20}}{0.85} \tag{2.1}$$
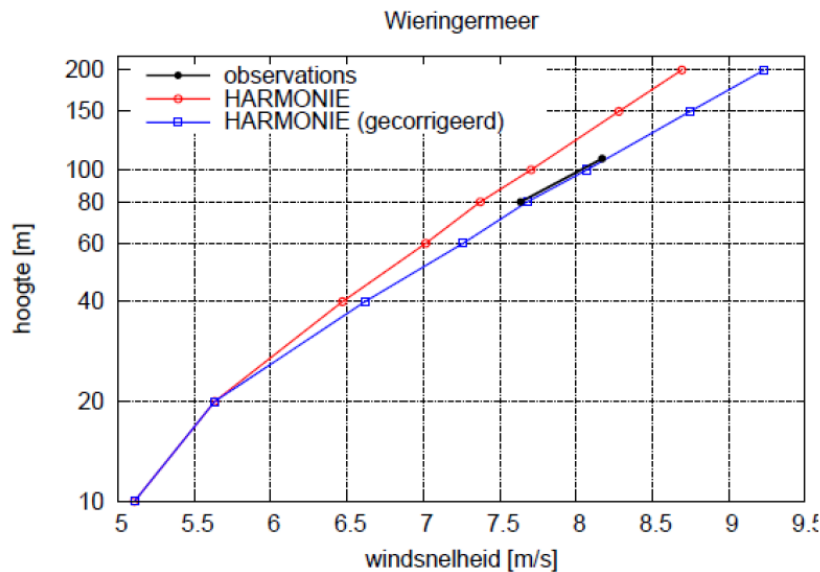
Figure 2.4: Wind speed vs height before and after shear correction [5]

Description of the dataset

As mentioned before, the grid cells of the KNW atlas have a size of $2.5km$ by $2.5km$. The latitude consists of 188 grid cells while the longitude has 170 cells. Each cell contains data for eight different altitudes which are 10, 20, 40, 60, 80, 100, 150 and 200m. This gives a three-dimensional dataset. To make it 4D, data is available for every hour, meaning for every grid cell and every altitude, there are 24 outputs per day per variable. As mentioned earlier, over 40 years of data is available.

Now that the size of the data set is known, the contents of the dataset can be discussed. The variables that are available as output of the KNW atlas are pressure, specific humidity, wind speed, wind direction and temperature.

All data is available on the KNMI data platform. The data itself has already been used to make certain images. Useful images could be the 2D figures for certain altitudes of e.g. Weibull parameters, average wind speed or extremes. Furthermore, wind speed distributions and wind roses can be accessed [4].

Validation

The KNW atlas has been validated extensively. It was validated against the offshore wind masts OWEZ, FINO1 and MMIJ. These are the masts of the Dutch offshore wind park Egmond aan Zee, the German Forschungsplattformen in Nord- und Ostsee and the Meteorological Mast IJmuiden, respectively. Their locations are shown in figure 2.5. Furthermore, some LiDAR measurements were used of both platform-mounted and floating devices.

Because of the volume-averaged values, the values that HARMONIE outputs will vary less than for example an anemometer measurement. This is why anemometer measurements should be averaged over time in order to get comparable results. It was found that the time over which should be averaged is 60 minutes [5]. This means that when comparing a measurement station with a HARMONIE output, the measurements are averaged from 30 minutes before to 30 minutes after the time of the HARMONIE output value. For validation however, the measurements are not averaged. Since HARMONIE outputs one value for every 60 minutes, there are 6 momentary measurements to be compared to every HARMONIE output. When taking the difference between these 10 minute average (momentary) measurements and the HARMONIE values and doing this for a large number of values, the differences will become exactly the same as the difference between the hourly averaged measurements and the HARMONIE output. Note that extreme wind speeds cannot be validated as they are not part of the dataset. This is because a 50-year extreme value would require 50 years of measurements. Instead, these values are extrapolated based on

the available measurements.

It was found that the KNW results for the wind speed error at hub height for all masts and all heights does not exceed $0.2 \frac{m}{s}$. This would mean that long term variables of the KNW atlas such as averages or extremes will be comparable to the measurements [4]. Furthermore, the mean wind speed bias was found to be $1.53 \frac{m}{s}$ [11]. The bias is a measure of magnitude of the difference between the output variables and the validation data. The lower the bias, the more accurate the simulation results.

It was also found that at a height of 10m, the KNW atlas overestimates the wind speeds with $0.3 - 0.4 \frac{m}{s}$ for the northern part of the North Sea, while for the southern part of the North Sea it underestimates the wind speeds by $0.1 - 0.3 \frac{m}{s}$ [5].
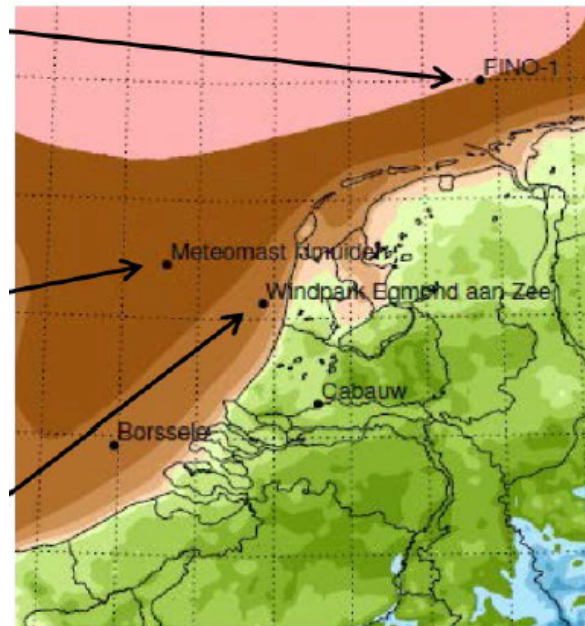
Figure 2.5: Validation mast locations KNW atlas [4]

2.1.2. Dutch Offshore Wind Atlas

The Dutch Offshore Wind Atlas is a project that ran from July 2017 until December 2019. The main goal of the project was to create a wind atlas that was more accurate than the KNW atlas, with special attention to wind energy applications. This was done by using the new version of ERA-Interim, ERA5, of which 11 years of data was used to run the HARMONIE model. In addition to that some changes were made to the HARMONIE model in order to use its full potential. In terms of measurements, some additional measurement platforms were used in the North Sea and some wind energy applications were already included in the project. Even kite power was part of the project, requiring data at larger altitudes. Additional satellite and aircraft measurements were used and low level jets were also part of the DOWA project [11]. The flow chart of the DOWA is shown in figure 2.6.
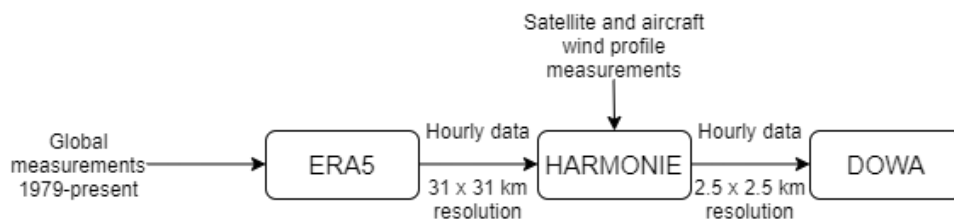
Figure 2.6: Flowchart of the DOWA

The following paragraphs will discuss the domain and grid, the ERA5 input data, the HARMONIE model and some wind energy applications. Validation work that has been performed will be presented as well.

Domain and grid

Figure 2.7 shows a comparison between the domain of DOWA and the KNW atlas. Recall that in the KNW atlas, ERA-Interim data was used corresponding to the green domain. After downscaling with HAR-MONIE, the subdomain that was used in the atlas itself is the blue domain, this was already shown in figure 2.2. In figure 2.7, the domain that DOWA uses in terms of ERA5 data is visualised as a yellow area while the data that was used in the atlas itself is shown in red. It can be seen that the data used to make the DOWA stems from a significantly larger domain, meaning there is a lower chance of initialisation error when the data is downscaled by HARMONIE. Furthermore, the resulting data that can be used for the atlas covers a larger domain. In terms of resolution, not much changes as the resulting grid size is still $2.5km$ by $2.5km$ [11]. A small change is the fact that the resolution of ERA5 is $31km$ by $31km$, while this was $80km$ by $80km$ for ERA-Interim [12].
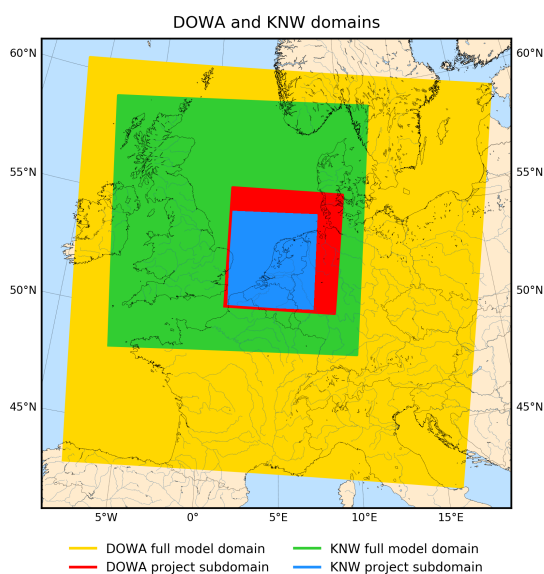
Figure 2.7: Comparison of DOWA and KNW atlas domains [11]

ERA5

ERA5 is the ECMWF's successor of ERA-Interim and thus uses a newer version of the ECMWF Numerical Weather Prediction model. The main differences include a spacial resolution upgrade from $80km$ by $80km$ to $31km$ by $31km$ and an increase in temporal resolution from 6 hours to 1 hour [11] [13] [14]. The ERA5 dataset contains data at 137 altitudes, while there are only 60 altitudes available in the ERA-Interim dataset [13]. It uses data starting from the year 1979 and is updated to 5 days from real time. The ERA-Interim program was stopped at 31 August 2019, at which point it was fully replaced by ERA5 [12].

HARMONIE

In the KNW atlas, HARMONIE was not used at its full potential as ERA-Interim data was used to cold start a HARMONIE simulation every 6 hours. In the DOWA, an updated version of HARMONIE is used (Cycle 40h1.2.tg2). Additional satellite and aircraft wind profile measurements are used for every 3 hour interval in addition to the ERA5 reanalysis data. This improves the output of HARMONIE. The 'cold start' that was used for the KNW atlas is eliminated by making use of the latest forecast of the previous cycle as initial values. ERA5 data is used as boundary condition of the domain for every hour of simulation [13].

Wind energy applications

A major part of the DOWA project was its applications for wind energy. First of all, an LES-model was nested in the HARMONIE model to downscale the data even further. This LES model is called GRASP and was used to simulate the DOWA parameters around three Dutch offshore wind farm locations (Borssele, Hollandse Kust Noord and Hollandse Kust Zuid) on a finer grid and higher temporal resolution. This allows for a more accurate wind farm analysis. To do this, a wind turbine parametrisation is used in GRASP. The power production estimation of wind farms were also considered as an application of the DOWA. This was done using FarmFlow and the OWEZ wind farm was used as a test case [11]. Secondly, the loads on turbines in extreme events like low level jets have been analysed using AeroModule. These low level jet events make it difficult to estimate atmospheric stability and can have an impact on fatigue performance and energy yield. Thirdly, even without the LES nesting the DOWA output can analyse wind farms. More specifically, the output of the HARMONIE model can be used to analyse mesoscale effects of wind farms. In order to do this, a wind farm parametrisation is introduced into the HARMONIE model. This allows for calculations of the wake of wind farms in the North Sea. Finally, data was produced for high altitudes in order to allow not only for analysis of taller wind turbines but also e.g. kite power.

Validation

The DOWA was validated using 10 years of measurements at the Cabauw site using a mast equipped with cup anemometers and wind vanes to measure wind speed and direction. Data is available for six heights ranging from $10m$ to $200m$. It can be seen in figure 2.8 that the results of the DOWA and KNW atlas are very similar and very close to the measurements. Taking into account the accuracy of the measurements of $0.1\frac{m}{s}$, it is assumed that any bias below $0.2\frac{m}{s}$ is insignificant. This means that both the DOWA and KNW atlas have a wind speed bias of almost zero. It can be seen however that at heights of $10m$ and $20m$, the KNW atlas outperforms DOWA. Zooming in on the seasonal variations and the height of $20m$, some bias can be seen in both DOWA and KNW especially during the winter months where the value for the wind speed bias can be as high as $0.5\frac{m}{s}$ as shown in figure 2.9. During these months, DOWA was found to underestimate the wind speed while the KNW atlas overestimates the wind speed, meaning their bias is opposite in sign [15].
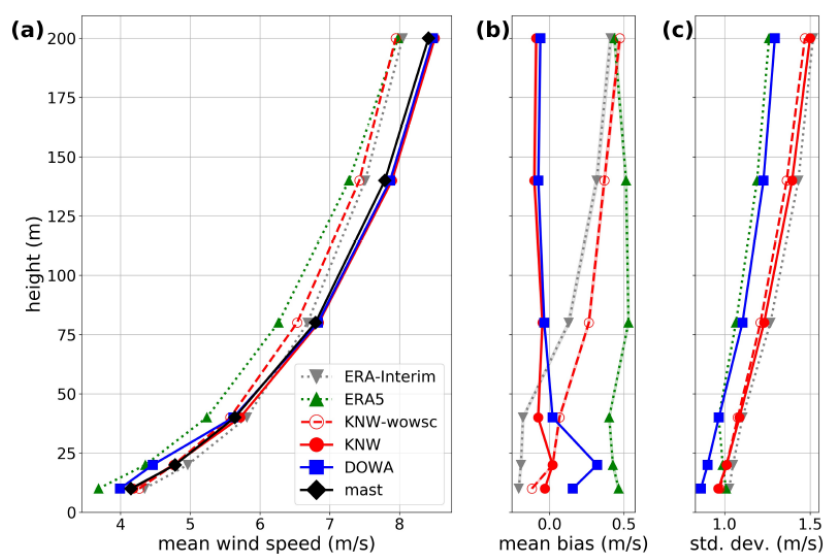
Figure 2.8: Mean wind speed (a),
mean bias (b) and standard deviation of the bias (c) of different models and wind atlases for different heights [15]
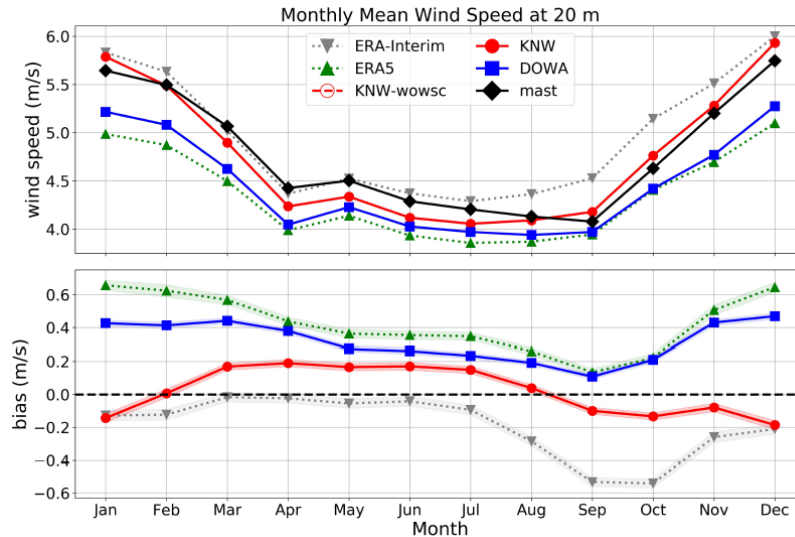
Figure 2.9: Mean wind speed and bias at a height of $20m$ [15]

Table 2.1 shows the wind speed correlation results of the DOWA and KNW atlas by means of a linear regression fit. It can be seen that DOWA performs slightly better than the KNW atlas, especially at higher altitudes, but no significant differences were found [15].

Table 2.1: Correlation results for DOWA and KNW [15]

Height (m)	Slope		Offset (m/s)		R^2	
	DOWA	KNW	DOWA	KNW	DOWA	KNW
10	0.91	0.90	0.20	0.46	0.87	0.84
20	0.88	0.89	0.25	0.48	0.87	0.84
40	0.91	0.92	0.51	0.53	0.87	0.84
80	0.92	0.90	0.55	0.70	0.87	0.84
140	0.93	0.90	0.58	0.90	0.88	0.85
200	0.94	0.90	0.61	0.95	0.90	0.86

The same validation analysis is performed for the wind direction of the DOWA and KNW atlas compared to the Cabauw measurements. It was found that the bias is as large as $-6°$ for lower heights and $-2°$ at larger altitudes. The KNW atlas performs slightly better at the largest heights. Furthermore, it was concluded that DOWA is better at capturing the diurnal cycles than the KNW atlas [15].

In the original DOWA report, some validation was already included as well. In terms of results at the Cabauw meteorological mast, the same conclusions are drawn in the DOWA final report as for the validation report discussed earlier. In the DOWA final report however, LiDAR and meteorological mast measurements were used. These LiDAR measurements were both floating and platform-mounted. This is the same as for the KNW atlas. The DOWA was then further validated using additional Advanced Scatterometer (ASCAT) measurements. For this validation, measurements at 10 different sites are considered [11].

2.1.3. New European Wind Atlas

The New European Wind Atlas (NEWA) is a wind atlas issued by the European commission and it is funded by its participating member states. It is the improved version of the European Wind Atlas that was published in 1989. The flowchart of the NEWA is shown in figure 2.10. The initial and boundary conditions that serve as input for the numerical weather prediction model are the same as for the DOWA, meaning ERA5 reanalysis data is used. The numerical weather prediction model itself is different however. In the NEWA, the Weather Research and Forecasting (WRF) model is used to perform the simulations. Using this model, the temporal resolution of 3 hours from the ERA5 data is downscaled to 30 minutes. The spatial resolution of $31km$ by $31km$ of the ERA5 data is downscaled to three different resolutions, which will be

further explained in the following paragraphs. The outputs of WRF are then further downscaled, reducing the spatial resolution to $50m$ by $50m$ to capture local flow phenomena [16].

Figure 2.10: Flowchart of the NEWA

In the following paragraphs, the domain and grid, WRF model and WAsP model will be discussed in more detail. This is followed by a description of the dataset and an overview of the validation performed on the NEWA.

Domain and grid

The NEWA covers the full domain of Europe as shown in figure 2.11, extending $100km$ from the European coasts to include offshore sites. The resolution of this domain is $27km$ by $27km$, which is the output of the WRF model. The domain has a nested mesh however. A nested mesh is a mesh that has a finer resolution at certain locations. There are five regions that are resolved in a higher resolution, shown by the square regions in the figure. These regions have a resolution of $3km$ by $3km$. Note that there is a larger square region around each high resolution nested region. This is a transition region and has a resolution of $9km$ by $9km$. This is because a nested mesh has an ideal resolution ratio of $1:3$, so the resolution of $27km$ first has to be downscaled to $9km$ and can then be nested to $3km$ according to the ideal ratio. The nesting in this atlas is a one way nest. This means that the coarser mesh is resolved first and the input of this coarser mesh is then used to create the finer mesh. In a two-way nest, the finer mesh would be resolved together with the coarse grid but this is computationally more expensive [9]. This atlas is further downscaled to a $50m$ by $50m$ resolution using a WAsP model, however this data is only available for three different heights: $50m$, $100m$ and $150m$ above ground level and the aim of this microscale model is to incorporate local terrain effects.
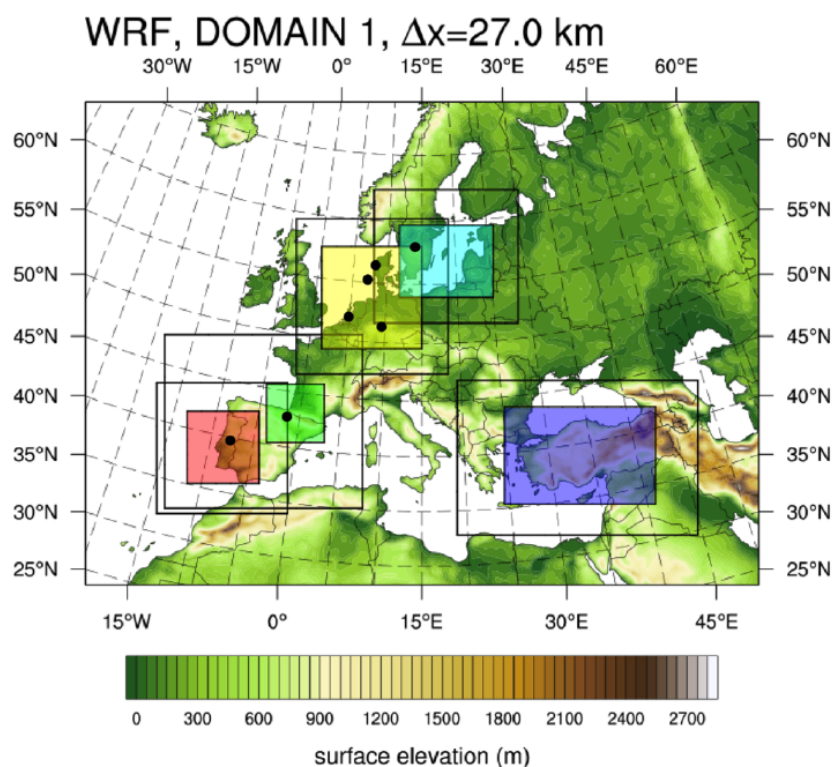
Figure 2.11: Domain of the NEWA [17]

WRF

The numerical weather prediction model that is used to make the NEWA is the Weather Research and Forecasting (WRF) model. Note that in the KNW atlas and the DOWA, HARMONIE was used. This is one of the major differences between the atlases. The WRF model, like HARMONIE, does not use the hydrostatic assumption. The implications of this assumption were already explained in subsection 2.1.1. The original version of the WRF model is slightly modified to fit the needs of the NEWA. For example, some changes were made in the planetary boundary layer scheme and a module for ice accumulations was added to take this phenomenon into account.

The ERA5 data was downscaled through the WRF model by running simulations. ERA5 data was used to initialise the model and to provide boundary conditions after which an 8 day simulation was run. The first day of this simulation is used as a spin-up period, meaning that ERA5 data is still fed into the model during this day in order to nudge the model in the right 'direction', making sure that the model does not drift away from the observed atmospheric patterns. This is important because the model needs some time to reach an equilibrium in order to produce viable data. This spin-up day is then discarded, leaving 7 days of data after a run. Each 7 day period was simulated independently, saving computational time since the full 30 year temporal domain of the NEWA could be simulated simultaneously in 7 day periods (+ 1 spin-up day) [16].

WAsP

WAsP is a linearised flow model that is based on the Jackson-Hunt theory. It is relatively fast to run since it solves the equations of continuity and momentum, but not the energy equation. Its main purpose is to take out small scale terrain effects that cannot be modeled by the relatively large resolution numerical prediction models. Note that the WAsP model is not suitable for complex terrain. If complex terrain features are to be resolved, CFD models are required although they are computationally much more expensive.

The Jackson and Hunt theory behind this WAsP model is a theory that allows the flow over a 2D hill to be solved analytically with linear equations. The theory was then extended by Mason and Sykes to allow for the flow over a 3D hill to be solved. A representation of a 2D hill is shown in figure 2.12. Jackson and Hunt divide the air above the hill into two regions. There is an inner layer for $z < l$ with z the height above the hill. This inner layer is dominated by shear stresses as a result from contact with the surface. The layer for $z > l$ is the outer layer, this is dominated by the pressure gradient and is barely affected by shear forces. The linearised boundary condition given by equation 2.2 is applied. Here, $\frac{\partial S}{\partial x}$ is the slope of the hill where S is the vertical distance and x is the horizontal distance. $U_0(z)$ is the wind speed as a function of height. It is because of this boundary condition that the terrain cannot be too complex. If the hill is too steep, turbulence is created behind the hill since the flow is no longer fully attached, this is where the linear boundary conditions break down. Some linearised equations are then formulated to solve the flow within both the inner and outer layer separately and they are solved after having applied a Fourier transformation [18].
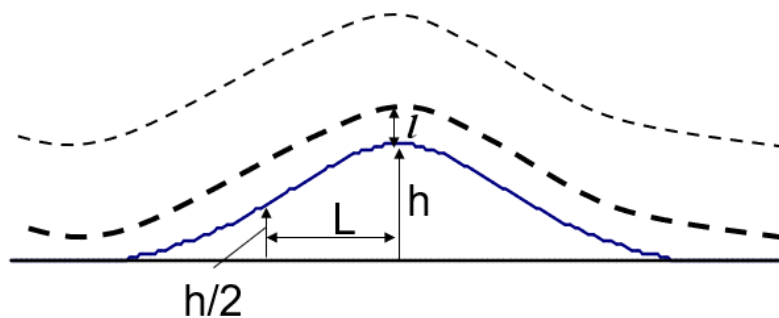
Figure 2.12: Jackson and Hunt theory 2D hill [18]

$$\text{on } z = l: \ w = U_0(l)\frac{\partial S}{\partial x} \tag{2.2}$$

Description of the dataset

The output of the WRF model contains data at 61 different heights. The heights that are relevant to wind energy applications are the 10 lowest: 6, 22, 40, 57, 73, 91, 113, 140, 171 and 205m above ground level. It outputs parameters like wind speed, Weibull parameters, humidity and temperature. As mentioned before, after applying the WAsP model to resolve the microscale phenomena, only three heights remain at which data is available: 50, 100 and 150m. Only the wind speed, Weibull parameters and air density are available for these microscales. Note that for offshore locations, microscale effects that the WAsP model accounts for do not play a very important role since the terrain is very flat.

Validation

It is difficult to validate the NEWA because compared to the domain of the atlas, there are very few met masts available. Especially in regions with complex terrain additional measurements would be required. Furthermore, the met masts that are available do not cover exactly the same heights and not every mast covers the same period of time as the NEWA which is the period of 1989-2018.

However, measurements of 291 meteorological masts across Europe have been used in an attempt to validate this wind atlas. It makes sense that the error is related to the complexity of the terrain surrounding the mast. It was found that the average wind speed bias is $0.05 \pm 0.49\frac{m}{s}$ for the WRF model while it is $0.28 \pm 0.76\frac{m}{s}$ for WAsP. The ERA5 reanalysis data is slightly less accurate with a mean wind speed bias of $-1.50 \pm 1.30\frac{m}{s}$ [16].

2.2. Atmospheric stability

With this background information on the models behind the wind atlases in mind, the remainder of this chapter will focus more on the theory used to analyse the data of the DOWA, starting with atmospheric stability. Atmospheric stability is an important aspect to consider in any wind energy project, especially offshore. Stability can have significant effects on the power production and fatigue damage of a wind turbine [19]. The most straightforward method to describe atmospheric stability is with a vertical potential temperature profile. The boundary layer is statically stable when the change of potential temperature with height $\frac{\partial \theta}{\partial z} > 0$ and statically unstable when $\frac{\partial \theta}{\partial z} < 0$. For $\frac{\partial \theta}{\partial z} = 0$, the boundary layer is neutral [20].

Different methods have been established to estimate atmospheric stability in the boundary layer. The most relevant stability parameters for wind energy applications are the wind shear exponent, Obukhov length and turbulence intensity. These parameters will be explained in more detail in subsection 2.2.1, subsection 2.2.2 and subsection 2.2.3, respectively. Based on these parameters, the data can be assigned to stability classes in order to provide a more detailed overview of the stability distribution at a specific location [21].

2.2.1. Wind shear exponent

The wind shear exponent is a stability parameter that is used in the power law fit of the vertical wind profile. The power law expression is given by equation 2.3 [20].

$$U(z) = U_R \left(\frac{z}{z_R} \right)^m \tag{2.3}$$

In this equation, $U(z)$ is the wind speed at height z and U_R is the wind speed at height z_R, where z_R is the lowest of both heights. The parameter m is the wind shear exponent. This parameter can be calculated using equation 2.4 when the wind speed at two heights is known.

$$m = \frac{ln\left(\frac{U(z)}{U_R}\right)}{ln\left(\frac{z}{z_R}\right)} \tag{2.4}$$

The value of the wind shear exponent is used to assign a stability class to the measured wind profile, these can be found in figure 2.13. The data from this figure was obtained using Cabauw measurements, making it applicable to the DOWA simulation data as it is centered around the same measurement station.

Pasquill class	Name	Shear exponent range	Typical value of shear exponent
A–C	(very–slightly) unstable	$m \leq 0.1$	0.07–0.10
D	(near) neutral	$0.1 < m \leq 0.2$	0.15
E	slightly stable	$0.2 < m \leq 0.4$	0.35
F	(moderately–very) stable	$0.4 < m$	0.55

Figure 2.13: Stability classes with corresponding shear exponent values [22]

2.2.2. Obukhov length

The Obukhov length L was defined by Monin-Obukhov in 1954, where L is the ratio of mechanical shear forces to thermal buoyant forces. This ratio of shear forces and buoyant forces is parametrised in equation 2.5 [23].

$$L = \frac{u_*^3}{kB} \tag{2.5}$$

In the equation, B is the buoyant force, calculated using equation 2.6. Equation 2.5 and equation 2.6 combine to equation 2.7. Here, u_* is the friction velocity, k is the Von Kármán constant, C_p is the specific heat of dry air, ρ is the air density, T is the absolute temperature, g is the gravitational acceleration and H is the heat flux.

$$B = \frac{gH}{TC_P\rho} \tag{2.6}$$

$$L = \frac{u_*^3 C_P \rho T}{kHg} \tag{2.7}$$

The Obukhov length is used to perform a stability correction to the logarithmic wind profile given by equation 2.8, where $\psi\left(\frac{z}{L}\right)$ represents the stability correction as a function of $\frac{z}{L}$. The parameter z represents the height above the ground and U is the wind speed.

$$U = \frac{u_*}{k}\left[ln\left(\frac{z}{z_0}\right) + \psi\left(\frac{z}{L}\right)\right] \tag{2.8}$$

Figure 2.14 shows the stability classes with corresponding Obukhov length intervals. Note that many different versions of this exist in literature and values should be modified based on the chosen site.

Class name	Class boundaries	Value for load calculations
Very Unstable (VU)	$-200 \leq L < 0$	$L = -100$
Unstable (U)	$-500 \leq L < -200$	$L = -350$
Neutral (N)	$|L| > 500$	$L = 1 \ 10^{10}$
Stable (S)	$200 < L \leq 500$	$L = 350$
Very Stable (VS)	$0 < L \leq 200$	$L = 100$

Figure 2.14: Stability classes with corresponding Obukhov length values [24]

Table 2.2 shows how ψ is calculated as a function of atmospheric stability and elevation relative to the Obukhov length. Note that the Obukhov length is assumed to be a single parameter for a certain location, it does not change with height. In terms of the parameter $\frac{z}{L}$, the atmosphere is stable for $\frac{z}{L} > 0$, unstable for $\frac{z}{L} < 0$ and neutral for $\frac{z}{L} = 0$ since z is never negative. Note again that this table provides one of many stability correction functions that can be found in literature.

Table 2.2: Stability correction function ψ for a given atmospheric stability and elevation relative to Obukhov length [23]

Atmosphere	Stability correction function	z/L
Neutral	$\psi = 0$	
Stable	$\psi = 4.5(z/L)$	$z \leq L$
Stable	$\psi = 4.5[1 + \ln(z/L)]$	$z > L$
Unstable	$\psi = -0.5(z/L)$	$z \leq L$
Unstable	$\psi = -0.5[1 + \ln(z/L)]$	$z > L$

In practise, it is difficult to calculate the Obukhov length based on equation 2.7. This is why an approximation is often used through the Richardson number. The gradient Richardson number is often used to estimate the Obukhov length if data is available for several heights, the formula for this is given in equation 2.9 [25]. It can be seen in the equation that this method uses data at two different heights that contain both wind speed and temperature.

$$RI = \frac{g \Delta \overline{\theta_v} \Delta z}{\overline{\theta_v} (\Delta \bar{u})^2} \tag{2.9}$$

The variable θ_v is the virtual potential temperature. The conversion from absolute temperature to virtual temperature is given by equation 2.10, where r_v is the mixing ratio in units of $\frac{kg}{kg}$ and $\epsilon = 0.622$. The conversion from absolute temperature T to potential temperature θ is given by equation 2.11 [26]. Combining these two equations yields equation 2.12, which gives the conversion from absolute temperature to virtual potential temperature. Here, p_0 is the reference pressure of 1 bar and $\kappa \approx 0.2854(1 - 0.24 r_v)$ is the poisson constant. The factor 0.2854 is the ratio of the gas constant and specific heat of dry air at constant pressure; $\frac{R_d}{c_p}$.

$$T_V = T \frac{1 + \frac{r_v}{\epsilon}}{1 + r_v} \tag{2.10}$$

$$\theta = T \left(\frac{p_0}{p} \right)^\kappa \tag{2.11}$$

$$\theta_V = T \frac{1 + \frac{r_v}{\epsilon}}{1 + r_v} \left(\frac{p_0}{p} \right)^\kappa \tag{2.12}$$

The mixing ratio r_v is the ratio of water vapor mass to the ratio of dry air mass in the air. The mixing ratio can be calculated as the product of the saturation mixing ratio and the relative humidity. The saturation mixing ratio can be looked up in literature as it is a function of temperature while the relative humidity is an output of the DOWA.

Once the gradient Richardson number described in equation 2.9 is obtained, the $\frac{z}{L}$ parameter can be estimated according to equation 2.13. Here, the Richardson number is valid for height $z' = \frac{z_1 - z_2}{ln(\frac{z_1}{z_2})}$ [25].

$$L_{gradient} = \begin{cases} \frac{z'(1-5RI)}{RI} & \text{if } 0.2 \geq RI \geq 0 \\ \frac{z'}{RI} & \text{if } RI \leq 0 \end{cases} \tag{2.13}$$

2.2.3. Turbulence intensity

Turbulence intensity is defined as the ratio of standard deviation of the wind speed to the mean of the wind speed given by equation 2.14, where U is the mean wind speed and σ_U is the standard deviation of the wind speed [20].

$$TI = \frac{\sigma_U}{U} \tag{2.14}$$

2.3. Low level jets

Strongly related to the atmospheric stability topic is the low level jet. A low level jet (LLJ) is an event that occurs when the wind speed reaches a maximum in the lower troposphere. It is usually observed at night under stable atmospheric conditions. There are several different mechanisms that can cause the formation of a low level jet. These mechanisms range from diurnal variations, where stable stratification occurs and the mixed boundary layer decouples from the surface [27]. Another mechanism is a change in surface. For wind energy, usually the difference in surface friction is important due to the development of an internal boundary layer. But the differential heating of these surfaces should also be considered as this can produce strong low level jets. An example of this is a coastal area, where the surface changes from sand to water.

In order to identify a LLJ, certain criteria have to be met. First of all, a maximum wind speed has to occur in the lower part of the boundary layer. Secondly, the wind speeds above and below this maximum wind speed have to be significantly lower. The term 'significantly' can be interpreted in different ways and is largely dependent on the data and the purpose of the research. The threshold can range from a difference of $0.5\frac{m}{a}$ to $2\frac{m}{s}$. Furthermore, a relative difference of e.g. 5% could be specified to avoid mistakes in the identification of LLJs [27].

At Cabauw, which is the center of the DOWA, significantly more LLJs are observed during the summer months. Jet speeds range from $6\frac{m}{s}$ to $10\frac{m}{s}$ and jet heights range from $140m$ to $260m$ [27]. Note that these are results for the Cabauw meteorological mast which is located onshore. For offshore calculations these numbers might differ. The problem of a low level jet is the fact that it makes it harder to quantify stability according to the parameters described in section 2.2. This is because a low level jet wind profile does not follow the logarithmic of power law vertical wind profile. Richardson numbers and corresponding Obukhov lengths or shear exponents calculated during the occurrence of a LLJ will not be valid. Usually under stable atmospheric conditions, the turbulence intensity decreases which has a positive effect on the loads experienced by a wind turbine. But during a LLJ event, significant shear is observed above and below the LLJ height, increasing wind turbine loading. It is therefore important to treat low level jets as a separate class due to their significance for wind energy, because they can occur around hub height. This can have severe consequences for the energy yield and fatigue calculations.

2.4. Energy yield

This section will provide an overview of some of the theory used during the energy yield calculations. Subsection 2.4.1 will discuss the density correction for wind speed, while a correction for wind shear will be discussed in subsection 2.4.2. Finally, an overview of the theory regarding the turbulence intensity correction is given in subsection 2.4.3.

2.4.1. Density correction

The wind speed should be corrected for air density according to equation 2.15. In the equation, U_{norm} is the normalised wind speed, U is the wind speed according to the data and ρ is the density according to the data. The parameter ρ_0 is the reference density of $1.225 \frac{kg}{m^3}$ [28].

$$U_{\text{norm}} = U \cdot \left(\frac{\rho}{\rho_0} \right)^{1/3} \tag{2.15}$$

2.4.2. Wind shear correction

There are several possibilities to correct the power curve for wind shear. Equation 2.16 describes vertical averaging of the horizontal wind speed while equation 2.17 describes the procedure to average the wind speed over the rotor plane. Both methods assume the vertical wind profile follows the power law with shear exponent α [28].

$$U_{\text{avevert}} = \frac{1}{2R} \int_{H-D/2}^{H+D/2} U(z)dz = U(H) \cdot \frac{1}{\alpha+1} \cdot \left(\left(\frac{3}{2} \right)^{\alpha+1} - \left(\frac{1}{2} \right)^{\alpha+1} \right) \tag{2.16}$$

$$U_{\text{averot}} = \frac{1}{A} \int_{H-D/2}^{H+D/2} U(z)dA = U(H) \cdot \frac{2}{\pi} \cdot \int_{-1}^{1} \sqrt{1-y^2} \cdot \left(\frac{1}{2} \cdot y + 1 \right)^{\alpha} dy \tag{2.17}$$

Another option, if a sufficient number of measurements is available, is to use the rotor equivalent wind speed. The formula to calculate rotor equivalent wind speed is given by equation 2.18. It is based on the principle that the rotor swept area is vertically divided into sections. Each section has its own area and wind speed. The rotor equivalent wind speed is then the wind speed at hub height normalised according to energy flux [29].

$$U_{eq} = \sqrt[3]{\frac{1}{A} \left(\sum_i \overline{U_i^3} \cdot A_i \right)} \tag{2.18}$$

2.4.3. Turbulence intensity correction

Equation 2.19 shows the wind speed correction for turbulence intensity, where $TI = \frac{\sigma_U}{U}$ [28]. This expression is obtained from the cubical dependence of power on wind speed. This expression is verified in appendix B using FAST simulations.

$$U_{\text{corr}} = U_{\text{norm}} \cdot \left(1 + 3 \cdot \left(\frac{\sigma_U}{U} \right)^2 \right)^{1/3} \tag{2.19}$$

2.5. Fatigue

Another important aspect to consider in any wind turbine project besides energy yield is fatigue. Since a turbine is a rotating machine operating for 20 years or more, a very high amount of load cycles will be experienced during its lifetime. Wind turbines generally experience low cycle fatigue, meaning a very high number of cycles with a relatively low stress amplitude will occur. The main focus point for wind turbine fatigue is the blades, as they are designed to be as low weight as possible while being a rotating component [30].

2.5.1. Rainflow counting and Miner's rule

The basics of fatigue analysis are rainflow counting and Miner's rule. Usually when assessing fatigue, the input is a series of stresses in time. Figure 2.15 represents how rainflow counting is applied to a larger series of stress values. The algorithm to take out small amplitude cycles is repeated until no more cycles can be removed. That leaves the residue stress spectrum. These are the main load cycles that will be used in the fatigue analysis.
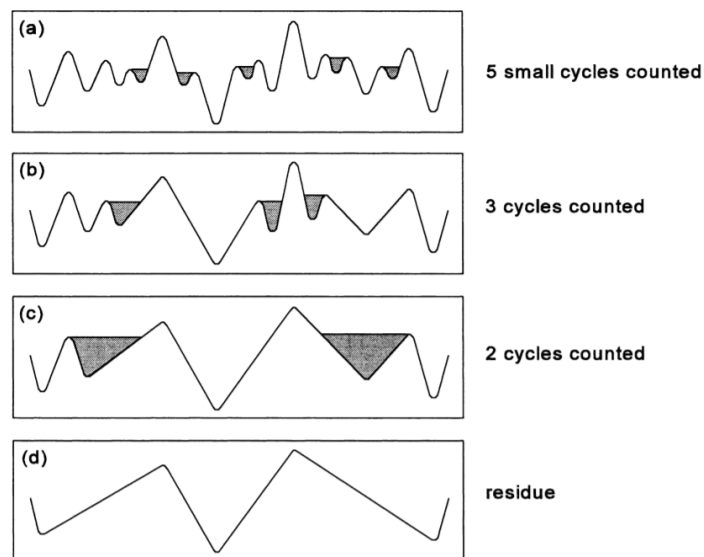
Figure 2.15: Rainflow counting applied to a larger series of stress values [31]

When these load cycles are obtained, the fatigue damage of each load cycle is summed in order to obtain the total fatigue damage. There are several ways to do this, but the most commonly used method is the application of Miner's rule given by $D = \sum \frac{n_i}{N_i}$. Here, D is the total fatigue damage, n_i is the number of cycles experienced by the specimen at a certain stress amplitude and N_i is the number of cycles to failure of the specimen at that stress amplitude.

Like all methods, Miner's rule has its limitations. This rule assumes that partial damage accumulated due to a load cycle with a certain amplitude can be linearly added to the partial damage due to a load cycle with a different amplitude. This is not entirely correct as the partial damage is determined based on tests on a specimen under the application of a constant amplitude load cycle.

Consider figure 2.16, where a variable amplitude load spectrum is shown. The specimen experiences load cycles until failure, where the first half of the cycles has a larger amplitude than the second half. According to Miner's rule, $\frac{n_1}{N_1} + \frac{n_2}{N_2} = 1$ is true for this case, as the sum of the partial fatigue damages should equal one in case of failure.
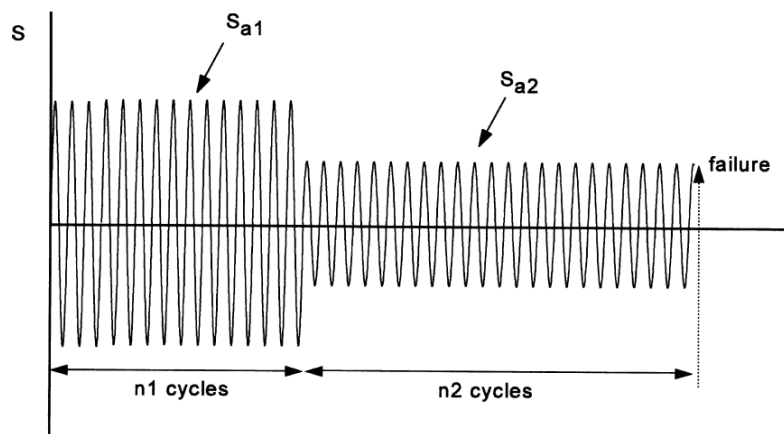
Figure 2.16: Variable amplitude load spectrum [31]

If now S_{a_2} is considered to be below the fatigue limit, the material should never fail according to Miner's rule due to the fact that $\frac{n_2}{N_2} = \frac{n_2}{\infty} = 0$. In reality this proves to be inaccurate because the value of $N_2 = \infty$ comes from constant amplitude testing and is based on the fact that a crack cannot be initiated below the fatigue limit. However, a crack may have already initiated under the loading amplitude of S_{a_1}, meaning the crack can still grow under the loading amplitude of S_{a_2}, but no new cracks will be initiated. This crack growth during the second half of the cycles when a load amplitude below the fatigue limit is applied is completely neglected in Miner's rule, which is why this rule underestimates the fatigue damage in case of variable amplitude loading. This means that the material will fail at $D < 1$ as calculated by Miner's rule [31].

Another limitation to consider for the application of Miner's rule is the effect of notch root plasticity. Consider again figure 2.16 but in this case, S_{a_1} is below the ultimate strength but above the yield strength of the material and S_{a_2} is below the yield strength but above the fatigue limit of the material. In this case, a load above the yield strength is applied first, meaning there will be plastic deformation of the material. A consequence of this is the presence of plasticity during the application of smaller amplitude load cycles, also referred to as notch root plasticity. This plasticity will improve the fatigue response of the material, meaning the material will fail at $D > 1$ as calculated by Miner's rule. If the spectrum were reversed, meaning smaller amplitude load cycles are applied first and large amplitude load cycles are applied after that, Miner's rule would be correct since this plasticity is not present during the small amplitude load cycles. Figure 2.17 shows the error that Miner's rule makes when applied to different load spectra. It is clear that when a small amplitude load is preceded by a large amplitude load, the material will fail later than expected due to notch root plasticity. When the spectrum is reversed, the material fails sooner than expected. When the specimen is notched, these differences can become very large. This shows how important it is to critically analyse the load spectrum to which Miner's rule is applied before drawing conclusions on the fatigue life of the material [31].
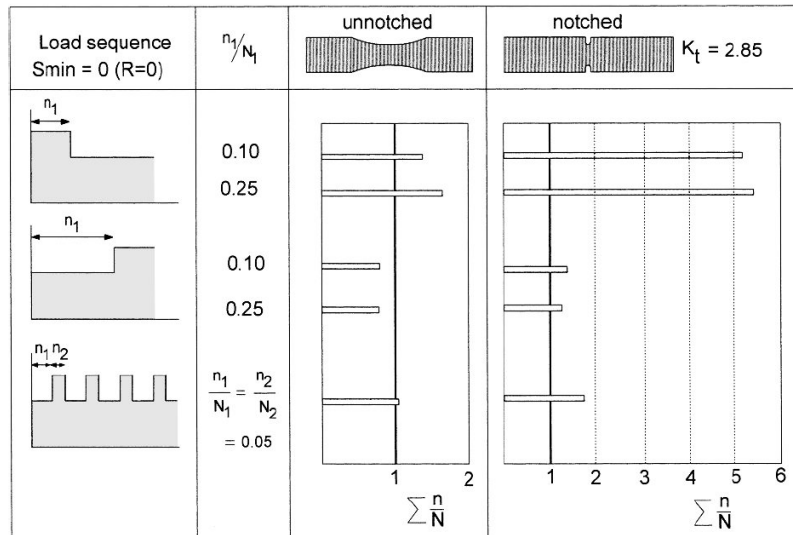
Figure 2.17: Error of Miner's rule for different load spectra [31]

2.5.2. S-N curve

A commonly used tool in fatigue analysis is the S-N curve. These curves are generated through specimen testing. During these tests, a constant amplitude load cycle is applied to the specimen and the number of cycles until failure is recorded. It takes a lot of specimen to be tested at a large number of different amplitude load cycles to generate a reliable S-N curve. For metals, the database is quite extensive. Composite specimen have not been as thoroughly tested as metals although relatively large databases such as the DOE/MSU database exist. Additionally, composite materials have more design parameters than metals like fibre content, fibre orientation, layer thickness and type of resin used. This makes it more difficult to provide S-N curves as a change in one of these parameters can change the fatigue life of the material. An example of a composite S-N curve is shown in figure 2.18 while an example of a metal S-N curve can be seen in figure 2.19, both of these curves have a log-log scale. Note that steel has a fatigue limit so the stress amplitude will never drop completely to zero. The fatigue limit is the stress amplitude below which no fatigue failure will occur. Equation 2.20 gives the S-N curve in the form of an equation. Here, σ is the stress amplitude, N is the number of cycles until failure and $-\frac{1}{b}$ represents the slope of the curve [30].

$$\sigma = CN^{-\frac{1}{b}} \tag{2.20}$$
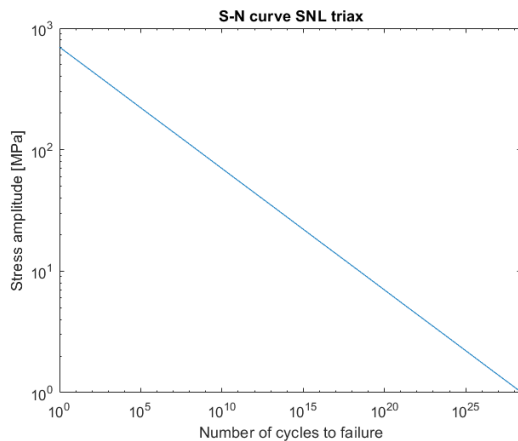
Figure 2.18: S-N curve of the composite blade material
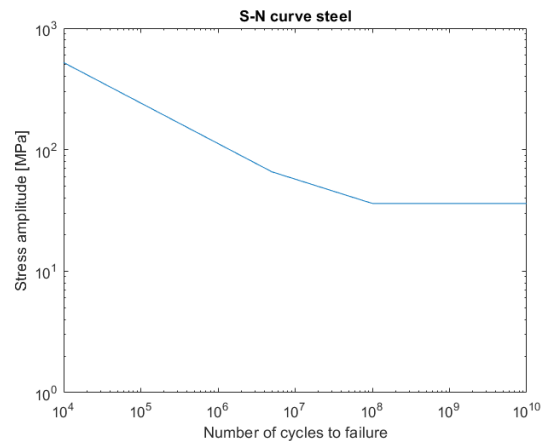
Figure 2.19: S-N curve of the tower material

2.5.3. Goodman diagram

A more accurate tool for fatigue assessment and mostly used in design projects is the Goodman diagram. An example of a typical Goodman diagram is shown in figure 2.20. The vertical axis plots the ratio of stress amplitude to ultimate stress, while the horizontal axis contains the effect of mean stress. Constant life arcs are shown in the figure to easily analyse the effect of parameter changes on fatigue life. Constant R ratio lines are plotted as well, where $R = \frac{\sigma_{min}}{\sigma_{max}}$, meaning the minimum stress to maximum stress ratio. In fully reverse bending, $R = -1$ and the mean stress is zero. It can be seen in the figure that the effect of mean stress can have a significant impact on the fatigue life. This is why a Goodman diagram is more accurate than an S-N curve. But in order to obtain such a diagram, a considerate amount of specimen testing is needed. The reason for this is that a Goodman diagram is essentially a graphical representation of a family of S-N curves for different mean stresses. The Goodman fit is given by equation 2.21. Here, σ_a represents the alternating stress, σ_m is the mean stress, σ_e is the equivalent zero-mean alternating stress and σ_{ult} is the ultimate stress which can be replaced by the yield stress depending on the nature and goals of the analysis. The constant c is usually taken to be equal to 1, but can be changed depending on the fit [30].

$$\sigma_{\mathrm{a}} = \sigma_{\mathrm{e}} \left[1 - \frac{\sigma_{\mathrm{m}}}{\sigma_{\mathrm{ult}}} \right]^{\mathrm{c}} \qquad (2.21)$$
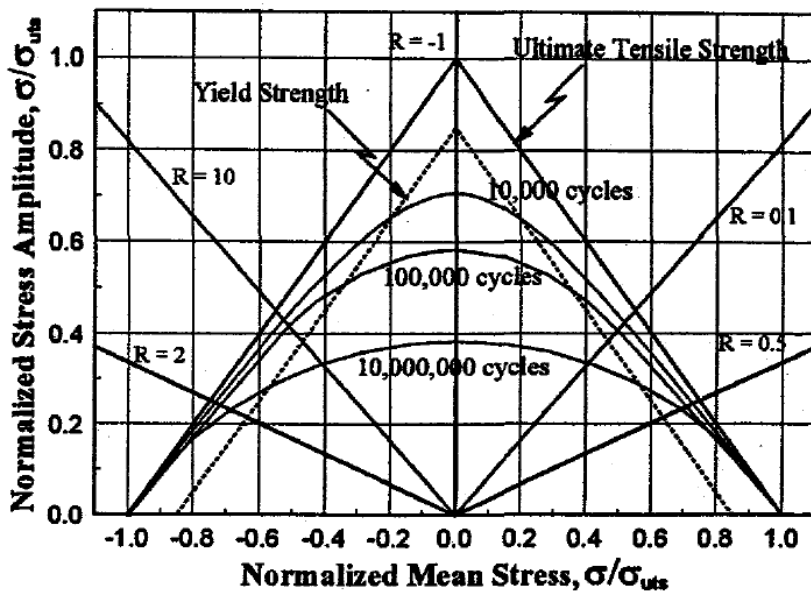
Figure 2.20: Example of a Goodman diagram [30]

2.5.4. IEC standards

Table 2.3 shows the basic parameters for each IEC wind turbine class. There are nine classes, where each class consists of a number between I-III corresponding to the wind speed at hub height, and a letter from A-C corresponding to the turbulence intensity at a wind speed of $15 \frac{m}{s}$. The parameter U_{ref} is the reference wind speed equal to $U_{ref} = 5\bar{U}$, where $\bar{U}$ is the average 10-minute wind speed at hub height [32].

Table 2.3: IEC wind turbine class basic parameters

Wind turbine class		I	II	III
U_{ref}	(m/s)	50	42,5	37,5
A	I_{ref} (−)	0.16		
B	I_{ref} (−)	0.14		
C	I_{ref} (−)	0.12		

For fatigue calculations, the most important model to consider is the Normal Turbulence Model (NTM). For this model, equation 2.22 gives the standard deviation of the wind speed, corresponding to the 90% quantile for the given wind speed at hub height. The turbulence intensity is then given by $TI = \frac{\sigma_U}{U_R}$. Values of I_{ref} are provided in table 2.3. Figure 2.21 shows the turbulence intensity vs wind speed at hub height for the different IEC classes [32].

$$\sigma_U = I_{\text{ref}} (0,75 U_R + const); \quad const = 5,6 \, \text{m/s} \tag{2.22}$$
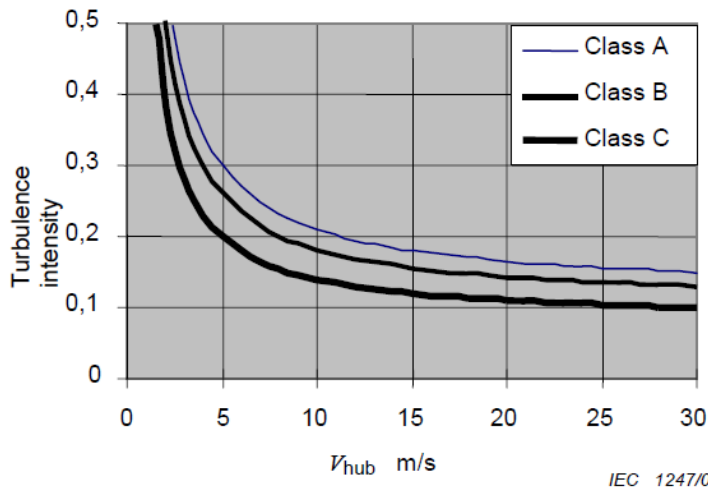
Figure 2.21: Turbulence intensity vs wind speed for IEC classes [32]

For fatigue calculations, several load cases have to be assessed. These load cases include a NTM analysis in power production with and without the occurrence of a fault, a NWP during start and normal shut down and a NTM for parked conditions. The NWP is the Normal Wind Profile model and uses the power law approximation to approximate the average wind speed where the exponent is assumed to be $\alpha = 0.2$.

According to IEC standards, two partial safety factors have to be applied to fatigue calculations. The first partial safety factor relates to the accuracy of the S-N curve data of fibre composites. A safety factor of 1.2 is applied to account for uncertainties in this area. The second safety factor is about the consequence of failure. For class 2 components like wind turbine blades, this safety factor is 1.15 [32].

2.6. FAST

FAST (Fatigue, Aerodynamics, Structures and Turbulence) is a model developed by NREL. It is an engineering tool that can simulate a horizontal axis wind turbine with either two or three blades [33]. Figure 2.22 gives an overview of all of the solvers that are coupled to the FAST driver. Note that this discussion relates to version 8 of FAST, this is the last version of the software before its transition to OpenFAST. All of these coupled solvers allow for an extensive wind turbine simulation. The interactions between different modules of the tool is shown in figure 2.23. External conditions are specified using InflowWind. These conditions are then fed into the aerodynamic solver AeroDyn. The aerodynamic solver interacts with the structural solver ElastoDyn in order to iterate structural and aerodynamic solutions. The structural solver requires input from and interaction with ServoDyn, which is responsible for the wind turbine control specifications and the drive train dynamics. These results can then be expanded to the foundation of the wind turbine using SubDyn, which performs calculations on either the part of the tower that is below the water or the floating structure. For this, SubDyn requires inputs from and interaction with both the structural solver for the tower and the external conditions solver for waves and currents which is called HydroDyn. Using all of these interactions and assuming all inputs are properly specified, a wind turbine can be simulated [34].

This means that the software takes as input the external conditions and the specifications of a turbine. Turbine specifications include control strategy, power curve, blade and tower dimensions, generator spec-

ifications etc. Simulations can then be performed for fatigue, extreme loading and energy yield to generate the desired results.
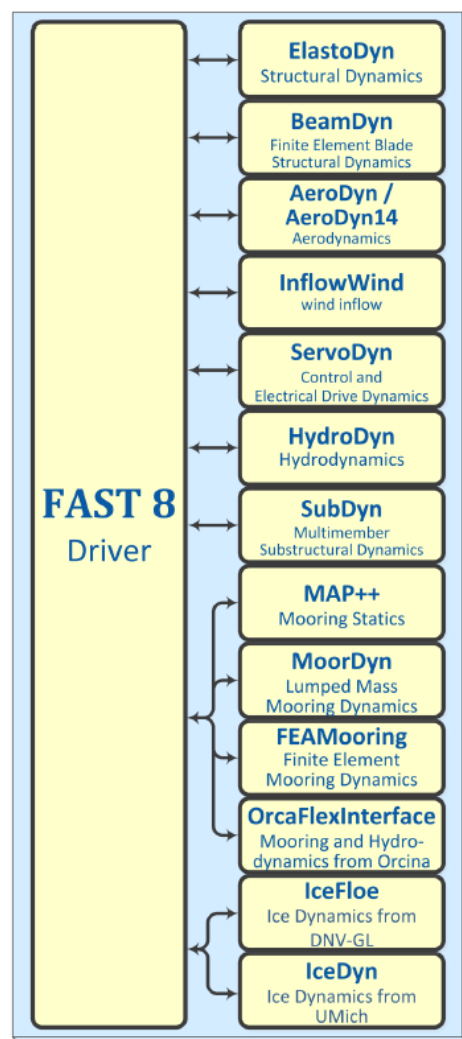
Figure 2.22: Overview of the structure of FAST [34]
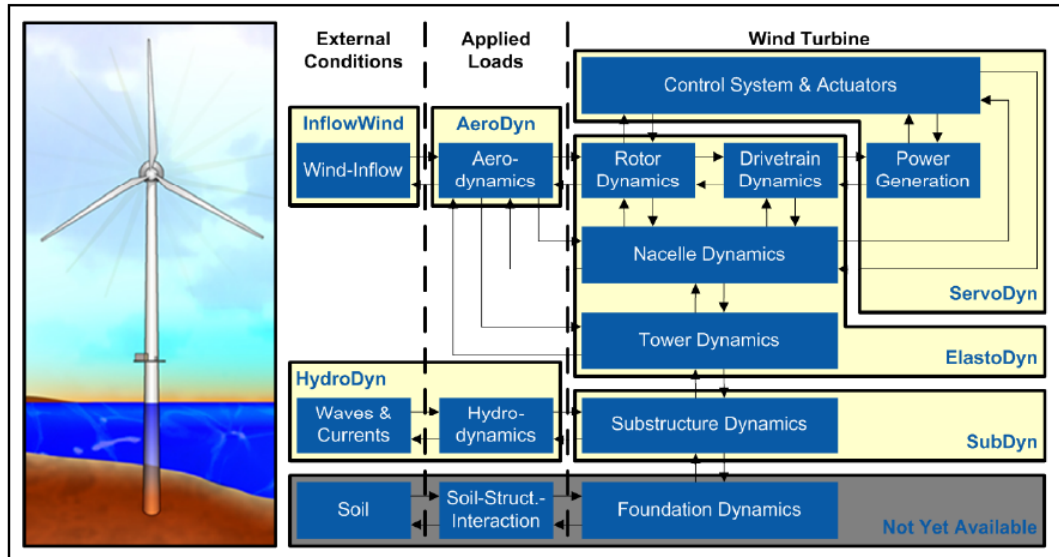
Figure 2.23: FAST module interactions for fixed-bottom systems [34]

<div style="text-align: right; font-size: 3em;">

3

</div>

Description of the dataset

In this chapter, a brief description of the dataset will be provided. This data will be analysed in the following chapters of the report. Section 3.1 will describe the DOWA dataset while section 3.2 will discuss the site measurement data that will be used for the validation procedure.

3.1. DOWA

The DOWA simulation outputs are stored in the KNMI data platform [1] and can be downloaded from the data catalogue directly or through a script. The data is stored in NetCDF format and can be opened using MATLAB. Data is stored both in the form of daily 3D files and in 10 year time series. In the daily 3D files, the data of all grid points for one day can be downloaded as a single file, the temporal resolution is one hour. In the 10-year time series, the same data can be downloaded but organised per grid point. This means that every file contains the full 10-year time series of a single grid point. Both types of formats contain exactly the same data, but depending on how the data is used, a different format could be more convenient. For the purpose of this research, the 10-year time series files seem to be the most convenient. In order to download all files in this dataset, example scripts in Python for bulk dataset downloads are provided on the KNMI data platform under the 'developer portal' tab.

There are $217x234$ grid points in the DOWA, meaning the 10-year time series dataset contains 50.778 files with a size of $53MB$ each. This is around 2.6 terrabytes of data. Note that this is the temporary space needed to store the files. The relevant parameters are humidity, pressure, temperature, wind speed and wind direction. When these five parameters are extracted in MATLAB and converted into .mat files, the size of the data is reduced to $1.13TB$.

Upon opening the netCDF file containing the full time series of a single grid point, some things can already be noted. First of all the general attributes are listed in the description. It states the version of HARMONIE that is used to generate this data, which is harmonie-40h1.2.tg2. ERA5 is the driving model and the creation date of this dataset is September 11, 2018. Secondly, the dimensions of the variables are stated. For this format, the x and y dimensions are both 1 as it contains data for a single grid point only. The height dimension is 17, which is the number of heights for which data is available. These heights are 10, 20, 40, 60, 80, 100, 120, 140, 150, 160, 180, 200, 220, 250, 300, 500 and 600m. There is also a time vector which contains 87673 values. This corresponds to the amount of hours in the period starting on 01/01/2008 at 00:00h with as final value 01/01/2018 at 00:00h. There were 3 leap years during this period, meaning the amount of hours is as calculated in equation 3.1.

$$(7 \cdot 365 + 3 \cdot 366) \cdot 24 + 1 = 87673 \tag{3.1}$$

Finally, the variables in the file are of importance. The first variable to be verified is the time variable. As

---

[1] https://dataplatform.knmi.nl/catalog/index.html

calculated above, it contains 87673 values with as unit the amount of days since the start of the dataset. The x and y variables contain just 1 value each with the projected x and y coordinate, respectively. The units of these variables are metres. The next variables are 'lon' and 'lat', these are the longitude and latitude in degrees east and degrees north, respectively. These variables also contain just one value each. The next variable of interest is the height. As mentioned earlier, it contains 17 values expressed in a number of metres above mean sea level. The variables 'wdir' and 'wspeed' are also part of the dataset, representing wind direction and wind speed, respectively. They each have dimensions of 1x1x17x87673, meaning there is a value for every height for every hour. Wind direction is expressed in degrees and the unit of wind speed is $\frac{m}{s}$. There are three more variables to be discussed: 'ta', 'p' and 'hur'. They have the same dimensions as wind speed and wind direction and represent the air temperature, pressure and relative humidity, respectively. Keep in mind that these last three variables have not been validated yet.

In addition to the data described above, the DOWA also provides data for three offshore wind farm locations. The same parameters are included as for the full domain with as extra parameter the standard deviation of the wind speed. Furthermore, the values provided for the wind farm locations have a 10-minute temporal resolution instead of the one hour resolution in the rest of the domain. The data for the wind farm locations is provided both for the presence of the wind farm and for free-stream conditions. The Borssele wind farm contains data for the years 2015, 2016 and 2017, the Hollandse Kust Noord wind farm location contains data for the years 2009, 2010 and 2017 and Hollandse Kust Zuid contains data for the years 2016, 2017 and 2018, where the year 2018 only has data up to and including July 30. Some days are missing in the datasets, which is extensively described in the report describing and validating the GRASP model used to perform the LES at these locations [35].

3.2. Measurements

On the Wind @ Sea website [2] by TNO, data can be requested for the following meteorological stations:

- Lichteiland Goeree (LEG)
- Europlatform (EPL)
- K13A
- Meteomast IJmuiden (MMIJ)
- Offshore wind park Egmond aan Zee (OWEZ)
- Borssele wind farm zone (also in DOWA)
- Hollandse Kust Zuid (HKZ, also in DOWA)

The locations and types of these measurement stations are visualised in figure 3.1.

---

[2]https://www.windopzee.net/

Figure 3.1: Measurement locations [36]

The first measurement location to be analysed is the Borssele wind farm zone. Measurements have been performed for this zone in two different locations. The first location is 'lot 1' with coordinates $51°42.41388'N$,$3°2.07708'E$ and the second location is 'lot 2' with coordinates $51°38.778'N$,$2°57.0846'E$ [37] [38]. For lot 1, the location with the longest period of available data, monthly data is publicly available for the period of 11 June 2015 until 18 July 2016. In this period, there is no data for: 15 September 2015 - 11 November 2015 and 15 December 2015 - 11 February 2016. This means that some data is missing, which has to be taken into account when analysing the data because some seasonal fluctuations may not be captured. Note that for lot 1, measurements were performed up to and including February 2017, but this data is not publicly available.

Measurements are performed using the Seawatch Wind LiDAR buoy, equipped with a variety of instruments to measure wind and wave parameters. The parameters that are of interest for this project are wind speed, wind direction, air pressure, humidity and temperature. Wind speed and direction are measured with a LiDAR for the following heights: $30m$, $40m$, $60m$, $80m$, $100m$, $120m$, $140m$, $160m$, $180m$ and $200m$ with a sampling interval of approximately $17.4s$. Air pressure, humidity and temperature are only measured at the location of the buoy. This means it will be impossible to perform calculations regarding Obukhov length and temperature profile for stability estimations.

The measurements at the HKZ wind farm zone are obtained using two buoys located approximately $2km$ away from each other. The choice of buoy measurements to be used for the DOWA validation is therefore irrelevant of location since the DOWA spatial resolution is $2.5km$ by $2.5km$. The buoys and corresponding measurement parameters and heights are identical to the buoy deployed at the Borssele wind farm. Measurements are publicly available for the period of June 2016 up to and including May 2017. There are no missing months in this dataset, but some availability issues were encountered that need to be filtered out before starting the calculations [39].

The Meteomast IJmuiden (MMIJ) will be used for stability validation because its output contains pressure, humidity and temperature data at heights of $27m$ and $90m$. Additionally, the output data contains wind speed and wind direction at heights of $27m$, $58m$ and $90m$ with a temporal resolution of $0.25s$. Data is available through the Wind @ Sea website for the full year of 2015.

4
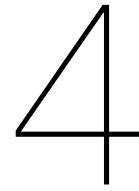
Method

Based on the theory discussed in chapter 2 and the dataset presented in chapter 3, some methods can be described to perform the required analyses in order to meet the project goals. The methods to estimate the parameters relevant for atmospheric stability classification can be found in section 4.1. The energy yield and fatigue calculation methods will then be discussed in section 4.2 and section 4.3, respectively.

4.1. Atmospheric stability

Atmospheric stability can be quantified and classified using different parameters, this was already described in section 2.2. The method to calculate most of these parameters based on the available data will be described in this section. The method used to find low level jets and estimate the wind shear exponent, Obukhov length and temperature profile are described in subsection 4.1.1, subsection 4.1.2, subsection 4.1.3 and subsection 4.1.4, respectively. The turbulence intensity will then be discussed in subsection 4.1.5.

4.1.1. Low level jets

To find low level jets, some conditions have to be fulfilled depending on the purpose of the study. The input for the procedure are the wind speed values of the DOWA for all heights except $10, 500$ and $600m$ as these are not relevant for the purpose of this research. If the low level jet would be above $300m$, the wind turbines under consideration in this report would simply see a logarithmic wind profile. It was decided to discard the height of $10m$ due to concerns about the accuracy of the data as was already established by the DOWA validation report[11], while starting the analysis at a height of $20m$ is still considered sufficient as this is below the rotor swept area of both reference turbines. The procedure to find instances containing a low level jet is as follows:

1. Find each instant with a maximum wind speed that occurs below $300m$

2. For each of these instances, find the absolute and relative difference between this maximum wind speed and the minimum wind below and above the height of the maximum wind speed

3. If the absolute difference is larger than $0.5\frac{m}{s}$ and the relative difference is larger than 5%, the instant is marked as a LLJ event. Note that these differences must apply both below and above the height of the maximum wind speed as indicated in figure 4.1

Note that in literature, usually a threshold of $2\frac{m}{s}$ is chosen[40]. The threshold values chosen here for the absolute and relative difference are based on an iterative approach using visual inspection of the vertical wind profile. This means that during the atmospheric stability analysis, it was found that a significant

number of wind speed profiles that were not marked as a LLJ was discarded due to the fact that they did not follow the power law profile. Upon visual inspection, it was seen that most of these discarded profiles resemble a low level jet, meaning the criteria for LLJ identification had to be iterated. An example of such a discarded shear exponent wind speed profile that should have been identified as a low level jet is shown in figure A.3 in appendix A.
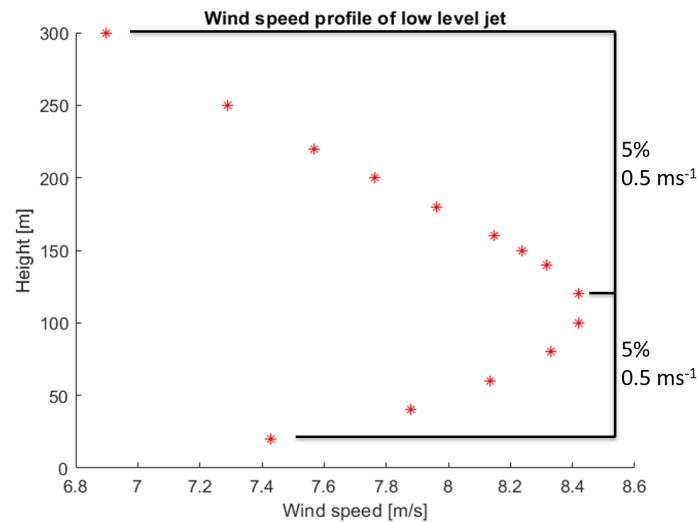
Figure 4.1: Low level jet identification criteria. Absolute and relative difference have to be larger than $0.5\frac{m}{s}$ and 5%, respectively. This applies both above and below the maximum wind speed height.

4.1.2. Wind shear exponent

The wind shear exponent is calculated using a power law fit. The only input it needs is the wind speed at two heights. The wind shear exponent is obtained using equation 2.4. Two wind shear exponents are calculated for each hour of simulation data, where each exponent is tuned to one of the reference turbines. Both shear exponents are calculated with the height of $20m$ as lowest value. The second height is chosen to be $100m$ for the first reference turbine and $150m$ for the second. This gives two power law fits for the same vertical wind profile.

The next thing to do is divide the wind shear exponents into stability classes according to figure 2.13. A problem with this approach is that it includes the instances where the vertical wind profile does not follow the power law due to for example low level jets, which is why the low level jets found previously are removed from the data. The power law is plotted according to equation 2.3, where z_R is chosen to be $150m$ for the 15MW turbine and $100m$ for the 5MW turbine. This data is then plotted and compared to the DOWA simulation data. For each wind turbine, the relevant heights, meaning the heights in the rotor swept area, are used to calculate the error of the power law fit compared to the DOWA data. The absolute value of this error is used to calculate the error of the power law fit, expressed in percentages relative to the wind speed at height z_R, where the error is 0. This is why z_R was chosen around hub height. If the average of the absolute value of the relative error exceeds 5%, the fit is marked as invalid. Note that due to the usage of the absolute value, the error of 5% is an overestimation in all cases. This is because in most cases, the error below z_R is opposite in sign to the error above z_R, meaning the errors at least partially cancel each other out with respect to energy yield.

This leaves a list of hours at which the vertical wind profile does not follow the power law, while these hours were not identified as a low level jet. These are also taken out of the stability classes to get a more accurate representation of the stability.

Additionally, a stability histogram will be computed for four offshore locations visualising the occurrence of a certain stability class for each wind speed. These locations are the three offshore wind farm locations available in the DOWA and the MMIJ met mast.

4.1.3. Obukhov length

The Obukhov length is estimated using the gradient Richardson number as explained in subsection 2.2.2. Where the wind shear exponent only needs wind speed as input, the Richardson number estimation requires both virtual potential temperature and wind speed. The virtual potential temperature is calculated using temperature, pressure and humidity as shown in equation 2.12. The mixing ratio in this equation is the product of the saturation mixing ratio and the relative humidity. The saturation mixing ratio is a function of temperature that can be looked up in literature while the relative humidity is a direct output of the DOWA. The purpose of virtual potential temperature is to correct the temperature for pressure and humidity variations.

This virtual potential temperature can be used together with the wind speed to calculate the gradient Richardson number given by equation 2.9. Like for the wind shear exponent, two Richardson numbers are calculated, each corresponding to a reference turbine. The heights are chosen based on the validity height of the Richardson number. The Richardson number is valid for height $z' = \frac{z_1 - z_2}{ln(\frac{z_1}{z_2})}$ [25]. For the 5MW reference turbine, the chosen heights are 60 and $140m$, while for the 15MW turbine they are 100 and $220m$. The heights at which the Richardson numbers are valid are then 94 and $152m$, respectively. It is assumed the Richardson numbers are valid at the hub heights of 90 and $150m$.

Based on the Richardson number, the Obukhov length is calculated following equation 2.13. Based on the value of L, each vertical wind profile is assigned to a stability class based on figure 2.14. An additional analysis is performed to obtain the stability histogram for the four offshore locations previously described in the shear exponent method.

4.1.4. Temperature profile

Determining stability through the temperature profile requires temperature data for different heights. All available DOWA heights are used in this approach except 10, 500 and $600m$, leaving 14 heights to be analysed. The input for this calculation is the potential temperature, which is calculated using the same method as in subsection 4.1.3. The first step is to calculate the temperature difference between two subsequent heights. This gives 13 values for each temperature profile. The height difference between two subsequent heights is not constant, this is why the temperature difference between two heights is normalised with the height difference giving a temperature difference per meter.

If the temperature difference is larger than $0\frac{K}{m}$, a score of 1 is assigned. If the temperature difference is lower than $0\frac{K}{m}$, a score of -1 is assigned. In case the temperature difference is equal to $0\frac{K}{m}$, a score of 0 is assigned.

The stability based on temperature profile is assessed separately for both reference turbines. This means that only the values corresponding to heights within the rotor swept area are used. For the 5MW rotor, this leaves 6 temperature difference values per hourly temperature profile while for the 15MW rotor, 11 values are left. A temperature profile for the 5MW reference turbine is considered stable when the sum of the 6 scores is at least 2, while for the 15MW turbine the sum of 11 scores should be at least 5. This means that at most 2 out of 6 values show a negative temperature difference for the $5MW$ turbine and at most 3 out of 11 values show a negative temperature difference for the $15MW$ turbine. The temperature profile is unstable when the sum of the scores is no larger than -2 and -5 for the $5MW$ and $15MW$ wind turbines, respectively. A temperature profile is classified as neutral in all other cases, meaning no values are discarded in the temperature profile stability analysis.

4.1.5. Turbulence intensity

The turbulence intensity is calculated using equation 2.14. Unfortunately, this requires as input the standard deviation of the wind speed which is only available for locations around three offshore wind farms. Two locations around the Borssele wind farm, two locations around the Hollandse Kust Zuid wind farm and three locations around the Hollandse Kust Noord wind farm. The turbulence intensity can be calculated for each 10-minute interval. The results of these seven locations are analysed in order to see the variability of turbulence intensity between two wind farms and within a wind farm. Note that the DOWA provides data

both for free stream conditions and for operating wind farm conditions. The calculations described above use the free stream data as input because the results are intended to be extrapolated to areas where no wind farm is present.

The turbulence intensity of these wind farm locations is analysed per wind speed. To do this, the 10-minute wind speed mean and standard deviation of the three wind farms are used. The turbulence intensity for each 10-minute interval is calculated and sorted per wind speed interval. Then, the average turbulence intensity for a certain wind farm at a certain wind speed is calculated as well the standard deviation. This allows for a comparison of turbulence intensity versus wind speed of three wind farm locations while the standard deviation gives an estimate of the accuracy of these turbulence intensity values.

4.2. Energy yield

The method used to calculate the annual energy yield of a wind turbine is shown in the form of a flowchart in figure 4.2. The general idea of this flowchart will be described first, while a more detailed description of the individual components will follow below the figure. First, the wind speeds are corrected for a deviation from the standard atmospheric density of $1.225\frac{kg}{m^3}$. This process takes as inputs the wind speed, pressure and temperature. The output of the density correction is U_{norm}. These wind speeds then have to be corrected for wind shear. The output of the shear correction is the rotor equivalent wind speed U_{eq}. This wind speed is then corrected for turbulence intensity. The output of the TI correction is U_{corr}. These wind speeds are then used to fit a Weibull curve. In order to do this, the wind direction is also required as input. The output of this process is the Weibull curve, which is used in combination with the power curve to calculate the power output of the wind turbine for every time interval. This power output can then be used to calculate the annual energy yield.
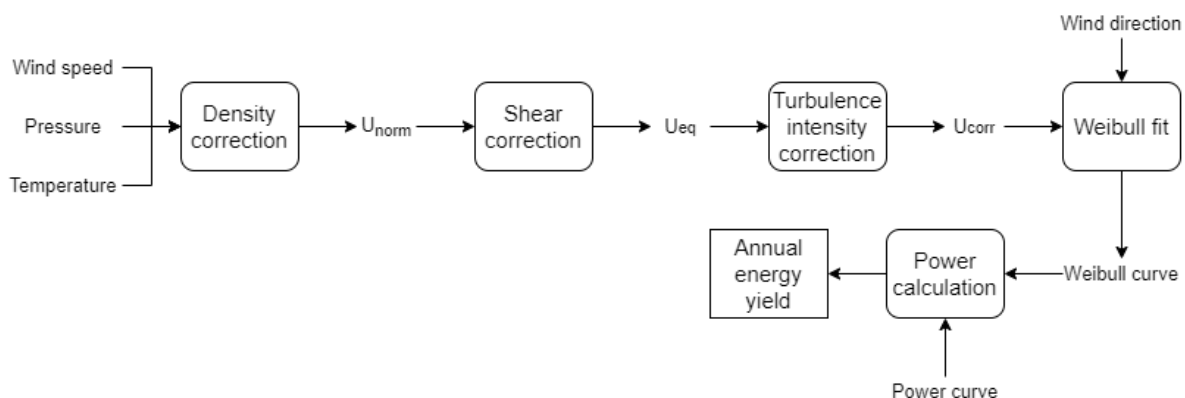
Figure 4.2: Method used to calculate the annual energy yield of a wind turbine

In subsection 4.2.1, the density correction will be discussed in more detail. The section will continue with a description of the shear and turbulence intensity corrections in subsection 4.2.2 and subsection 4.2.3, respectively. The Weibull fit will be discussed in subsection 4.2.4 and the section will conclude with the energy yield calculation in subsection 4.2.5.

4.2.1. Density correction

The air density correction is applied according to equation 2.15, where U is the wind speed taken from the DOWA output, $\rho_0 = 1.225\frac{kg}{m^3}$ and ρ is calculated according to the ideal gas law given by equation 4.1. Here, p is the air pressure, T is the temperature in Kelvin and $R_d = 287.058\frac{J}{kgK}$ is the specific gas constant of dry air. Note that in reality and especially for the offshore locations in the DOWA, the air is not dry. But even for a very high relative humidity, the assumption of using dry air does not influence the results to a large extent [1].

---

[1] When considering an extreme case of e.g. a temperature of $30°C$, the air can hold up to 4% water vapor. Assuming the air is fully saturated, the specific gas constant becomes $R = 0.96 \cdot R_d + 0.04 \cdot R_v = 0.96 \cdot 287 + 0.04 \cdot 461 = 294\frac{J}{kgK}$. This will change the

$$\rho = \frac{p}{R_d T} \tag{4.1}$$

4.2.2. Shear correction

Correcting the wind speed for wind shear is important, especially for offshore locations since significant wind shear due to stability effects can occur. Problems in the estimation of stability have already been described in section 4.1. This is why it is chosen to use rotor equivalent wind speed as a measure for wind shear for the energy yield calculations. This is a convenient method due to the data being available at a relatively large number of heights. Figure 4.3 shows the sections used to calculate the rotor equivalent wind speed of the NREL 5MW rotor. These sections correspond to data at heights of 40, 60, 80, 100, 120, and $140\,m$. The sections for the IEA 15MW rotor are shown in figure 4.4. These correspond to data at heights of $40, 60, 80, 100, 120, 140, 150, 160, 180, 200, 220$ and $250\,m$. Note that not all of these heights correspond to the middle of a section, but it is assumed that the wind speed for a height in a section corresponds to the wind speed for the entire section. The rotor equivalent wind speed is then calculated according to equation 2.18.
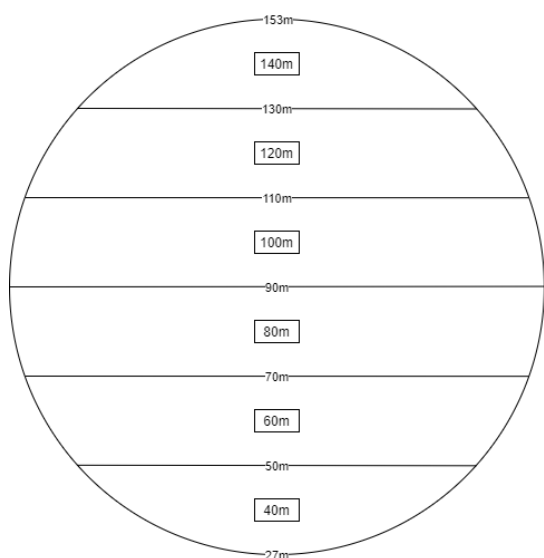

Figure 4.3:
NREL 5MW rotor sections used to calculate U_{eq}
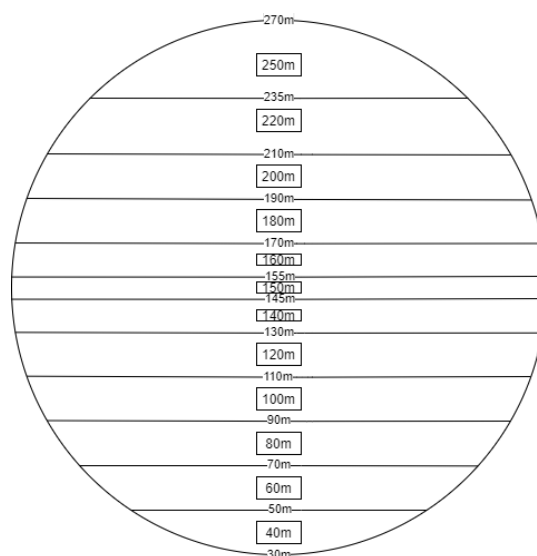
Figure 4.4: IEA 15MW rotor sections used to calculate U_{eq}

4.2.3. Turbulence intensity correction

The next wind speed correction to consider is the turbulence intensity correction. The turbulence intensity is calculated using equation 2.14. This means that both wind speed mean and standard deviation values have to be available. This is only the case in the DOWA for the area around three offshore wind farms. It was found that the turbulence intensities for the three wind farm locations are very similar. It is then assumed that this turbulence intensity applies to all locations in the simulated domain, meaning all locations have the same turbulence intensity corresponding to the value found at the wind farm locations.

4.2.4. Weibull fit

With the wind speed now corrected for density, wind shear and turbulence intensity, the next step is to fit a Weibull curve. This is done according to the European wind atlas model. The European wind atlas model focuses its Weibull fit on the most important aspects of wind energy. In order to do this, there are two requirements to fulfill.

1. The total wind energy of the fitted Weibull distribution should be equal to the total wind energy in the

density of air by 2.4%. Note again that this is an extreme case and in reality, the differences will be much smaller.

data

2. The average wind speed should be calculated from the data. The amount of wind speed occurrences above this average wind speed should be equal for the Weibull fit and the data.

The available wind power density is proportional to the cube of the wind speed (third moment) given by equation 4.2, the mean wind speed (first moment) is calculated using equation 4.3 [41]. The second condition states that the amount of wind speed occurrences below the average wind speed of the data, $F_{\bar{U}}$, should be equal to the frequency of occurrence of the cumulative Weibull distribution for that same average value, this is stated in equation 4.4. In this equation, the scale parameter a can be substituted using equation 4.2, which gives equation 4.5. This equation only has one unknown, the shape parameter k, which can be solved by finding the roots of the equation. The scale parameter a can then be determined using the first condition and equation 4.2, where the sum of the power densities of the Weibull distribution should be equal to the sum of the power densities of the data. Again, there is only 1 unknown which can be solved by a simple root-finding algorithm. Note that in the code, some safety should be built in to ensure that the code does not output non-numerical Weibull parameters due to an invalid initial guess in the root-finding algorithm. This procedure is applied for every wind speed sector, which is why wind direction is needed as an input. The wind speeds are divided into twelve sectors before the Weibull fit is performed. This means that each sector will have a different Weibull curve.

$$\langle u^3 \rangle = a^3 \Gamma\left(1 + \frac{3}{k}\right) \tag{4.2}$$

$$\bar{U} = \langle u \rangle = a \Gamma\left(1 + \frac{1}{k}\right) \tag{4.3}$$

$$0 = F_{\bar{U}} + \exp\left[-\left(\frac{\langle u \rangle}{a}\right)^k\right] - 1 \tag{4.4}$$

$$0 = F_{\bar{U}} + \exp\left[-\left(\frac{\langle u \rangle}{\left(\frac{\langle u^3 \rangle}{\Gamma(1+3/k)}\right)^{1/3}}\right)^k\right] - 1 \tag{4.5}$$

4.2.5. Energy yield calculation

Once the Weibull curve for each sector is known, it can be combined with the power curve in order to calculate the power output and annual energy yield. The energy yield for a sector is calculated using equation 4.6. The total energy yield is then simply the sum of the energy yields of each sector. In the equation, T is the number of hours, U_{ci} is the cut-in wind speed, U_{co} is the cut-out wind speed, P(U) is the power curve and f(U) is the Weibull curve.

$$E(sector) = T \int_{U_{ci}}^{U_{co}} P(U) \cdot f(U) dU \tag{4.6}$$

4.3. Fatigue

The method used to calculate the lifetime fatigue damage of a wind turbine is visualised in figure 4.5. First, simulations are run in FAST, where bending moments at the blade root and tower base are calculated. These moments are then converted into stresses in order to apply rainflow counting to obtain a stress histogram. This histogram can be used to determine the hourly damage fraction which in turn is used to calculate the total fatigue damage. A more detailed explanation of the method will be provided below the figure.
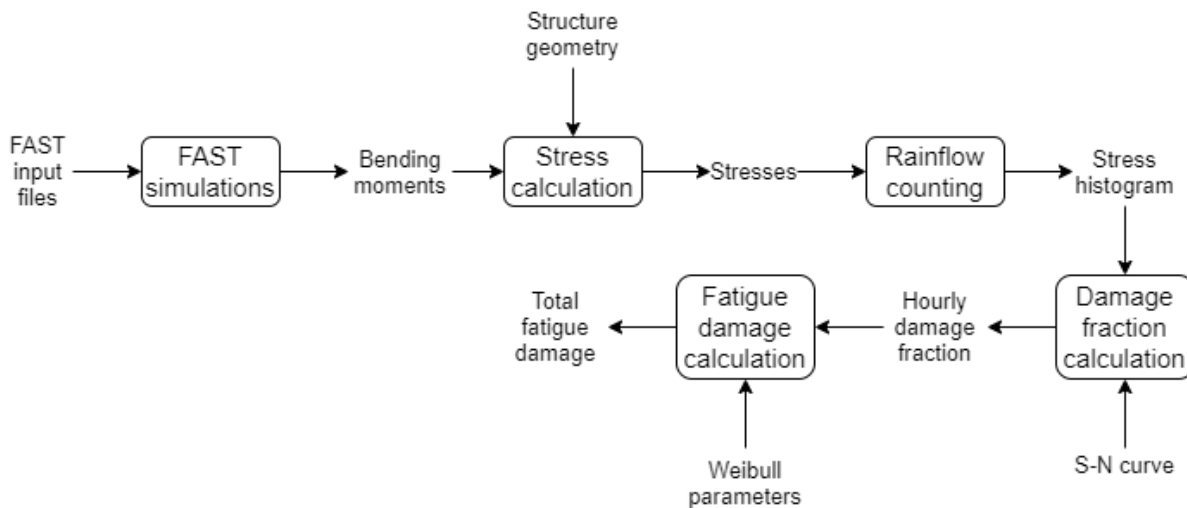
Figure 4.5: Method used to calculate the lifetime fatigue damage of a wind turbine

A detailed description of the FAST simulations is provided in subsection 4.3.1 while the stress calculation method is given in subsection 4.3.2. Subsection 4.3.3 and subsection 4.3.4 will discuss the rainflow counting algorithms and damage fraction calculation, respectively. Finally, the fatigue damage calculation method will be given in subsection 4.3.5.

4.3.1. FAST simulations

As shown in figure 4.5, FAST is used to perform the wind turbine simulations. FAST can be used by either running the raw code, or by creating a simulink interface in MATLAB since the software can be called through an S-function block. Such a simulink model has already been created for version 8 of the FAST software by the TU Delft Data-Driven Control department. This simulink integration, that comes with a MATLAB GUI, is open-source and available through their GitHub repository [2]. FASTTool [3] comes with a ready to use input file for the NREL $5MW$ reference turbine, but the input file for the $15MW$ reference turbine does not exist. This means that for this turbine, an input file still has to be written. All data needed for this can be found in the files of the IEAWindTask37 Github repository [4]. This repository contains files for this reference turbine, written for OpenFast.

Simulations are performed for both the $5MW$ and $15MW$ reference turbine. Simulations are run using the Normal Turbulence Model (NTM) during power production mode. The NTM model takes as input the wind speed and IEC class. IEC class 1C is chosen for the $5MW$ turbine as a comparison value. The turbulence classes as specified by IEC standards were found to be inadequate, since an analysis of three wind farm locations showed turbulence intensities far below the IEC values. In order to account for this, it is possible to manually input a turbulence intensity value in the TurbSim module of FAST rather than choosing an IEC class [42]. For this reason, turbulence classes D and E were manually added in the FAST code, corresponding to turbulence intensity levels at a hub height of $150m$ and $90m$, respectively. A turbulence intensity analysis was performed using the DOWA 10-minute data of three offshore wind farms. It was found that the turbulence intensity at a wind speed of $15\frac{m}{s}$ corresponds to around 6% for the $5MW$ reference turbine hub height and around 5% for the $15MW$ reference turbine.

It is important to note here that the TurbSim module in FAST uses the power law exponent approximation to estimate the shear over the rotor disk. This means stability effects are not included in the simulation results. An additional simplification that was introduced during the simulations was the skewed-wake parameter in the AeroDyn module. This parameter affects the skewed-wake correction model used. During the simulations for the $15MW$ turbine, an error occurred due to a calculated Mach number over the airfoil being larger than 1. This is a bug in the AeroDyn code itself which is no longer present in the most recent

---

[2] https://github.com/TUDelft-DataDrivenControl/FASTTool
[3] FASTTool was developed for and used in the TU Delft course 'AE4W09: Wind Turbine Design'
[4] https://github.com/IEAWindTask37/IEA-15-240-RWT

version of the software. The FASTTool simulink interface however still uses an older version of the module, requiring the skewed-wake correction model to be switched to 'uncoupled' in order to avoid the error. For the $5MW$ wind turbine simulations, the error did not occur and the Pitt-Peters correction model can be used. The effects that this simplification has on the output are difficult to estimate, but the fact that it is present should be kept in mind when analysing the results.

The FAST simulation is performed only for the wind speeds during power production. Due to FAST limitations, the cut-in wind speed of $3\frac{m}{s}$ is not simulated. This means that results are obtained for wind speeds of $4-25\frac{m}{s}$ with a $1\frac{m}{s}$ interval.

Each simulation is run for 660 seconds, where the first 60 seconds are discarded to eliminate any initialisation error leaving 10 minutes of data. For each condition, the simulation is run for six different seeds to eliminate most of the randomness effects. This means that one hour of simulation data is obtained for each combination of wind speed and stability class [5].

The relevant outputs of the simulation are the flapwise and edgewise bending moments of each blade root as well as the tower fore-aft and tower side-side bending moment, corresponding to a total of eight different output parameters.

4.3.2. Stress calculation

These bending moments M have to be converted into stresses in order to be used in the fatigue analysis. Equation 4.7 is used to convert the moments to stresses. The two additional parameters needed for this are the displacement of the material with respect to the neutral axis y and the second area moment of inertia I. For both wind turbines, the blade roots and tower base are cylindrical, meaning y is simply the radius of the cylinder and the moment of inertia can easily be computed if not available in the reference turbine documentation.

$$\sigma = \frac{My}{I}$$ (4.7)

4.3.3. Rainflow counting

After obtaining the stresses, a rainflow counting algorithm is used to extract stress cycles from the data. Two different rainflow counting functions are used in order to visualise the effect of the choice of rainflow counting algorithm on the fatigue results. Both functions are publicly available in MATLAB. The first function was created by Adam Nieslony according to the ASTM standard [6], while the second function is a simplified rainflow counting algorithm created by Yu Gong [7]. Without going into too much detail, the main difference is that the first function takes into account half cycles while the second function does not do this. This leads to the hypothesis that the fatigue damage using the second function will be an overestimation compared to the results according to the ASTM standard since in many instances, the damage of a full cycle will be assumed while in reality the material only experiences half of a load cycle. Note that the simple rainflow counting algorithm outputs stress ranges, these should be converted to stress amplitude before using the values in the remainder of the calculations.

When the stress cycles are obtained for each 10-minute period, these cycles can be converted into a stress histogram. Furthermore, recall that six 10-minute periods are available for each case. The results of these periods are summed in order to obtain the stress histogram of a one hour period. This is more convenient since the DOWA wind speed outputs that will be used to assess the fatigue performance are one hour averages.

---

[5] One simulation of 660 seconds takes around 2 minutes to initialise and around 15 minutes to run making a total of 17 minutes per 660 second simulation (simulation time step is $0.008s$, to be specified in the controls tab under 'sampling time'). Note that six of these simulations are run per wind speed using an HP ZBook Studio G3 laptop with a 2.60 GHz quad-core processor and 8GB of RAM. Note that some time can be saved on the initialisation by inputting multiple wind speeds and seeds before running the simulations.

[6] https://nl.mathworks.com/matlabcentral/fileexchange/3026-rainflow-counting-algorithm

[7] https://nl.mathworks.com/matlabcentral/fileexchange/38834-simple-rain-flow-counting-algorithm

4.3.4. Damage fraction calculation

With the one hour stress histogram, the one hour damage fraction can be computed. This is done based on the S-N curve (also known as the Wöhler curve) of the material. It is difficult to find very detailed material properties of the blades and tower used in the reference turbines. This does not necessarily have to be a limitation since the goal of this research is to compare results, not to design a turbine. This means that the comparison is valid as long as the same material is used for each analysis. This is why the composite blade material of both reference turbines is assumed to be SNL triax, with $b = 10$ according to GL standards and $S_{max} = 700 MPa$ [43]. There are many different types of steel that can be used for the tower. One of the most commonly used types of steel for wind turbine towers is S335, for which $S_{ult} = 400 - 600 MPa$ is a good estimate [44]. This supports the validity of the tower properties specified in table 6 of the IEA task 37 system design report [45]. The S-N curve used for the steel material in the tower is an approximation based on the parameters given in this table and is shown in figure 2.19. There are two slopes in the S-N curve for steel. The first slope is $b = 3$, which changes into $b = 5$ at $5E6$ cycles [46]. The fatigue limit of $36 MPa$ is reached at $1E8$ cycles. The figure indicates that the ultimate stress is located on the S-N curve at around $1E4$ cycles, this is also something that is commonly seen for steel [47][48][49]. Note the assumption that the composite blade does not have a fatigue limit, this means the fatigue results will be conservative. The S-N curves for the blade and the tower material are shown in figure 2.18 and figure 2.19, respectively. With the S-N curve, the one hour fatigue damage for each stress cycle in the stress histogram can be computed. This damage fraction is then multiplied by a safety factor of 1.38, composed of a material safety factor of 1.2 and consequence of failure safety factor of 1.15 as prescribed by IEC standards.

A very important note to make in this approach is the fact that S-N curves are used. These curves do not include the effect of mean stress making the results unrealistic. A better approach would be to use Goodman diagrams that include the effect of mean stress. Unfortunately, the fatigue documentation on composite materials is limited, leaving the Goodman approach for future research.

4.3.5. Fatigue damage calculation

The damage fraction of one hour at a certain mean wind speed is now computed. In order to convert this into the lifetime fatigue damage, the Weibull distribution is used. The Weibull parameters were already computed for each location during the energy yield calculations. Note that the Weibull parameters of the wind speeds without stability corrections have to be used since these corrections apply specifically to energy yield, not to fatigue. With this Weibull distribution, the probability of occurrence of a certain wind speed is known. The lifetime of a turbine is assumed to be 20 years $= 175,320$ hours $= 1,051,920$ 10-minute intervals under the assumption that five leap years are present in every 20 year period. The amount of hours that a certain wind speed occurs over a twenty year period is then: $probability * 175320$ hours. For each wind speed, the amount of hours is then multiplied with the hourly fatigue damage at that wind speed. When the fatigue damage of all wind speeds is summed, the total fatigue damage over a twenty year lifespan is known. Recall that this analysis only includes the fatigue damage accumulated during power production and ignores the wind speed of $3\frac{m}{s}$.

The calculations described above are performed for every location in the DOWA domain. Additionally, the fatigue damage is calculated for three offshore locations for which the DOWA provides 10-minute data. This allows for an analysis of the effect of hourly averaged wind speed values compared to 10-minute values. For the 10-minute values, the approach to calculate the fatigue damage is largely the same. Instead of the hourly damage fraction for a certain mean wind speed, the 10-minute damage fraction is now used. This is assumed to be $\frac{1}{6}^{th}$ of the hourly damage fraction at the same mean wind speed. Additionally, the number of damage fraction values to be summed over the lifetime of 20 years was $175,320$ before. For the 10-minute values, $1,051,920$ damage fraction values have to be included in the analysis for the lifetime of the wind turbine. A final difference between the hourly and 10-minute fatigue analysis are the Weibull parameters used. Since 10-minute values are used, these parameters will differ slightly from the hourly values. It should be noted that taking $\frac{1}{6}^{th}$ of the damage fraction and multiplying the number of fractions used in the analysis by 6 should not have any significant implications on the results. This means that any difference in fatigue damage between hourly and 10-minute values is caused by the difference in Weibull distribution.

$$5$$

Results & Discussion

Using the methods described in chapter 4, results are obtained. The results discussed in this chapter are based on data for the full DOWA domain of the year 2017. Section 5.1 contains the results of the atmospheric stability analysis. The results regarding energy yield are shown in section 5.2 and the results of the fatigue analysis are provided in section 5.3.

5.1. Atmospheric stability

The stability results are obtained using the methods described in section 4.1. These results include the occurrence of low level jets, stability estimations based on Obukhov length, shear exponent and temperature profile as well as stability histograms for several offshore locations. Finally, the turbulence intensity will be analysed based on 10-minute wind speed mean and standard deviation values provided by the DOWA for three offshore locations. Some example wind speed and temperature profiles of fits that were obtained during the calculation of these results are shown in appendix A.

Figure 5.1 shows the occurrence of low level jets as percentage of the total number of hours in 2017. This percentage varies significantly from 6% in the north of the domain to more than 15% at some locations along the British coastline. Figure 5.2 shows the same data expressed in absolute values, with the maximum being 8760 hours in the year 2017. These low level jet occurrences should be kept in mind when analysing the stability figures. Note that the coastlines are shown by a red line in the figure.
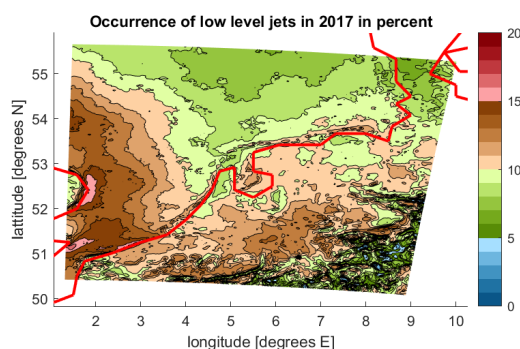
**Figure 5.1:** Low level jet occurrences in percent
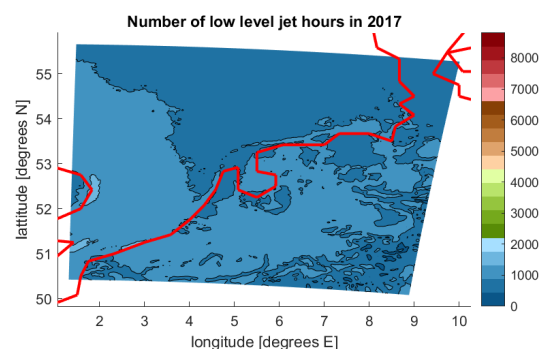
Figure 5.2: Low level jet occurrences in absolute values

An analysis was also performed on the mean height and wind speed of these low level jets. Figure 5.3

shows the mean low level jet height in 2017 while figure 5.4 shows the standard deviation of these heights.
The coastline is indicated by the red line. There are four blue dots on the figures as well, these represent the
three offshore wind farms Borssele, HKZ and HKN from southwest to northeast along the Dutch coastline.
The IJmuiden meteorological mast is located further offshore. Low level jets are found at heights in the
range of $100 - 170$ metres. For offshore locations near the coastline, low level jets occur at slightly lower
heights than for far offshore or onshore locations. The standard deviation of these heights is lowest for far
offshore locations.
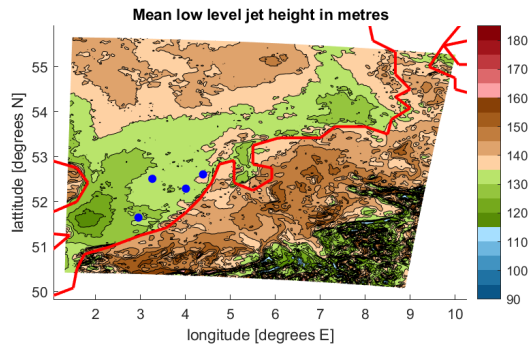
Figure 5.3: Mean low level jet height in 2017
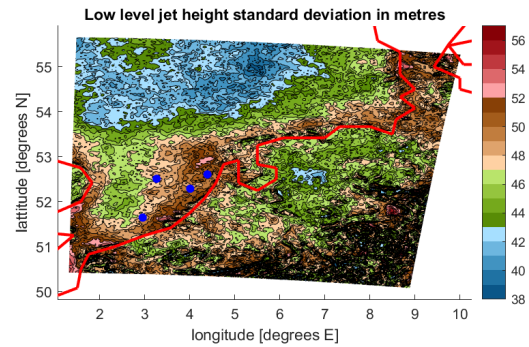
Figure 5.4: Low level jet height standard deviation in 2017

The wind speed of these low level jets was also analysed. Figure 5.5 shows the mean LLJ wind speed
while figure 5.6 shows the standard deviation of these wind speeds. As expected, the wind speeds are
larger for further offshore locations. The standard deviation is lowest onshore, while it is largest in the
offshore area between the Dutch and British coastline. Note that these standard deviations should be
interpreted together with the magnitude of the mean wind speed.
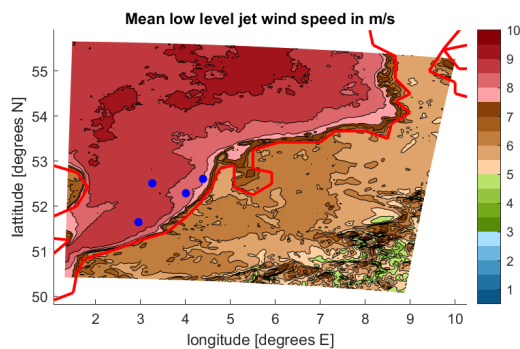
Figure 5.5: Mean low level jet wind speed in 2017
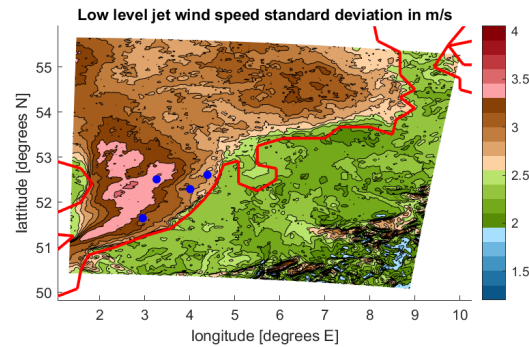
Figure 5.6:
Low level jet wind speed standard deviation in 2017

The DOWA project already included an analysis of low level jets at the MMIJ location. In the public final
report, it was found that low level jets occur at this location around 4% of the time while this is found the
be over 10% in figure 5.1[11]. Note that in the DOWA report, four years were analysed and different iden-
tification parameters were used. The LLJ analysis in the DOWA project uses identification parameters
based on previous publications [40]. In that publication, a low level jet is identified when the difference
between the minimum and the maximum wind speed is at least $2\frac{m}{s}$, while a difference of only $0.5\frac{m}{s}$ is
used to generate the results shown in figure 5.1. In the paper used for the DOWA project, a sensitivity
analysis was also performed. It was found that when the threshold was decreased from $2\frac{m}{s}$ to $1.5\frac{m}{s}$, the

percentage of occurrence of low level jets at the MMIJ location increased from 4.6% to 6.9%. This makes it plausible that a further threshold decrease to $0.5\frac{m}{s}$ would increase the percentage of occurrence to the value of 12.3% that was found for the MMIJ location in this report. To verify this, the threshold value was changed from $0.5\frac{m}{s}$ to $2\frac{m}{s}$ for the MMIJ location and the resulting LLJ occurrence was found to be 2%. In the DOWA project, the mean wind speed of low level jets at MMIJ was found to be $9.28\frac{m}{s}$ with a mean height of $101.51m$. This mean wind speed is very similar to what can be seen in figure 5.5 while the mean height shown in figure 5.3 is significantly larger. Note that the DOWA study uses LiDAR measurements to determine LLJ characteristics, potentially causing these discrepancies.

To justify the use of a $0.5\frac{m}{s}$ threshold, a vertical wind speed profile is shown in figure 5.7. In this profile, the threshold value of $0.5\frac{m}{s}$ is barely met, but based on visual inspection this looks like the correct identification of a low level jet. A downside of this lower threshold is shown in figure 5.8, where a low level jet is falsely identified. This should always be kept in mind when interpreting the results.
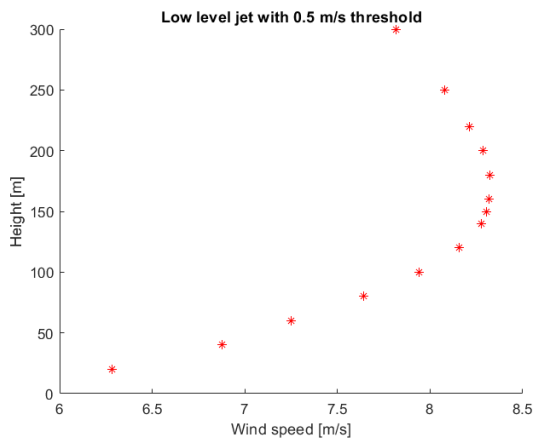
**Figure 5.7:** Low level jet profile with $0.5\frac{m}{s}$ threshold
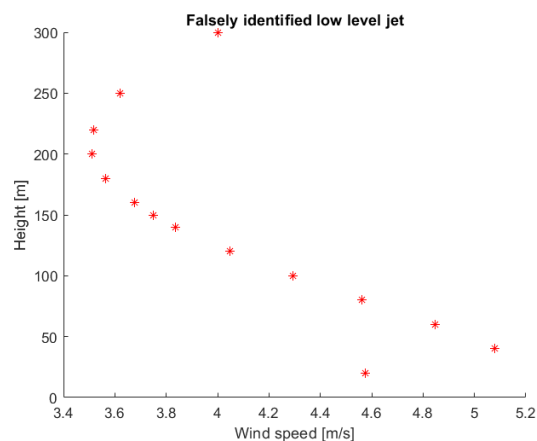
Figure 5.8: Falsely identified low level jet profile

Figure 5.9 and figure 5.10 show the discarded values of wind shear exponent and Obukhov length, respectively. The figures represent a height of $150m$ and the values are expressed as a percentage of the total number of hours in 2017 without low level jets. Both approaches confirm that a larger percentage of values is discarded onshore compared to offshore. Again, the coastlines are indicated by a red line. The four blue dots again represent the three offshore wind farms Borssele, HKZ and HKN from southwest to northeast along the Dutch coastline and the IJmuiden meteorological mast. The differences between the shear exponent and the Obukhov length can arise both from the theory behind the models and the parameters specified in section 4.1. The Obukhov length method discards a significantly larger amount of values, this is because it discards all values of $Ri > 0.2$ as it is outside the validity of the equation used to calculate the Obukhov length. The amount of values discarded for the same analyses for a height of $90m$ are similar in pattern but slightly lower and can be found in appendix A. Note that no values are discarded in the temperature profile approach, hence the results are not shown in a figure. The percentage of low level jets in combination with the percentage of discarded values after subtraction of the low level jets is important to keep in mind for the following analyses.
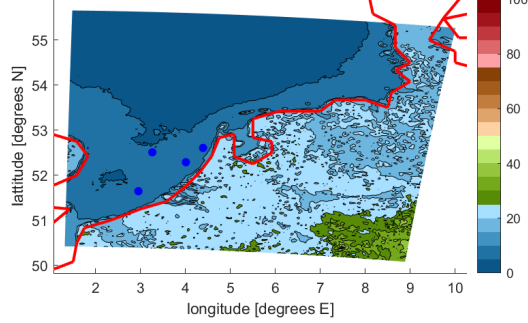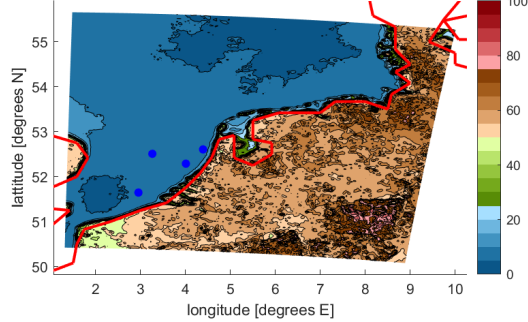
Figure 5.9: Wind shear exponent, 150m, discarded
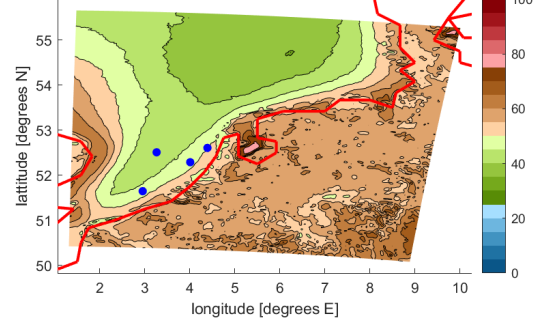
Figure 5.10: Obukhov length, 150m, discarded

Figure 5.11: Wind shear exponent, 150m, stable
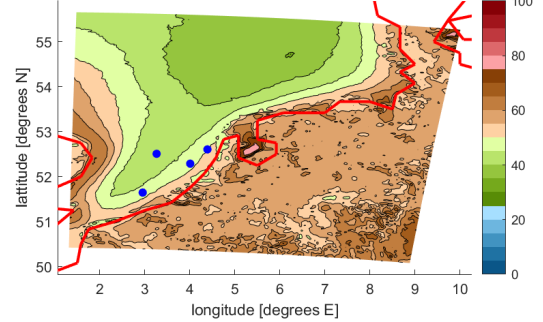
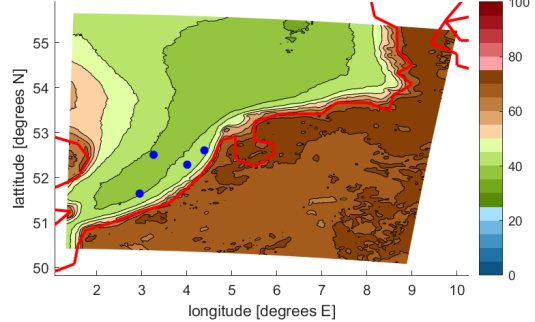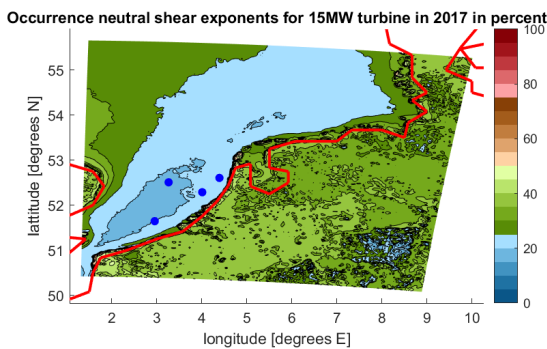**Figure 5.12:** Obukhov length, 150m, stable

Figure 5.13: Temperature profile, 150m, stable

Figure 5.11, figure 5.12 and figure 5.13 show percentage of occurrence of wind shear exponent, Obukhov length and temperature profile under stable atmospheric conditions, respectively. All figures represent a height of $150m$ and the values are expressed as the percentage of non-discarded values after subtraction of the low level jets cases. Note that this is different for the temperature profile, since low level jet cases are included in the analysis and no values are discarded. This means that the percentages of stable values, neutral values and unstable values of a certain parameter add up to 100% for all approaches. When looking at the figures it is clear that for onshore locations, around $50-70\%$ of the atmospheric conditions are stable according to the wind shear exponent, Obukhov length and the temperature profile. Offshore,

the three approaches do not confirm each other. The results of the temperature profile and the Obukhov length are in the same range of $35-50\%$, but the shear exponent indicates almost no stable atmospheric conditions for offshore locations.

Figure 5.14, figure 5.15 and figure 5.16 show the percentage of values classified as neutral by the wind shear exponent, Obukhov length and temperature profile, respectively. The figures represent results at a height of $150m$ and the values are expressed as percentage of non-discarded values and excluding low level jets, except for the temperature profile approach. Looking at the figures, significant differences between the approaches can be found. The wind shear exponent shows an interesting pattern offshore; parallel to the Dutch coastline, the amount of neutral values first decreases with offshore distance only to increase again when the distance to the coastline is increased further. This region of the lowest amount of neutral values corresponds to the channel between the British and Dutch coastline when the wind is coming from the southwest, the most dominant wind direction. The Obukhov length results do not show this pattern. The Obukhov length shows a decrease in neutral values with increase in offshore distance. The temperature profile results show a slightly lower amount of neutral values than the other two approaches.

So far, the stable and neutral values as well as the discarded values of each stability parameter at $150m$ have been shown. The unstable values will not be shown here, as they are simply a combination of the other results and are deemed redundant. For completeness, the results for unstable classification can be found in appendix A.

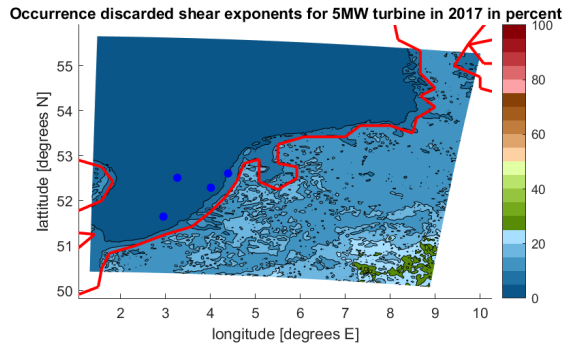**Figure 5.14:** Wind shear exponent, 150m, neutral
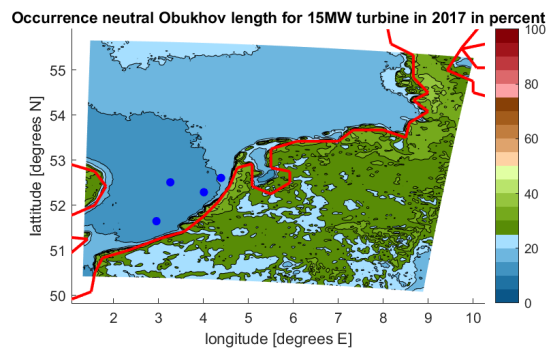
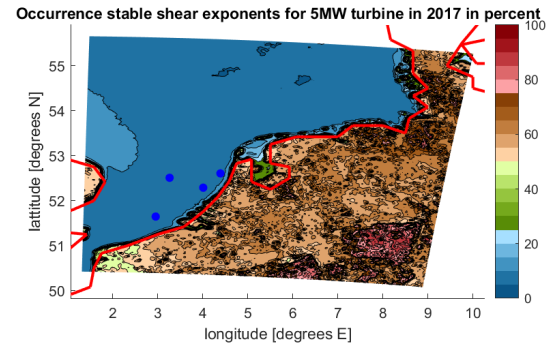**Figure 5.15:** Obukhov length, 150m, neutral
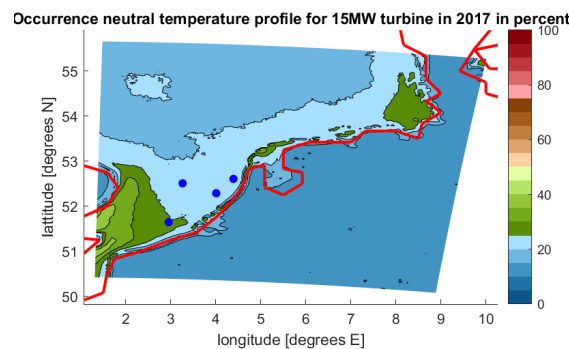
Figure 5.16: Temperature profile, 150m, neutral

A comparison between the discarded, stable, unstable and neutral values for the wind shear exponent at $90m$ is made in figure 5.17, figure 5.18, figure 5.19 and figure 5.20, respectively. Note again that the discarded values are expressed as a percentage of the total number of hours in 2017 excluding low level jets, while the other three parameters are expressed as a percentage of the non-discarded values. Just like for the height of $150m$, a larger amount of values is discarded onshore compared to offshore locations.
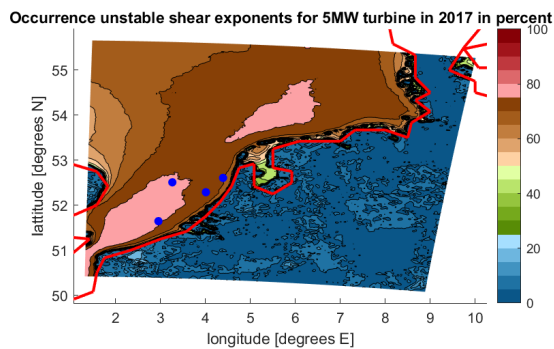
According to the wind shear exponent at $90m$, the number of stable values is larger onshore while the opposite observation can be made for the unstable values. The pattern of neutral shear exponents looks similar to the one at a height of $150m$.
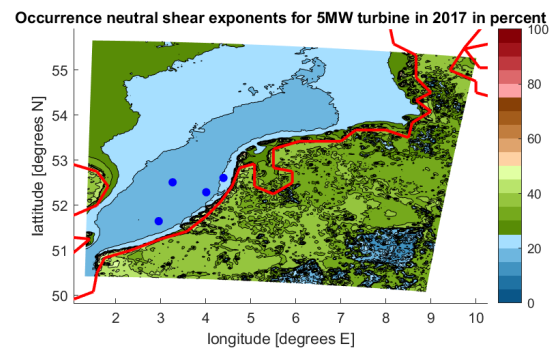

Figure 5.17: Wind shear exponent, 90m, discarded

Figure 5.18: Wind shear exponent, 90m, stable

Figure 5.19: Wind shear exponent, 90m, unstable

Figure 5.20: Wind shear exponent, 90m, neutral

A comparison between the stable, unstable and neutral values for the temperature profile at $90m$ is made in figure 5.21, figure 5.22 and figure 5.23, respectively. It is immediately clear that almost no values are neutral. A reiteration of the criteria to classify temperature profiles into stability classes is recommended. The figures of stable and neutral values are each others inverse, as is to be expected considering no values are discarded. Note that the results of the Obukhov length approach are not shown for the height of $90m$ as discussion would be largely the same as for the height of $150m$. For completeness, these results are included in appendix A. For all stability results, percentages have been plotted in this section. The absolute values of these results are presented in appendix A.
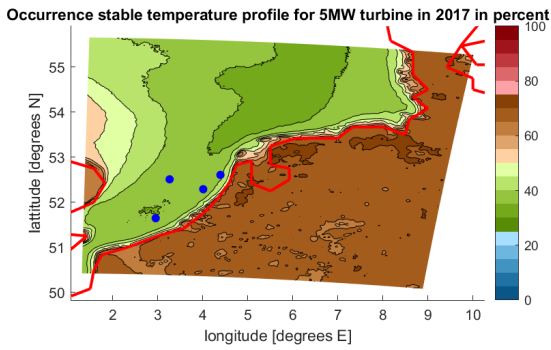
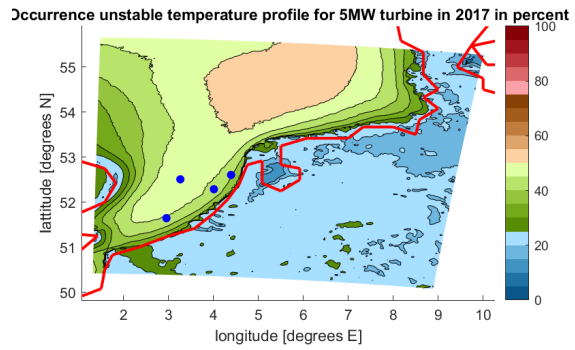**Figure 5.21:** Temperature profile, 90m, stable

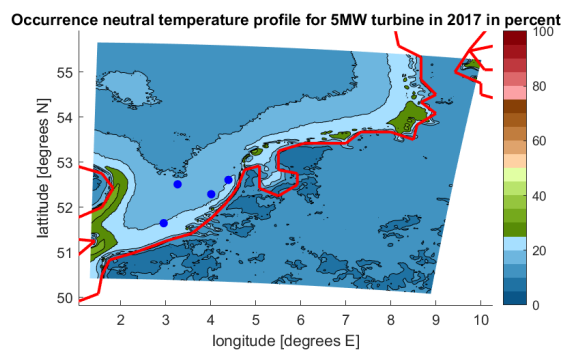**Figure 5.22:** Temperature profile, 90m, unstable

Figure 5.23: Temperature profile, 90m, neutral

Figure 5.24, figure 5.25, figure 5.26 and figure 5.27 show the stability histograms based on the shear exponent for Borssele, HKZ, HKN and MMIJ, respectively. The results show that for increasing wind speed, the amount of low level jets decreases and the amount of neutral values increases. In all locations, unstable atmospheric conditions are dominant fo every wind speed.
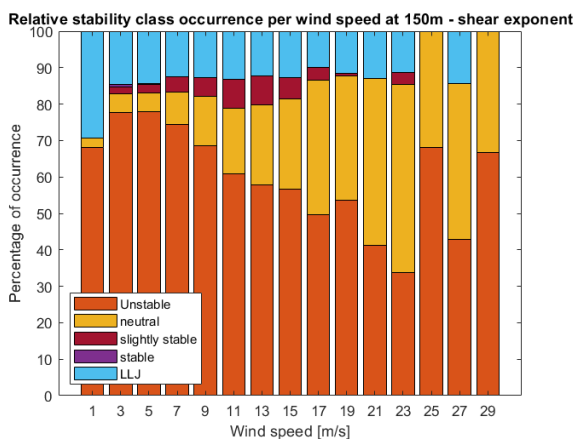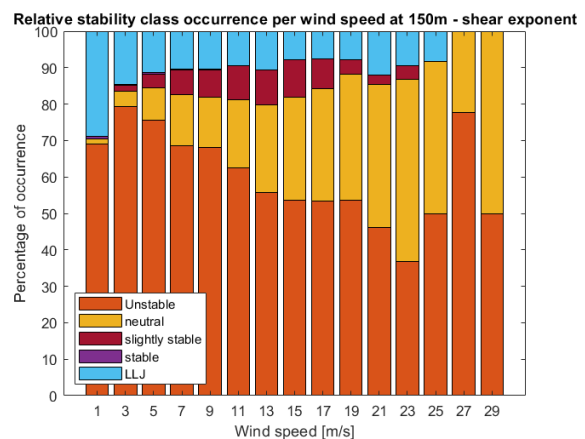

Figure 5.24: Stability histogram Borssele

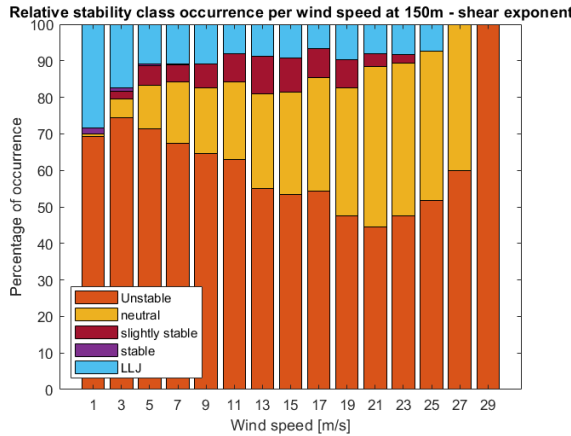**Figure 5.25:** Shear exponent stability histogram HKZ

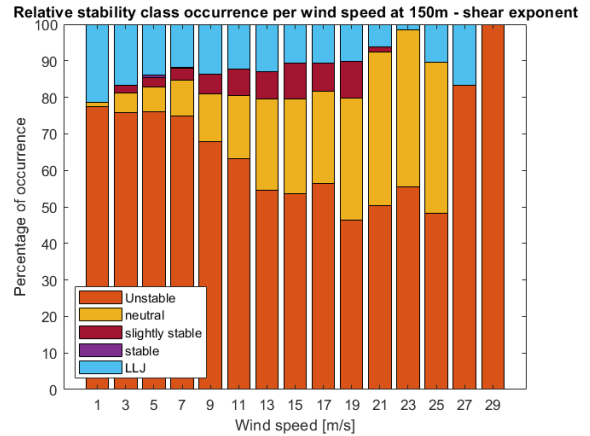**Figure 5.26:** Shear exponent stability histogram HKN

Figure 5.27: Shear exponent stability histogram MMIJ

Figure 5.28, figure 5.29, figure 5.30 and figure 5.31 show the stability histograms based on the Obukhov length for Borssele, HKZ, HKN and MMIJ, respectively. These figures show that the amount of unstable values significantly reduces with wind speed while the amount of low level jets stays more or less constant. The trend of decreasing number of unstable values with increasing wind speed is also found in literature, while the number of stable values is very low [24]. This may be caused by the fact that low level jets contain mostly stable values or the fact that the classification parameters need some iteration.
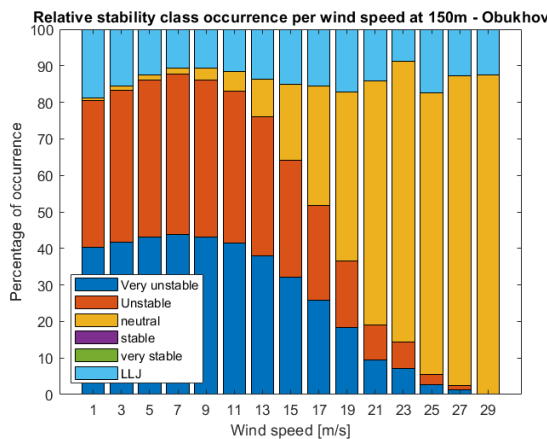

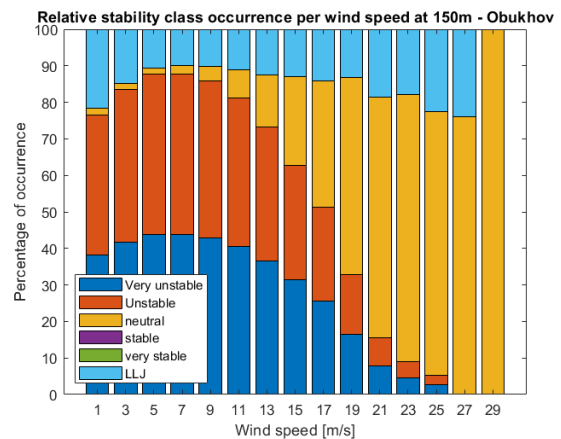**Figure 5.28:** Obukhov length stability histogram Borssele

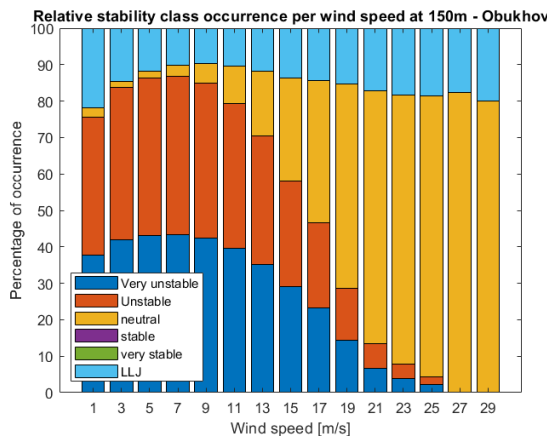**Figure 5.29:** Obukhov length stability histogram HKZ

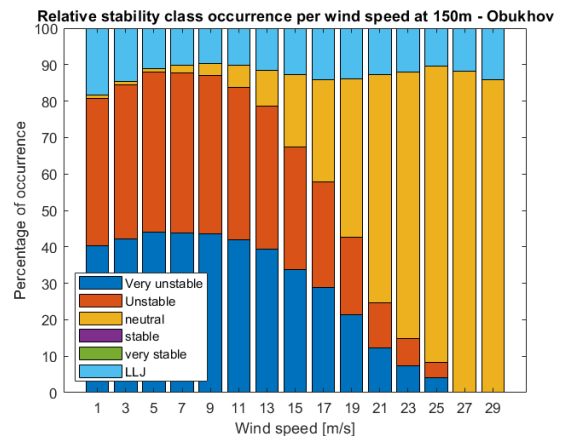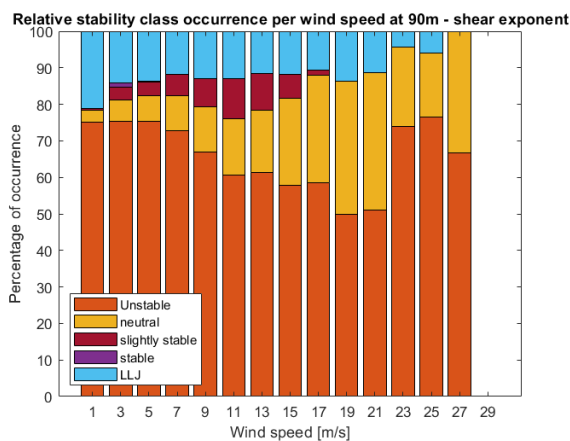**Figure 5.30:** Obukhov length stability histogram HKN

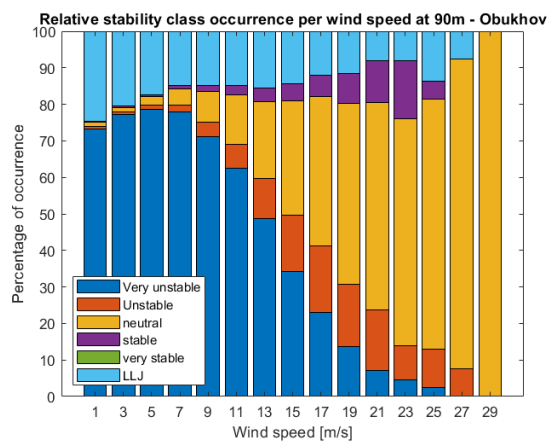**Figure 5.31:** Obukhov length stability histogram MMIJ

The histograms shown above apply to a height of $150m$. Figure 5.32 and figure 5.33 show the stability histograms for the Borssele wind farm location at a height of 90m using the shear exponent and Obukhov length, respectively. This allows for a comparison of stability between different heights. The main difference can be found in the Obukhov length comparison, where there is a significantly larger amount of stable values.

These figures can also be compared to figure 5.34 and figure 5.35 showing the stability histogram using 10-minute values for the shear exponent and Obukhov length, respectively. For the Obukhov length approach, there is a significantly lower amount of low level jets at higher wind speeds. This cannot be seen in the shear exponent histograms, where the 10-minute values indicate a lower amount of neutral values compared to the hourly values. This lower amount of neutral values is mainly caused by an increase in low level jets for these wind speeds. Note that several histograms like the temperature profile values are not shown, these can be found in appendix A.

When comparing these stability histograms to literature, significant differences can be found [22][24]. A very low amount of stable and very stable atmospheric conditions is identified. This could be caused by the large amount of discarded values for the Obukhov length or differences in reference height between the methods used in this report and the literature.
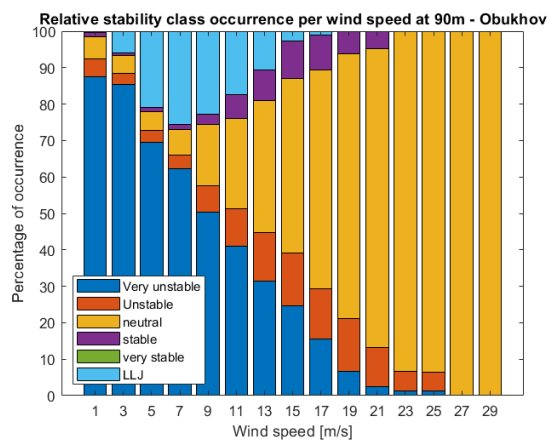

Figure 5.32: Shear
exponent stability histogram Borssele, hourly values

Figure 5.33: Obukhov
length stability histogram Borssele, hourly values
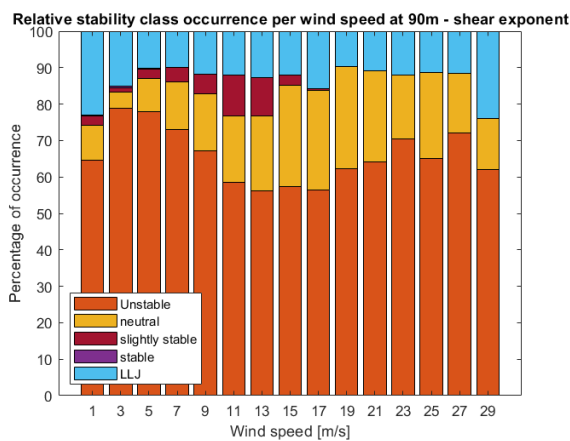
Figure 5.34: Shear
exponent stability histogram Borssele, 10-minute values

Figure 5.35: Obukhov
length stability histogram Borssele, 10-minute values

The turbulence intensity is plotted against wind speed in figure 5.36 and figure 5.37 for a height of $93m$ and $148m$, respectively. The standard deviation of the turbulence intensity for each wind speed is shown in the graphs as well. The turbulence intensity values of the three wind farms are very similar. A possible

explanation for this is the fact that they are located approximately at the same distance from the Dutch coastline. However, it is most likely that these similarities are caused because the turbulence intensities were prescribed values in the LES model used to generate this data. The reason for this is that the model was developed to account for added turbulence due to the presence of wind turbines, meaning free stream initial and boundary values were prescribed [35]. For the purpose of this report however, free stream data was used, yielding only the prescribed TI values. If this is the case, it will become clear during the validation with site measurements in chapter 6.
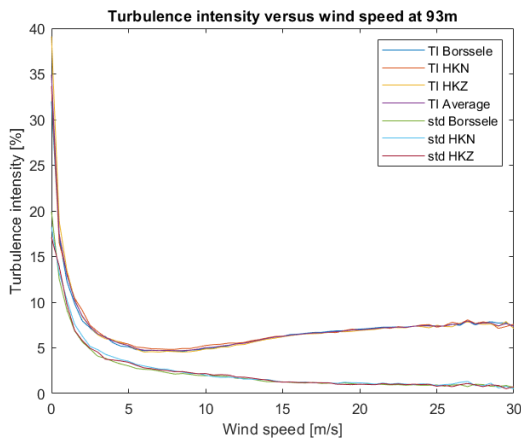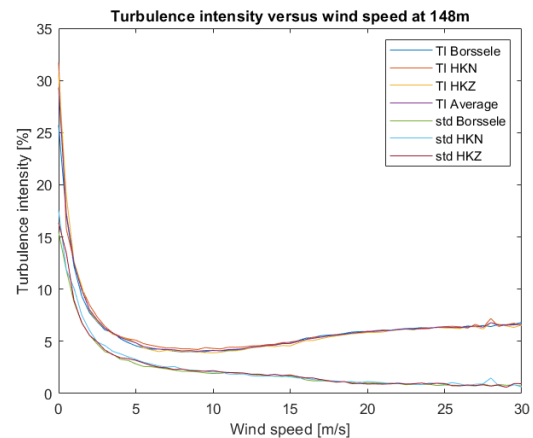

Figure 5.36: Turbulence intensity at 93m

**Figure 5.37:** Turbulence intensity at 148m

5.2. Energy yield

In this section, the results regarding energy yield are shown for the $5MW$ and $15MW$ wind turbines according to the method described in section 4.2. The figures cover the full DOWA domain and wind farms Borssele, HKZ and HKN are shown by blue dots along the coastline from southwest to northeast, respectively. The coastline is shown by a red line. A short verification of the turbulence intensity correction is provided in appendix B.

Figure 5.38 and figure 5.39 compare the energy yield of the 5MW reference turbine for the case with and without stability corrections, respectively. Figure 5.40 and figure 5.41 do the same for the 15MW reference turbine. When comparing the cases with and without stability correction, the differences seem relatively small at first sight. When comparing the 5MW to the 15MW turbine, the same patterns can be seen, meaning the energy output increases with increasing offshore distance. Onshore, the energy yield drops significantly as expected due to the large differences in mean wind speed. To give a sense of distance, figure 5.42 and figure 5.43 show the energy yield as a function of distance to the coastline. The location of these figures is indicated by the black line in figure 5.38 and figure 5.40. Negative distance values represent onshore locations and positive distance values represent offshore locations. Note that this is just an approximation of the distance, the accuracy is limited due to the resolution of the coastline coordinates and the orientation of the DOWA grid points.
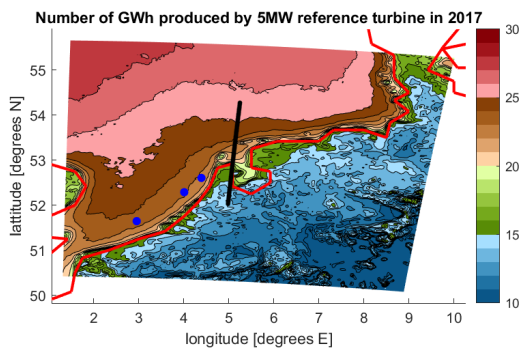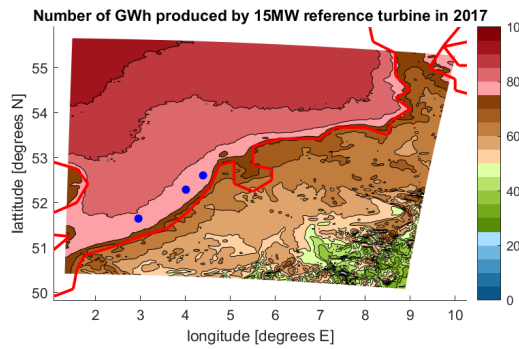
Figure 5.38:
NREL 5MW turbine energy yield with stability correction
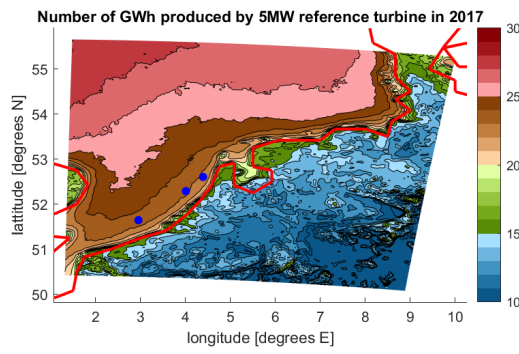
Figure 5.39: NREL
5MW turbine energy yield without stability correction
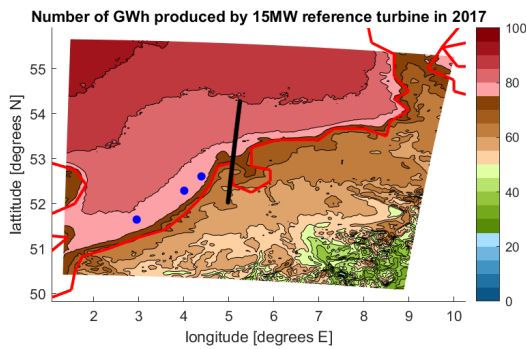
Figure 5.40:
IEA 15MW turbine energy yield with stability correction

Figure 5.41: IEA
15MW turbine energy yield without stability correction
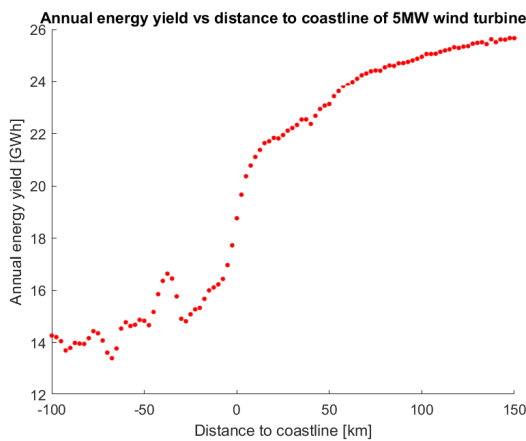
Figure 5.42:
5MW turbine energy yield vs distance to coastline
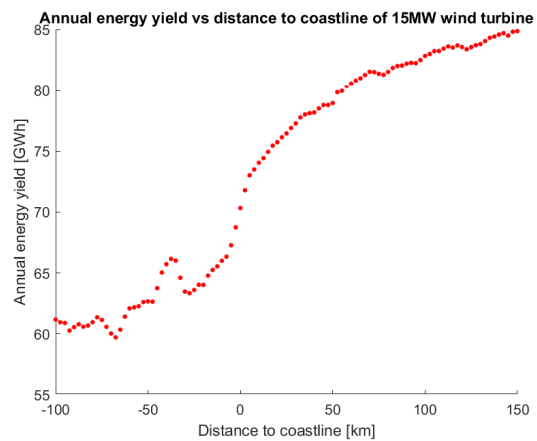
Figure 5.43:
15MW turbine energy yield vs distance to coastline

Figure 5.44 shows the ratio of the energy yield of the $15MW$ reference turbine with and without stability correction. In this figure, it is clearly visible that the energy yield with stability correction is lower than the energy yield without stability correction. Figure 5.45 shows the same data for the $5MW$ reference turbine. Here, the pattern is more interesting since onshore, the energy yield with stability correction is larger

than without correction while offshore, the ratio is around 1. To explain this, the applied corrections are analysed in more detail in figure 5.46, figure 5.47 and figure 5.48 showing the ratios of the wind speeds with and without density, shear and turbulence intensity correction, respectively. The turbulence intensity correction uniformly increases the wind speed as is to be expected from equation 2.19, but offshore this is counteracted by a combination of density and shear correction. This results in a corrected energy yield that is lower than the uncorrected value offshore, but larger onshore. The effect of each individual correction on wind speed is shown for the height of $90m$ only. The results for a height of $150m$ can be found in appendix B. For the $15MW$ wind turbine, the wind shear correction is largely responsible for the ratio of energy yield with and without stability lower than 1 shown in figure 5.44.

This analysis shows that considering stability, especially wind shear, in the energy yield analysis becomes more important as wind turbine hub height and rotor diameter increases because a seemingly small energy yield deficit can have very large consequences for the cost of energy and revenue of a wind farm [1].
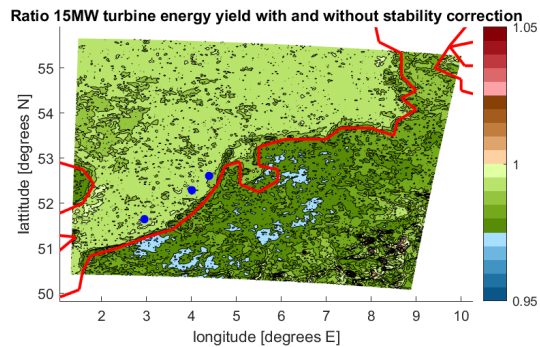

Figure 5.44: Ratio of energy yield with and without stability correction, 15MW reference turbine
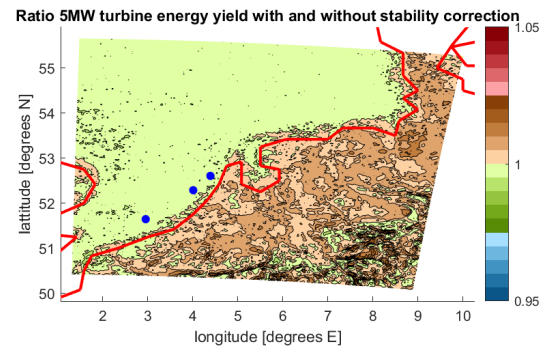
Figure 5.45: Ratio of energy yield with and without stability correction, 5MW reference turbine

---

[1] For the $15MW$ turbine, energy yield ratio's as low as 0.975 are shown for some onshore locations and for offshore locations, the lowest ratio's can be found around 0.99. This means that onshore, there is a 2.5% deficit and offshore there is a 1% deficit in energy yield compared to the calculations without corrections. Comparing this to the number of GWh per year produced in these locations, the deficit is around $1.4GWh$ onshore and $0.85GWh$ offshore. These values in turn correspond to a revenue loss of €560.000 onshore and €340.000 offshore over the complete wind turbine lifetime of 20 years, based on a revenue of $20\frac{€}{MWh}$. Note that these are losses for a single wind turbine, so in case of a wind farm with multiple turbines, these losses will be orders of magnitude larger. This shows that not including stability in wind farm design can have significant effects on the levelised cost of energy and return of investment.
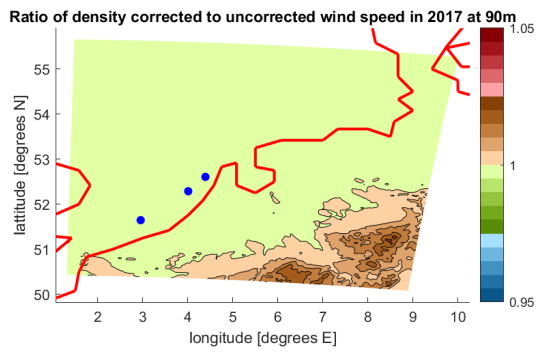
Figure 5.46:
Ratio of wind speed with and without density correction
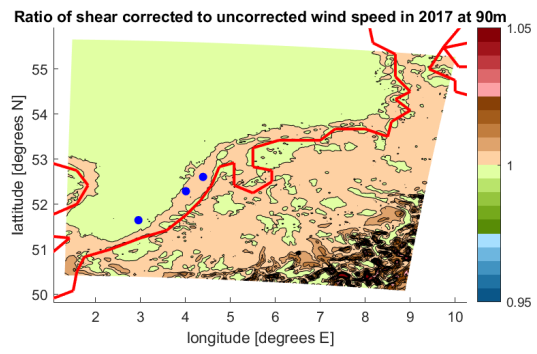
Figure 5.47:
Ratio of wind speed with and without shear correction
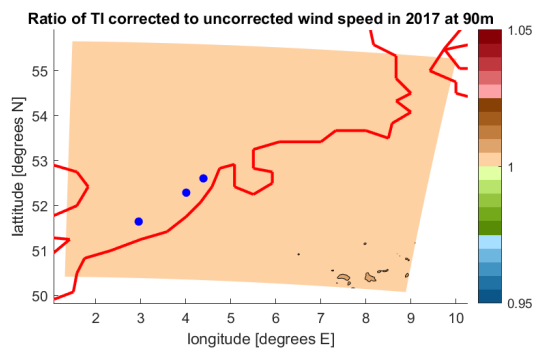
Figure 5.48:
Ratio of wind speed with and without TI correction

Figure 5.49:
150m Weibull scale parameter with stability correction

Figure 5.50:
150m Weibull scale parameter without stability correction

Figure 5.51:
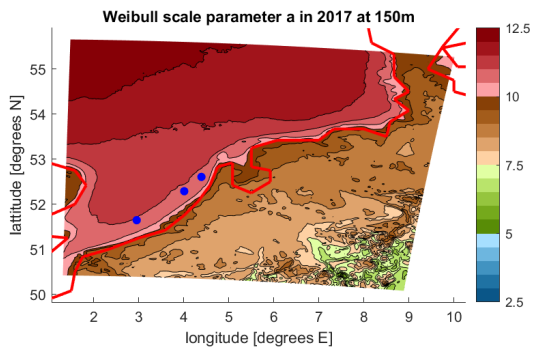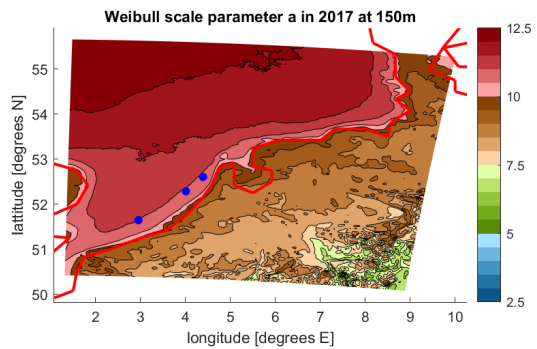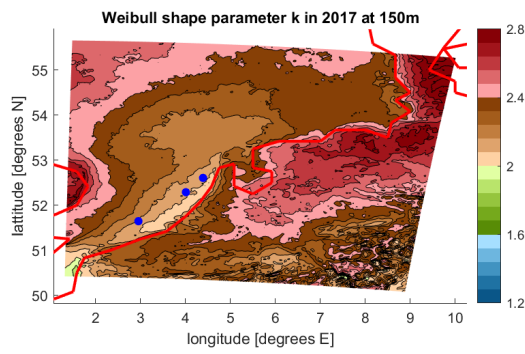150m Weibull shape parameter with stability correction
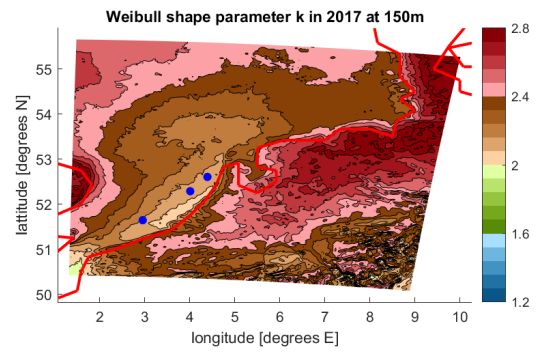
Figure 5.52: 150m
Weibull shape parameter without stability correction

The Weibull scale parameter 'a' with and without stability correction at $150m$ is shown in figure 5.49 and figure 5.50, respectively. No significant differences are observed associated to stability correction, even though significant difference in energy yield were observed. This means that only a slight change of the Weibull parameters can already have a large impact on the energy yield of a wind turbine. When comparing the shape parameter in figure 5.51 and figure 5.52, the same can be said. It is clear that the scale parameter increases for offshore locations, as it is related to the mean wind speed. The shape parameter appears to be influenced by the English channel between the British and European land masses as this is the most dominant wind direction. In the extent of the Channel, values of the shape parameter are slightly lower, where they increase again toward the further offshore locations and to the northeast of the Netherlands.
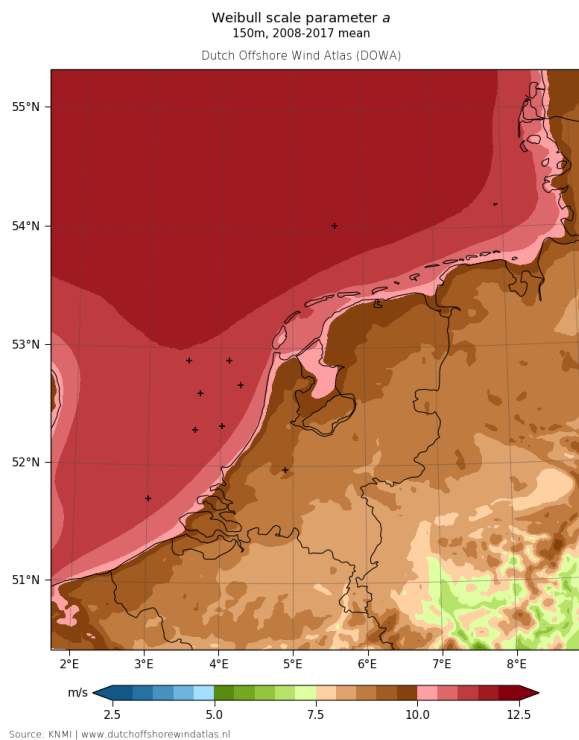
Figure 5.53: DOWA 150m Weibull scale parameter
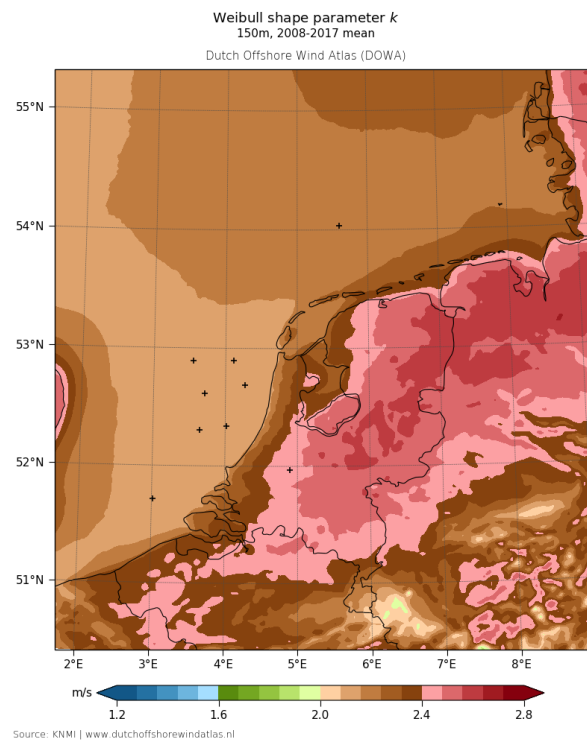
Figure 5.54: DOWA 150m Weibull shape parameter

As a form of verification, the Weibull parameters at a height of $150m$ can be compared to the DOWA results for the scale and shape parameter in figure 5.53 and figure 5.54 that were found on the DOWA

website [2]. The values found for the scale parameter 'a' seem to match up relatively well, while the values of the shape parameter k are more uniform offshore in the DOWA. However, the trend seen in the results that k increases onshore in the northeastern part of the Netherlands seems to hold. Note that the DOWA values span a time period of 10 years, while the values shown previously in this section are for the year 2017 only. Additionally, the Weibull values in the DOWA project are estimated using the methods established by Wieringa and Rijkoort [50]. This can partially explain some of the differences with the Weibull parameters shown in figure 5.50 and figure 5.52, that were determined using the European Wind Atlas method.

Table 5.1 shows the Weibull parameters and energy yield at three wind farm locations using different simulation data, methods and temporal resolutions. The first aspect of this table to consider is the comparison between the DOWA nondirectional, DOWA hourly and analytical values. The difference between these three is the method used to calculate the energy yield. For the DOWA nondirectional results, a single Weibull fit is obtained for all wind speed values. This is different from the DOWA hourly values, that uses a Weibull fit for every wind direction sector according to the European Wind Atlas method as explained in chapter 4. The DOWA data values represent the energy yield without fitting a Weibull distribution, this method simply calculates the power produced for every wind speed value in the data. Note that the same input data is used for these three methods. When comparing these DOWA results, it can be seen that the energy yield calculated using the European Wind Atlas method can differ significantly from the energy yield calculated when only one Weibull curve is fitted. The largest difference is observed at the HKZ location and can be explained by looking at figure 5.55 and figure 5.56. These figures show the Weibull fit obtained in the European Wind Atlas method for the sector with directions between $60°$ and $90°$ and the Weibull fit obtained by fitting all wind speed values to a single Weibull curve, respectively. Both Weibull fits are obtained for the HKZ location at a height of $150m$, but it is clear that the wind speed for certain sectors does not follow a smooth Weibull curve. In this specific case, using all wind speed data without dividing into direction sectors yields a better Weibull fit. This verification shows that one should always be careful when using Weibull parameters to calculate energy yield, especially when a limited number of values are used to obtain the fit as is the case here. For the wind direction sector in figure 5.55, only 515 values are present out of 8760 hourly wind speed values in the year 2017. For the other wind farm locations, the opposite can be said. For the Borssele and HKN location, the European Wind Atlas method calculates energy yield values closer to the data than the verification method.

As an additional form of verification, an analytical expression was used to calculate the energy yield based on wind turbine specifications and Weibull parameters. This analysis is performed to verify the accuracy of the code to calculate the energy yield from the Weibull curve and the power curve. The analytical expression that was used is given by equation 5.1 and equation 5.2 [51]. In equation 5.2, e is a dimensionless energy yield parameter. x_{ci}, x_r and x_{co} are the cut-in, rated and cut-out wind speed normalised with the mean wind speed, respectively. This means that $x_{ci} = \frac{U_{ci}}{\bar{U}}$, $x_r = \frac{U_r}{\bar{U}}$ and $x_{co} = \frac{U_{co}}{\bar{U}}$ where $\bar{U}$ can be easily computed using the gamma function as was already explained in chapter 4 regarding equation 4.3. In equation 5.2, E is the energy yield, T is the number of hours, $C_{p,max}$ is the maximum power coefficient, η_{max} is the maximum wind turbine efficiency, ρ is the air density which is assumed to be $\rho = 1.225 \frac{kg}{m^3}$ and R is the rotor radius. Note that $C_{p,max}\eta_{max}\frac{1}{2}\bar{U}^3\pi R^2$ is simply the output power of the wind turbine at the mean wind speed. The parameters necessary for this analysis were taken from the NREL $5MW$ and IEA $15MW$ reference turbine reports [52][53]. From the results it can be seen that the energy yield values obtained with the analytical expression are in all cases $1 - 3\%$ larger than the results obtained during the previous analyses. Differences can originate from small inaccuracies in the power curve that was used in the simulations or the resolution of the Weibull fit used for the energy calculations. This verification serves as a sanity check on the energy results obtained with the other analyses in order limit the probability of bugs being present in the energy yield code. Note that the Weibull values given in table 5.1 are rounded to one decimal. For the analytical calculations, the exact numbers were used.

$$e = x_{ci}^3 e^{-\frac{\pi}{4}x_{ci}^2} - x_r^3 e^{-\frac{\pi}{4}x_{co}^2} - \frac{6}{\pi}\left\{ x_r e^{-\frac{\pi}{4}x_r^2} - x_{ci} e^{-\frac{\pi}{4}x_{ci}^2} \right\} + \frac{6}{\pi}\left\{ \text{erf}\left(\frac{\sqrt{\pi}}{2}x_r \right) - \text{erf}\left(\frac{\sqrt{\pi}}{2}x_{ci} \right) \right\} \tag{5.1}$$

$$E = e \cdot T C_{p,max}\eta_{max}\frac{1}{2}\rho\bar{U}^3\pi R^2 \tag{5.2}$$

---

[2]https://www.dutchoffshorewindatlas.nl/atlas/image-library/image-library/
parameters-per-height-150m

Table 5.1: Weibull parameters
and energy yield for three wind farm locations at $150m$ using different methods and temporal resolutions

Parameter		a[-]	k[-]	Energy yield [GWh]
Borssele	DOWA nondirectional	10.9	2.1	77.8
	DOWA hourly	-	-	78.1
	DOWA data	-	-	78.4
	Analytical	-	-	78.9
	LES hourly	10.7	2.0	76.1
	LES 10-minute	10.6	2.0	76.0
HKZ	DOWA nondirectional	10.9	2.1	76.9
	DOWA hourly	-	-	77.8
	DOWA data	-	-	76.9
	Analytical	-	-	78.6
	LES hourly	10.8	2.0	76.9
	LES 10-minute	10.8	2.0	76.7
HKN	DOWA nondirectional	10.9	2.1	77.1
	DOWA hourly	-	-	76.6
	DOWA data	-	-	76.7
	Analytical	-	-	78.6
	LES hourly	11.1	2.1	78.4
	LES 10-minute	11.1	2.1	78.2

Up until now, only the DOWA hourly data was used for the analyses. However, 10-minute LES data is also available for these three wind farm locations. These 10-minute values were also averaged into hourly values to allow for a sensitivity analysis of the temporal resolution. In table 5.1, it can be seen that the difference between 10-minute and hourly LES results is relatively small, especially considering the error that could be introduced by the Weibull fit. For the HKZ location, the LES results are very close to the DOWA hourly results. For the other wind farm locations however, the LES and DOWA values are very different. Note that the Borssele wind farm LES dataset is missing data for May 12th, 2017. This analysis was also performed for the $5MW$ reference turbine, the results of this can be found in appendix B. A verification of the energy content in the Weibull fit was also performed in order to make sure the Weibull curve satisfies the first condition of the European Wind Atlas method. This verification can be found in appendix B.4.
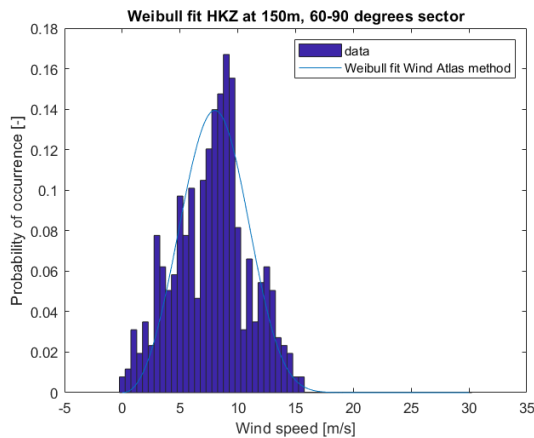
Figure 5.55:
Weibull fit HKZ wind farm at 150m, sector $60° - 90°$
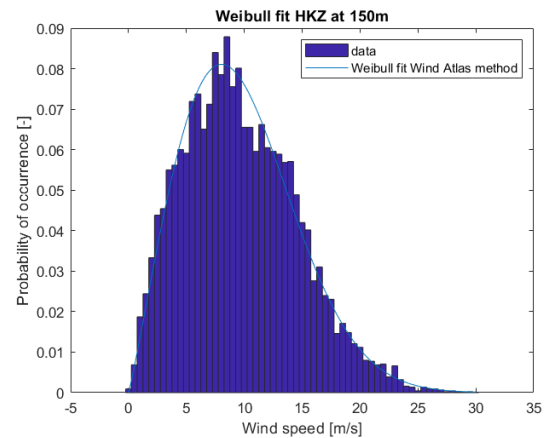
Figure 5.56:
Weibull fit HKZ wind farm at 150m, all directions

An analysis was also performed on the dominant wind direction in the year 2017. This can be useful for wind farm design in order to account for wake losses. Figure 5.57 shows the dominant wind direction at $150m$ while figure 5.58 shows the dominant wind direction at $90m$. Both figures look similar, with dominant wind directions ranging from 200 degrees in the offshore region between the Dutch and British coastline to around 300 degrees in the northern part of the Netherlands.
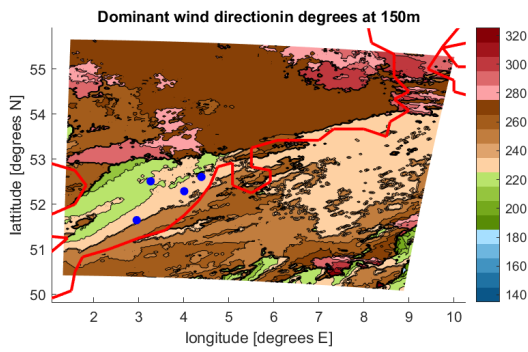
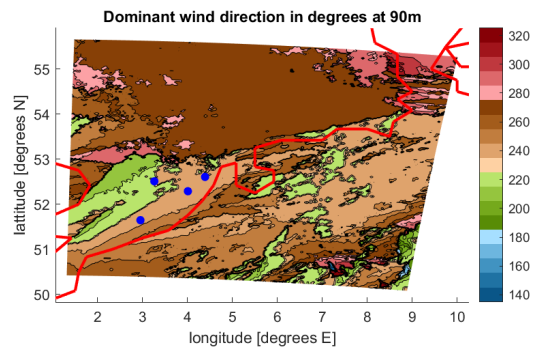**Figure 5.57:** Dominant wind direction at 150m

Figure 5.58: Dominant wind direction at 90m

Figure 5.59 and figure 5.60 show the wind rose at 150m for the HKN and MMIJ locations, respectively. Wind roses for other locations will be shown in chapter 6 while wind roses at $90m$ can be found in appendix B.
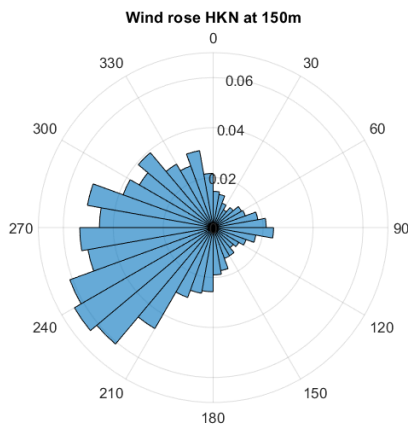

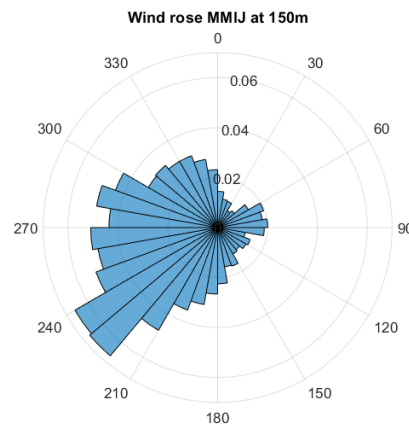**Figure 5.59:** Wind rose at HKN location at 150m

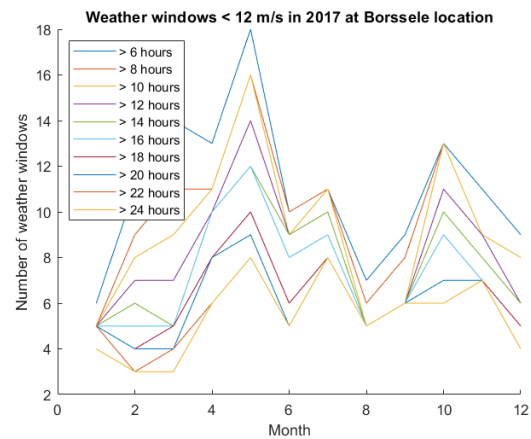**Figure 5.60:** Wind rose at MMIJ location at 150m

Another factor that affects the energy yield of a wind turbine or wind farm is the availability. In order to increase the availability, maintenance should be carefully planned. This is why it is useful to perform an analysis on the weather windows for maintenance and installation of wind turbines across the North Sea. Figure 5.61 and figure 5.62 show the number of weather windows per month at the Borssele location for wind speeds below $7\frac{m}{s}$ and $12\frac{m}{s}$, respectively. The same data is shown for the HKZ location in figure 5.63 and figure 5.64 and for the MMIJ location in 5.65 and figure 5.66. These figures show that for maintenance requiring wind speeds lower than $7\frac{m}{s}$, the month with the largest number of weather windows is August. For maintenance requiring wind speeds below $12\frac{m}{s}$ however, the best month is May. The reason why the wind speeds of $7\frac{m}{s}$ and $12\frac{m}{s}$ are chosen for this analysis is because $7\frac{m}{s}$ is the limit value for the inspection of the tower and blades and $12\frac{m}{s}$ is the limit value for climbing the rotor [54]. Note that there are slight differences in these limit values to be found throughout literature. It seems counter-intuitive that the number of weather windows below $12\frac{m}{s}$ is lower than the number of weather windows below $7\frac{m}{s}$, since a wind speed below $7\frac{m}{s}$ is automatically below $12\frac{m}{s}$. However, the number of weather windows does not say much about the length of this window. This means that when the wind speed is below $7\frac{m}{s}$ for 6 hours, the 7th hour the mean wind speed is $8\frac{m}{s}$ and the next 6 hours the mean wind speed is below $7\frac{m}{s}$ again, there will be 2 windows below $7\frac{m}{s}$ counted in this 13 hour period, while there will be only 1 window below $12\frac{m}{s}$, hence the lower number of windows below $12\frac{m}{s}$.

This is supported by the histograms shown in figure 5.67 and figure 5.68. These histograms show the number of weather window occurrences for each length below $7\frac{m}{s}$ and $12\frac{m}{s}$, respectively. It is clear that the histogram of $7\frac{m}{s}$ shows a significantly larger amount of windows with lower lengths, while the $12\frac{m}{s}$ window indicates more weather windows above 60 hours than the $7\frac{m}{s}$ histogram. This is why the figures should be interpreted carefully. Simply because the number of weather windows is larger in May does not mean the numbers of hours below the limit wind speed is larger. On the other hand, a larger number of wind speed below the limit wind speed is not beneficial if the windows are very short, since this does not provide a sufficient amount of time for the maintenance personnel to perform their tasks. Figure 5.69 and figure 5.70 show the number of hours per month below $7\frac{m}{s}$ and $12\frac{m}{s}$, respectively at the Borssele location. Figures 5.71 and figure 5.72 show the same for the HKZ location while figure 5.73 and figure 5.74 apply to the MMIJ location. Here, August is the best month for maintenance below $7\frac{m}{s}$ while the figures for $12\frac{m}{s}$ differ from the weather window analyses. Especially September contains a larger number of useful hours than the weather window analysis showed. This is why the weather window graph should be interpreted in combination with the number of hours below the limit value when making a maintenance plan.
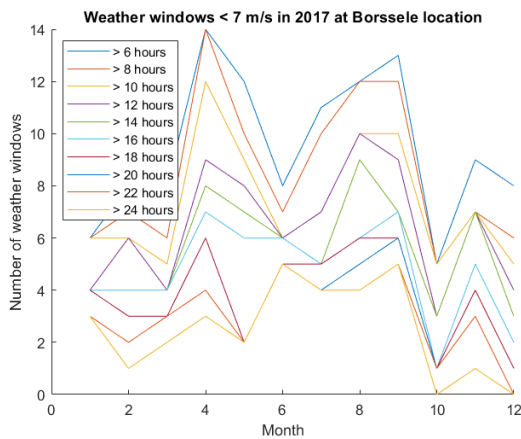
Figure 5.61:
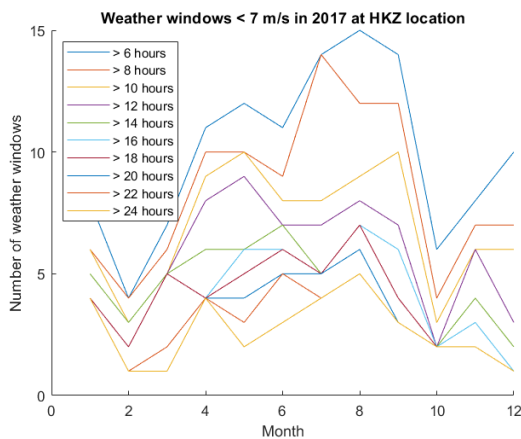Weather windows <7m/s at Borssele location at 150m

Figure 5.62:
Weather windows <12m/s at Borssele location at 150m

Figure 5.63:
Weather windows <7m/s at HKZ location at 150m
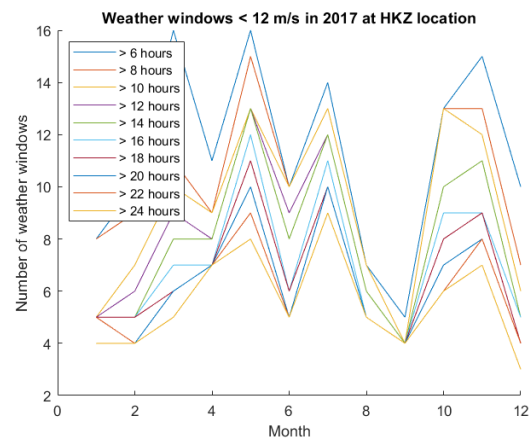
Figure 5.64:
Weather windows <12m/s at HKZ location at 150m
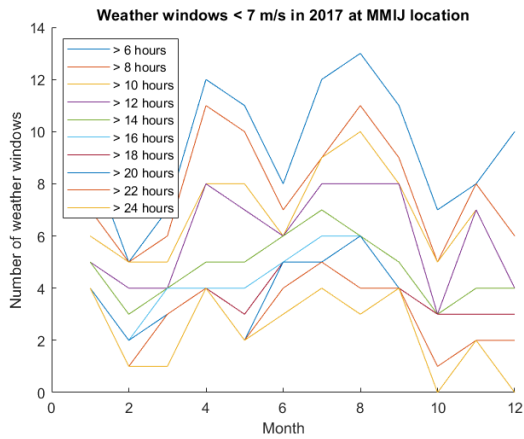
Figure 5.65:
Weather windows <7m/s at MMIJ location at 150m
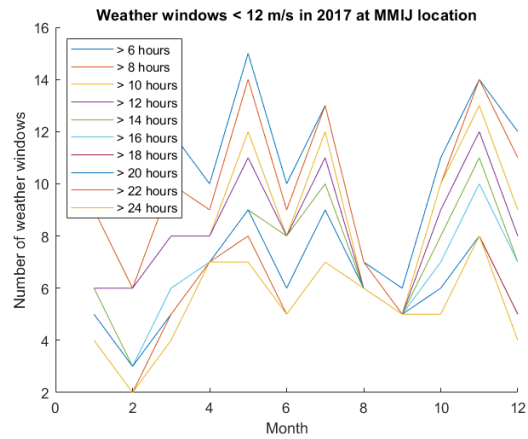
Figure 5.66:
Weather windows <12m/s at MMIJ location at 150m
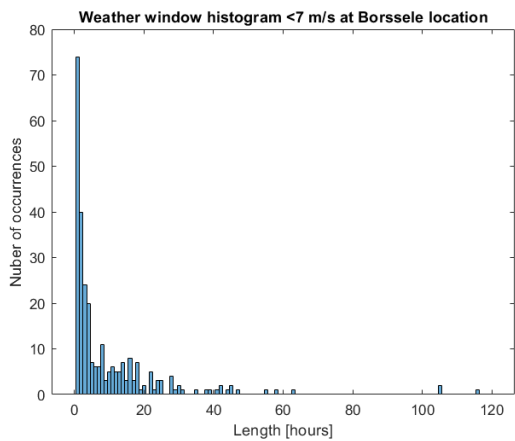
Figure 5.67: Weather
window histogram <7m/s at Borssele location at 150m
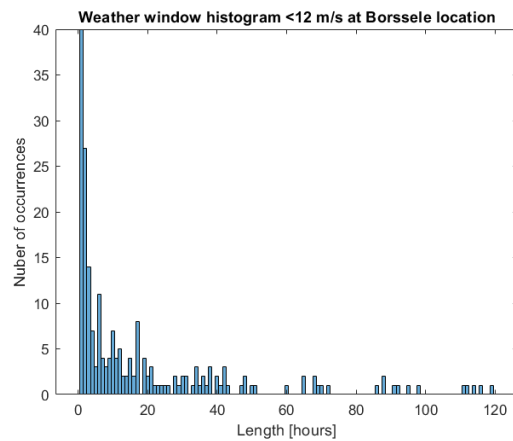
Figure 5.68: Weather
window histogram <12m/s at Borssele location at 150m
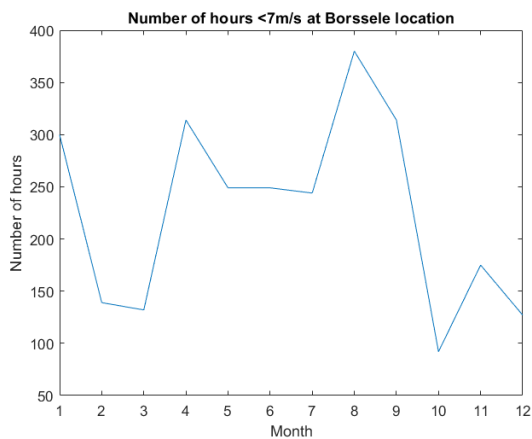
Figure 5.69:
Number of hours <7m/s at Borssele location at 150m
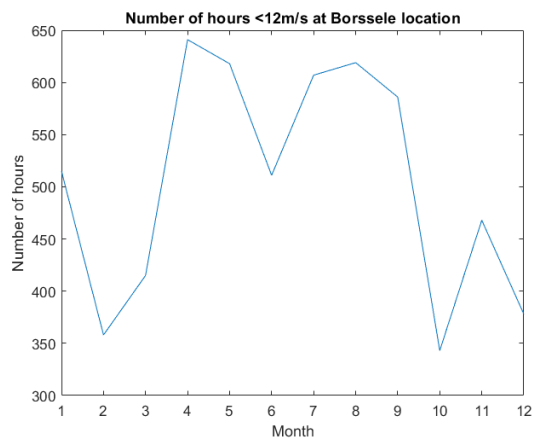
Figure 5.70:
Number of hours <12m/s at Borssele location at 150m
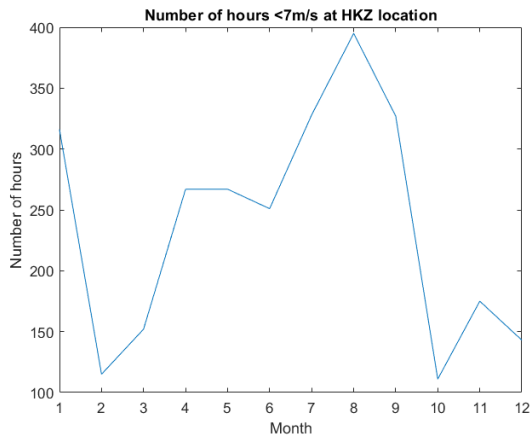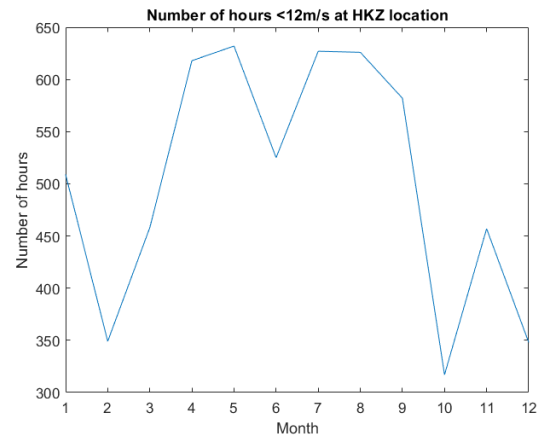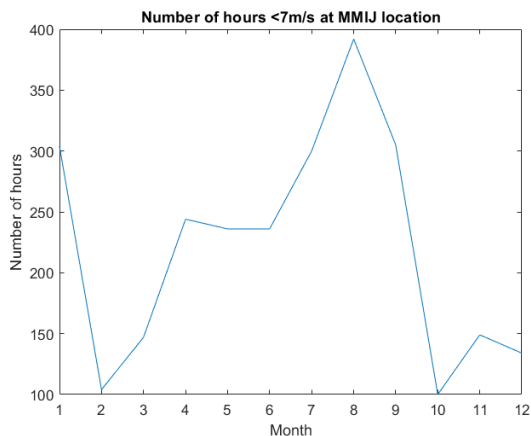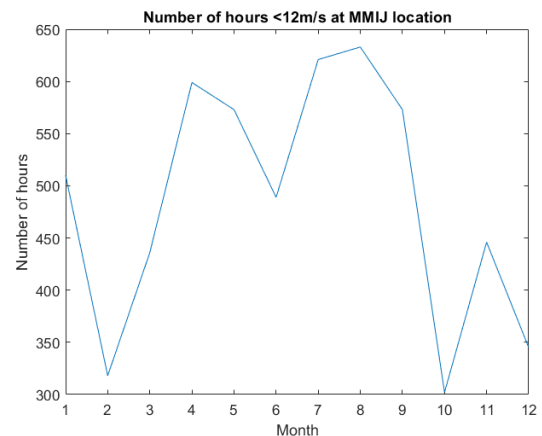
Figure 5.71:
Number of hours <7m/s at HKZ location at 150m

Figure 5.72:
Number of hours <12m/s at HKZ location at 150m

Figure 5.73:
Number of hours <7m/s at MMIJ location at 150m

Figure 5.74:
Number of hours <12m/s at MMIJ location at 150m

5.3. Fatigue

In this section, the fatigue results will be shown that were obtained using the method described in section 4.3. The results shown here apply to blade 1 of the reference turbines, where it is assumed that all three blades experience the same fatigue damage over their lifetime. The blade motions assessed in this section are the edgewise and flap-wise motions. In appendix C, some additional information can be found regarding the fatigue analysis. First, since the FASTTool is lacking a user guide or README file, a short user guide is given including a step by step procedure to change the MATLAB code in order to include the new turbulence intensity values. In this appendix, the values needed to write the input files of both reference turbines are given as well. Some of the time domain output results of FAST are plotted as well as several stress histograms that were obtained during the analysis.

Figure 5.75 shows the edgewise fatigue damage of the $5MW$ wind turbine blade with a turbulence intensity of 6% when the first rainflow counting algorithm is used. This is the rainflow counting function according to the ASTM standard. The first thing that can be noted from the figure is the fact that the fatigue damage is very low overall, so the blade is nowhere near fatigue failure. There are several possible explanations for this. First of all, only power production is considered in the fatigue analysis and the first wind speed of $3\frac{m}{s}$ is not used due to FAST limitations, this is a partial source of error. Secondly, the effect of mean stress is ignored when the S-N curve was used to determine the damage fractions while mean stress can have significant effects on fatigue damage. Thirdly, fatigue might not have been the driving factor in the blade design. It is possible that the extreme loads for which the blade was designed are sufficient to make the

fatigue damage negligible. The same goes for the tower of both the $5MW$ and the $15MW$ reference turbine, for which no results will be shown. The reason for this is that all cyclic loading occurs below the fatigue limit, leading to a fatigue damage of zero for the steel tower. Furthermore, showing fatigue results for the tower would not be representative since this is an offshore structure, meaning the tower will experience loading caused by tides and currents as well as wind loads. Only simulating the wind loads on the tower to assess its fatigue would be inadequate.

However, the most likely explanation for the seemingly low blade fatigue damage can be found by comparing the results to the results obtained in the Sandia 100-meter all-glass blade analysis [55]. This report describes the blade that was used as the baseline for the blades of the reference turbines used in this report. This means that the composite materials used in the blades including its fatigue properties are similar. In the Sandia report referenced above, albeit using different input wind conditions with larger turbulence intensities and a different wind turbine, it was found that at the blade root, the edgewise fatigue damage was in the order of $1E-7$ and the flap-wise fatigue damage was in the order of $1E-10$. It was also found that at the spanwise location of the blade adjacent to the root, the fatigue damage was largest in the order of $1E-2$ for the edgewise motion. This means that the root is not the most fatigue sensitive location on the blade. For the analysis in this report that is focused on a comparison between different locations, inflow conditions and temporal resolution of the input data, this should not be a problem. When designing a wind turbine however, it is very important to analyse the most fatigue sensitive location on the blade.

Figure 5.75 can be compared to figure 5.76 in order to see the effect of turbulence intensity on the fatigue damage. For the $5MW$ wind turbine, increasing the turbulence intensity from 6% to 12% leads to an increase in fatigue damage by a factor of around 1.25. This shows that turbulence is a significant source of fatigue damage for horizontal axis wind turbines. The comparison between two rainflow counting algorithms can also be made here. Looking at figure 5.75 and figure 5.77, the fatigue damage results are as expected. The rainflow counting algorithm that does not make use of half load cycles predicts a larger fatigue damage, but the effects are limited.
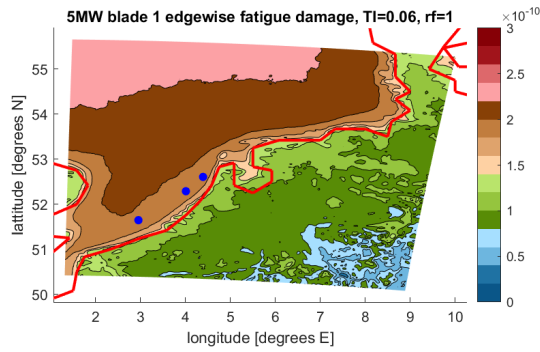
Figure 5.75: Fatigue damage of $5MW$ turbine and 6% turbulence intensity
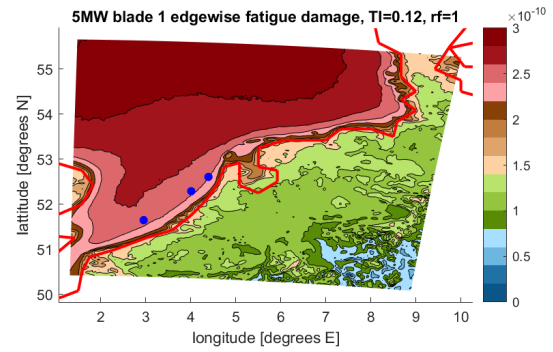
Figure 5.76: Fatigue damage of $5MW$ turbine and 12% turbulence intensity
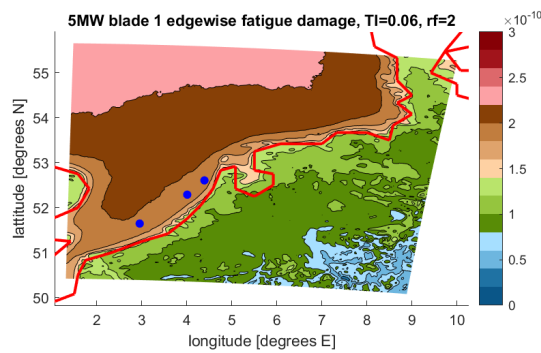
Figure 5.77: Fatigue damage of $5MW$ turbine with simple rainflow function
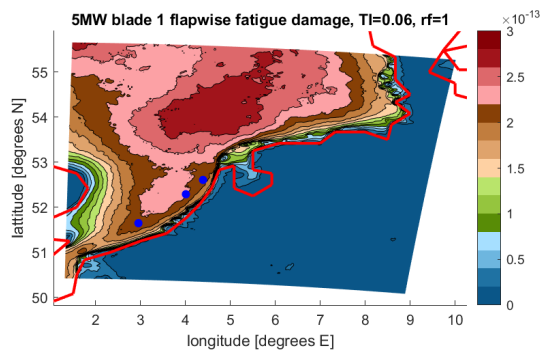
Figure 5.78: Fatigue damage of $5MW$ turbine and 6% TI **Figure 5.79:** Fatigue damage of $5MW$ turbine and 12% TI
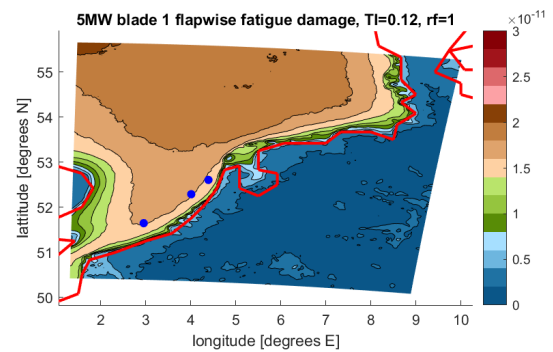
Figure 5.78 and figure 5.79 show the flap-wise fatigue damage of the $5MW$ wind turbine blades for a turbulence intensity of 6% and 12%, respectively. Comparing between both turbulence intensities, it can be seen that the flap-wise fatigue damage is even more sensitive to turbulence intensity than the edgewise motion. This is to be expected since the flap-wise motion is mostly influenced by the lift force over the airfoil, which is in turn mostly affected by the wind speed and the variations thereof. On the other hand, the edge-wise fatigue damage is partially influenced by the lift force over the airfoil, but it also contains a blade mass

component that changes over the rotation of the rotor causing fatigue damage. This is why the edgewise fatigue damage is larger compared to the flap-wise fatigue damage. This explanation is supported by the fact that the flap-wise fatigue damage is uniformly low onshore where the wind speeds and thus variations in wind speed are much lower than offshore, while the edgewise fatigue decreases more gradually toward far onshore locations.

Figure 5.80 and figure 5.81 show the fatigue damage for the $15MW$ wind turbine blade for edgewise and flap-wise motion, respectively. When comparing both figures to their $5MW$ versions, it can be seen that the fatigue damage of the $15MW$ turbine is half of that of the $5MW$ turbine. This is not due to smaller load cycles but because of the larger moment of inertia of the $15MW$ wind turbine blades. Again, the edgewise fatigue damage is larger than the flap-wise fatigue damage. Several fatigue contour plots were not shown in this section due to redundancy, they can be found in appendix C.
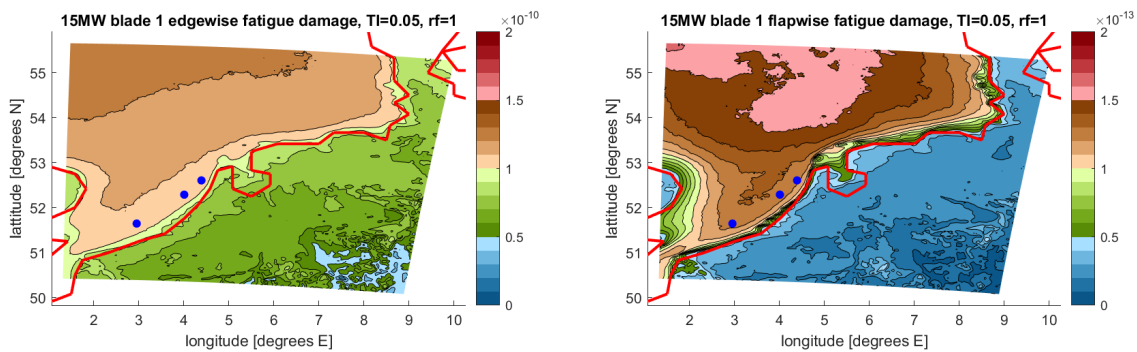
Figure 5.80: Edgewise fatigue damage of $15MW$ turbine **Figure 5.81:** Flap-wise fatigue damage of $15MW$ turbine

Another important aspect to consider is the effect of using hourly wind speed values compared to 10-minute values. The fatigue damage is calculated using 10-minute values for three offshore wind farm locations, marked by blue dots on the figures shown above. These offshore wind farms are from southwest to northeast: Borssele, Hollandse Kust Zuid (HKZ) and Hollandse Kust Noord (HKN). The results of the analysis are summarised in table 5.2, table 5.3 and table 5.4. The rows correspond to the locations and the columns describe the simulation case. The values represent the ratio of fatigue damage using hourly wind speed values to the fatigue damage using 10-minute wind speed values, where a value below 1 indicates that the fatigue damage using 10-minute values is larger than the fatigue damage using hourly values. The tables give these values for the $5MW$ edgewise case, $5MW$ flap-wise case and $15MW$ case, respectively.

Some interesting remarks can be made based on these tables. First of all, the fatigue damage obtained using hourly values is in almost all cases lower than the fatigue damage obtained using 10-minute values. The only case for which this is not true, is the edgewise motion of the blade at the Borssele wind farm site. The most significant differences can be found for the flap-wise fatigue damage. This is expected since the main difference between the hourly and 10-minute approach is the Weibull function used for the wind speeds and the stress cycles caused by turbulence increase with increasing wind speed. For both reference turbines, the HKN wind farm location shows the largest differences, being as high as 17% for the $5MW$ turbine flap-wise motion at a turbulence intensity of 6%. The smallest differences are found at the Borssele find farm location, where the ratio of hourly to 10-minute fatigue damage fluctuates around 1.

Table 5.2: Comparison of $5MW$ edgewise fatigue damage calculated with 10-minute and hourly wind speed values for three locations, where the values are $\frac{hourly}{10-minute}$

Location	TI=0.06 Rainflow 1	TI=0.12 Rainflow 1	TI=0.06 Rainflow 2	TI=0.12 Rainflow 2
Borssele	1.0405	1.0413	1.0405	1.0413
HKZ	0.9976	0.9963	0.9976	0.9963
HKN	0.9560	0.9528	0.9560	0.9527

Table 5.3: Comparison of $5MW$ flap-wise fatigue damage
calculated with 10-minute and hourly wind speed values for three locations, where the values are $\frac{hourly}{10-minute}$

Location	TI=0.06 Rainflow 1	TI=0.12 Rainflow 1	TI=0.06 Rainflow 2	TI=0.12 Rainflow 2
Borssele	0.9678	1.0135	0.9697	1.0159
HKZ	0.8985	0.9449	0.9002	0.9474
HKN	0.8269	0.8773	0.8287	0.8802

Table 5.4: Comparison of $15MW$ fatigue damage
calculated with 10-minute and hourly wind speed values for three locations, where the values are $\frac{hourly}{10-minute}$

Location	Edgewise Rainflow 1	Edgewise Rainflow 2	Flap-wise Rainflow 1	Flap-wise Rainflow 2
Borssele	1.0215	1.0215	0.9468	0.9525
HKZ	0.9864	0.9864	0.9079	0.9132
HKN	0.9525	0.9525	0.8463	0.8531

In the results presented above, the assumption is made that all wind speed profiles follow the power law profile that FAST uses as input. In reality, this is not the case and other wind profiles like low level jets will be encountered. Including low level jets in the fatigue analysis is very difficult since there are many different aspects to consider. In his doctoral thesis, Maarten Holtslag describes in detail how the LLJ height with respect to hub height, the positive and negative shear present in the low level jet and the magnitude of the maximum wind speed can affect the loads on the wind turbine blades [56]. It is also described how the mechanisms behind low level jets are different for onshore and offshore locations. It was decided not to perform FAST simulations on the effect of low level jets on the reference turbines, even though it is implemented in the TurbSim module. The reason for omitting this analysis is based on a trade-off between the available time for the project and the added value of the analysis. Because the low level jet implementation in FAST is based on the Lamar Low Level Jet project using measurements up to $120m$ for an onshore location in Colorado, there is no guarantee that its results will be accurate for far offshore wind turbines in the North Sea with low level jets up to $300m$ [42][57]. Additionally, even with the FAST model it would be difficult to capture all different low level jet parameters that affect the loading as described by Holtslag.

The exact influence of low level jets on wind turbine loading and fatigue is still unclear as different publications reach different conclusions. The DOWA project did not find any significant impact of low level jets on wind turbine loading compared to a reference case [11]. In fact, the loading was reduced due to the fact that turbulence intensity values are lower in the stable conditions of a low level jet. Note that this reduced loading does not necessarily mean the fluctuations in the loading are reduced, which is relevant for fatigue calculations. Holtslag established a clear increase in flap-wise blade root stresses in the presence of low level jets, while Rodriguez describes increases in mean flap-wise bending moments as large as 57% compared to an unstable case [58]. He also describes a significant increase in standard deviation of the flap-wise bending moment, which is confirmed by research of Cosack et al., reporting an increase in standard deviation of up to 20% for a $5MW$ reference turbine [59].

For this reason, as an alternative to the implementation of low level jets in the fatigue analysis, it was decided to perform a sensitivity analysis to see what the effect of a change in flap-wise blade root bending moment is to the total lifetime fatigue damage. Table 5.5 shows this sensitivity analysis for the $5MW$ wind turbine while table 5.6 shows the results for the $15MW$ reference turbine. The analysis is performed for three wind farm locations and the top row represents the total lifetime fatigue damage without a change in bending moment. In these tables, it can be seen that a small increase in the standard deviation of the bending moment already has significant impact on the fatigue damage, where a $5-20\%$ increase in bending moment standard deviation yields a relatively constant increase in fatigue damage of $21-26\%$ for the $5MW$ turbine. When the bending moment standard deviation is increased further, the fatigue damage increases significantly. When comparing the $5MW$ turbine results to the $15MW$ results, it is concluded that the fatigue damage of the larger wind turbine is significantly more sensitive to a change in bending moment standard deviation, even though at standard deviation increases of $5-10\%$, the effect on fatigue damage is relatively limited compared to the $5MW$ turbine. The conclusion that larger turbines are more sensitive to a change in bending moment standard deviation is supported by the conclusion drawn by Cosack et al., stating that the influence of low level jets increases with turbine size[59].

Table 5.5: Sensitivity analysis of $5MW$ reference turbine blade root
lifetime fatigue damage for change in flap-wise bending moment standard deviation at three wind farm locations

M_{root_std}	**Borssele**	**HKZ**	**HKN**
+0%	2.2452e-13	2.4320e-13	2.5654e-13
+5%	2.7344e-13 (+22%)	2.9475e-13 (+21%)	3.1136e-13 (+22%)
+10%	2.7545e-13 (+23%)	2.9555e-13 (+22%)	3.1222e-13 (+22%)
+20%	2.8296e-13 (+26%)	2.9855e-13 (+23%)	3.1543e-13 (+23%)
+50%	3.9042e-13 (+74%)	3.4150e-13 (+40%)	3.6140e-13 (+41%)

Table 5.6: Sensitivity analysis of $15MW$ reference turbine blade root
lifetime fatigue damage for change in flap-wise bending moment standard deviation at three wind farm locations

M_{root_std}	**Borssele**	**HKZ**	**HKN**
+0%	1.3107e-13	1.3872e-13	1.4554e-13
+5%	1.5438e-13 (+18%)	1.6195e-13 (+17%)	1.6985e-13 (+17%)
+10%	1.5875e-13 (+21%)	1.6453e-13 (+19%)	1.7220e-13 (+18%)
+20%	1.7504e-13 (+34%)	1.7418e-13 (+26%)	1.8098e-13 (+24%)
+50%	4.0812e-13 (+211%)	3.1219e-13 (+125%)	3.0649e-13 (+111%)

6

Validation

In order to be able to draw conclusions based upon the results presented in chapter 5, they will be validated. In this chapter, the validation procedure and results will be discussed. Validation related to atmospheric stability can be found in section 6.1. Validation of energy yield and fatigue results will be performed in section 6.2 using buoy mounted LiDAR measurements.

6.1. Stability

The method used to perform stability calculations was already discussed in chapter 4 when using the DOWA data. For the validation of these results, MMIJ measurement data is used. The methods to calculate the shear exponent, Obukhov length, temperature profile and turbulence intensity are largely identical. However, when processing the measurement data, several instances were discarded due to the unavailability of one of the parameters. This means that the measurement results will show a larger amount of discarded values than the DOWA or LES simulation results. Furthermore, since only two measurement heights are available, low level jets cannot be identified and are omitted from this analysis. Note that in literature, several publications can be found regarding low level jets at the MMIJ location, a comparison with these results was already made in chapter 5.

Figure 6.1 and figure 6.2 show the stability histograms using the shear exponent as calculated by measurement data and DOWA data, respectively. As mentioned earlier, a larger number of values is discarded in the measurement results. The trends are similar in both histograms but the measurements show more stable and neutral conditions than the DOWA simulations.
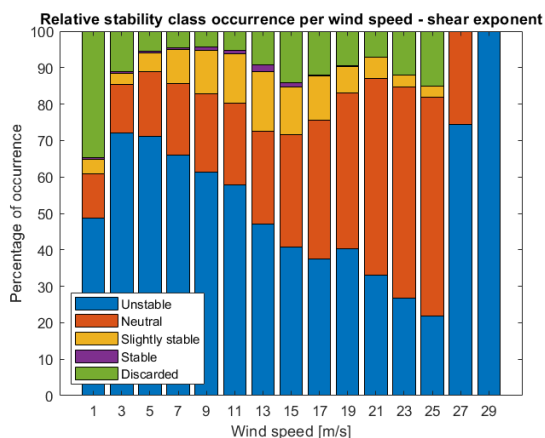

Figure 6.1: Shear exponent stability histogram for MMIJ measurements between $27m$ and $90m$
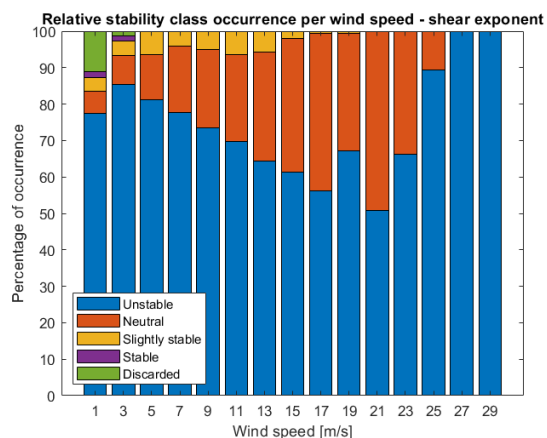
Figure 6.2: Shear exponent stability histogram for DOWA simulations at MMIJ location between $30m$ and $90m$

Figure 6.3 and figure 6.4 show the stability histograms using the Obukhov length as calculated by measurement data and DOWA data, respectively. Again, the measurements show a slightly larger number of discarded values. The number of stable values is also larger in the measurements, but the trends are similar. The similarities between the results obtained with measurements and DOWA data seem to confirm that the DOWA data does not contain large errors. The reason why the stability results differ from results found in literature should then be attributed to the methods and parameters used for the stability calculations.
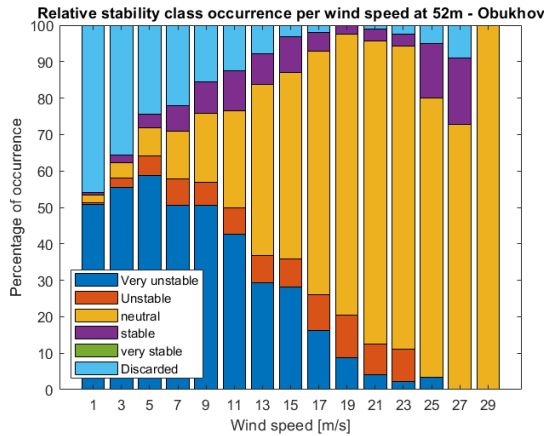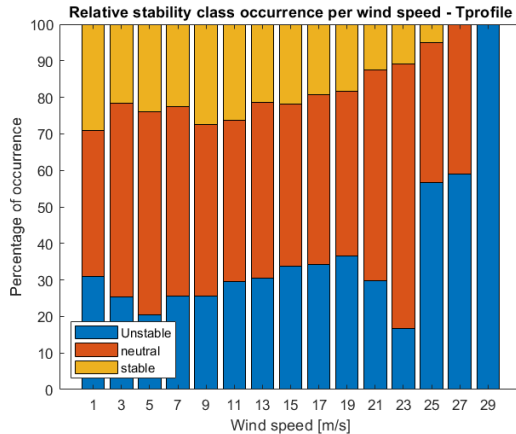

Figure 6.3: Obukhov length stability histogram for MMIJ measurements between $27m$ and $90m$
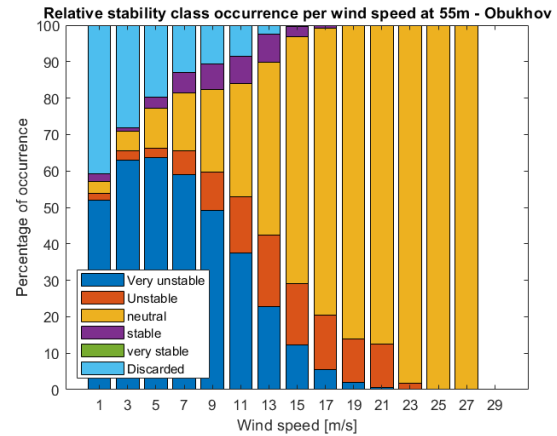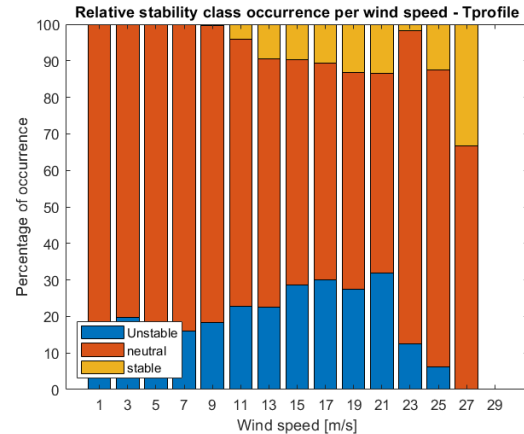

Figure 6.4: Obukhov length stability histogram for MMIJ DOWA simulations between $30m$ and $90m$

Figure 6.5 and figure 6.6 show the stability histograms using the temperature profile as calculated by measurement data and DOWA data, respectively. Once again, the measurements show a larger number of stable values. Note that the discarded values are not shown in figure 6.5 and that the DOWA approach does not discard any values when calculating the temperature profile stability results.

Figure 6.5: Temperature profile stability histogram for MMIJ measurements between $27m$ and $90m$

Figure 6.6: Temperature profile stability histogram for MMIJ DOWA simulations between $30m$ and $90m$

Figure 6.7, figure 6.8 and figure 6.9 show the turbulence intensity versus wind speed graph at different heights for the MMIJ, Borssele and HKZ locations, respectively. The graphs also show the standard deviation of the data at every wind speed. The turbulence intensity results differ significantly from the results found in chapter 5, since turbulence intensities of 6% and 5% were found for heights of $90m$ and $150m$ respectively for all locations. From the measurement data it appears that the turbulence intensity is around 12% for the Borssele and HKZ locations which are located at approximately the same distance from the coastline, while for the further offshore location of MMIJ, the turbulence intensity is significantly lower. In the monthly data reports published during the HKZ measurement campaign, turbulence intensities of $5-15\%$ were found when looking at the turbulence intensity versus time graph in the report [39]. The same range of values was found for the Borssele measurement campaign [37]. The turbulence intensity

values for HKZ and Borssele are significantly higher than one would expect from an offshore location in the North Sea. In the measurement validation reports, these high turbulence intensity values are explained by the fact that $TI = \frac{\sigma_u}{\bar{U}}$ and for low mean wind speeds, this definition can yield large turbulence intensity values. This explanation does not seem satisfactory because the large TI values are also observed for larger wind speeds. One would expect values in the range of $5-10\%$ like the MMIJ measurements, which are confirmed by an ECN report analysing turbulence intensity at MMIJ [60]. In the study described in that report, both the MMIJ mast and a ground based LiDAR are used. After comparison of the results, it was concluded that the turbulence intensity values are 50% higher for LiDAR measurements than for meteorological mast measurements, but only for lower wind speeds. This means the larger TI values for Borssele and HKZ can partially be explained by the fact that LiDAR measurements were used. Additional error can be expected there since these measurements are obtained with floating LiDAR systems, while the MMIJ study uses a ground based LiDAR. In order to exclude the location as a possible explanation for deviating TI values, the turbulence intensity is plotted for EPL and LEG in figure 6.10 and figure 6.11, respectively. The Europlatform results use measurements for the period of 01/07/2016-31/12/2016 while the Lichteiland Goeree results use measurements for the full year of 2017. Both figures show TI values in the same range as figure 6.7, supporting the hypothesis that the results for Borssele and HKZ are not accurate.
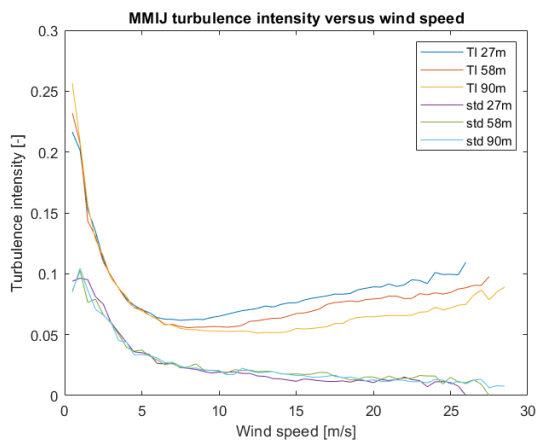

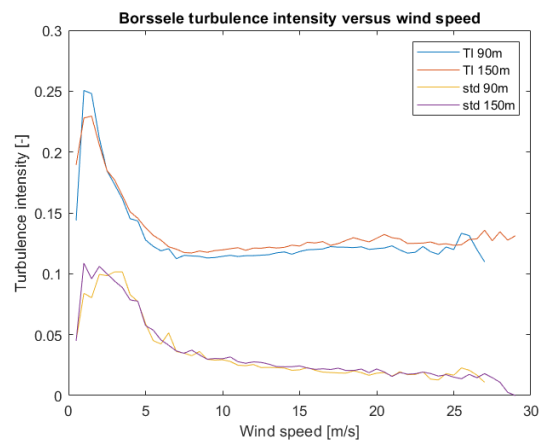**Figure 6.7:** Turbulence intensity at MMIJ
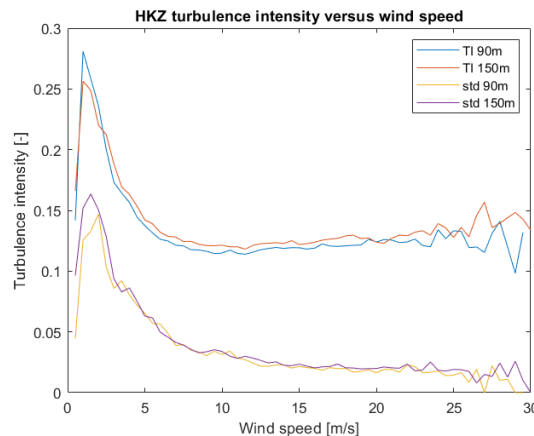

Figure 6.8: Turbulence intensity at Borssele

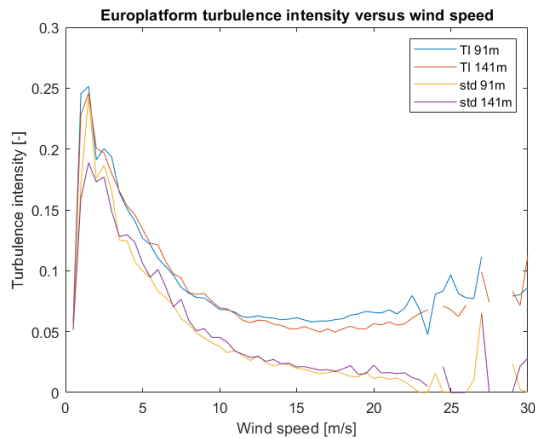
Figure 6.9: Turbulence intensity at HKZ

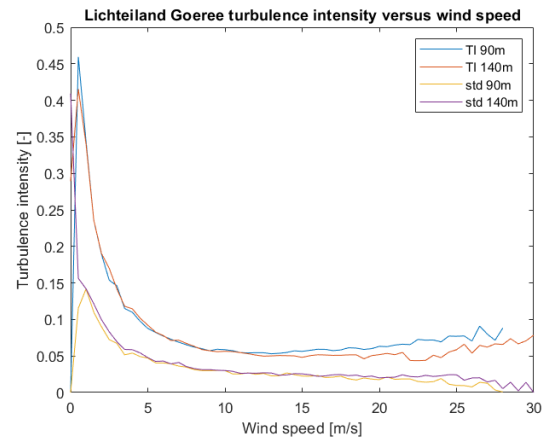**Figure 6.10:** Turbulence intensity at EPL

Figure 6.11: Turbulence intensity at LEG

6.2. Energy yield and fatigue

The validation of energy yield and fatigue results will be performed for the Borssele and HKZ wind farm sites because for these locations LiDAR measurements are available, allowing for a representative computation of the equivalent wind speed. Subsection 6.2.1 will discuss the validation of the energy yield results and subsection 6.2.2 will present the validation of the fatigue results.

6.2.1. Energy yield

The validation results regarding the energy yield analyses of the $5MW$ reference turbine are shown in table 6.1. The Borssele wind farm location shows the largest differences between measurement results and simulations results. For this location, the DOWA hourly data predicts an energy yield which is around 2% lower than the measurement results, while the LES 10-minute simulations predict an 8% lower energy yield. For the HKZ wind farm site, the DOWA hourly results accurately predict the measurement energy yield, while the LES 10-minute values underpredict the energy yield by 3%. This underprediction can have very large consequences on the cost of energy as was already explained in chapter 5.

**Table 6.1:** Validation of 5MW turbine energy yield results

Location	Parameter	Site measure- ments	DOWA 1 hour values	LES 10 minute values	DOWA/ measure- ments	LES/ measure- ments
Borssele	a [-]	10.7	10.5	10.1	0.98	0.95
	k [-]	2.1	2.1	2.0	1.01	0.93
	Energy yield [GWh]	23.7	23.1	21.8	0.98	092
HKZ	a [-]	9.8	9.8	9.7	1.00	0.99
	k [-]	2.2	2.2	2.1	0.98	0.96
	Energy yield [GWh]	21.3	21.3	20.7	1.00	0.97

The same trends can be seen for the $15MW$ turbine in table 6.2. However, for this turbine both the DOWA hourly simulations and the 10-minute LES data accurately predict the energy yield for the HKZ wind farm location. Note that the DOWA and LES results shown in table 6.1 and table 6.2 are for the same time period as the recorded measurements. This is why the values in the tables do not correspond to the values found in table 5.1. Because the same time period was used as the measurements, the energy yield values presented here are not necessarily annual energy yield values and serve merely for validation purposes. For a comparison of the annual energy yield between certain locations in the North Sea, more accurate results are shown in chapter 5.

Table 6.2: Validation of 15MW turbine energy yield results

Location	Parameter	Site measure-ments	DOWA 1 hour values	LES 10 minute values	DOWA/ measure-ments	LES/ measure-ments
Borssele	a [-]	11.0	10.8	10.6	0.98	0.96
	k [-]	2.0	2.0	1.9	1.02	0.97
	Energy yield [GWh]	79.1	77.7	75.0	0.98	0.95
HKZ	a [-]	10.1	10.1	10.1	1.00	1.00
	k [-]	2.1	2.1	2.0	1.00	0.97
	Energy yield [GWh]	72.6	72.6	72.3	1.00	1.00

The wind rose at the Borssele wind farm location is shown in figure 6.12 and figure 6.13 using site measurements and DOWA data, respectively. Figure 6.14 and figure 6.15 show the same parameter for the HKZ location. The wind roses using site measurements and DOWA data are largely identical, with only minor differences. The differences are larger for the Borssele location, where the dominant wind direction is 10 degrees larger in the DOWA wind rose. Wind roses for a height of $90m$ can be found in appendix B.
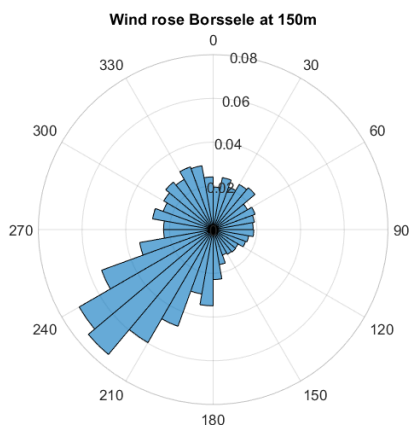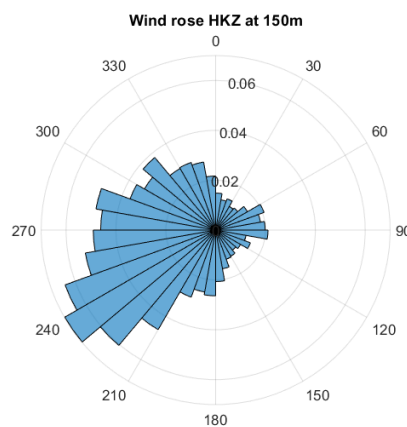

Figure 6.12: Wind rose at Borssele wind farm location at 150m using site measurements
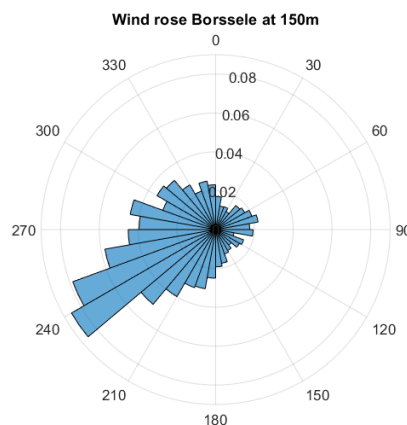
Figure 6.13: Wind rose at Borssele wind farm location at 150m using DOWA data
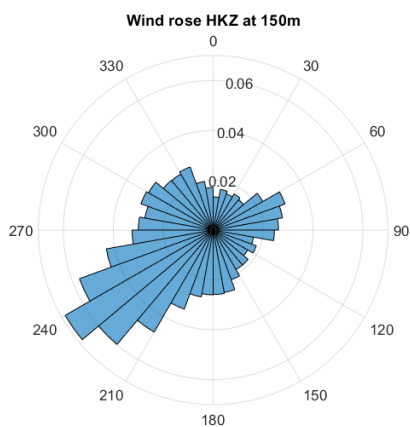
Figure 6.14: Wind rose at HKZ wind farm location at 150m using site measurements

Figure 6.15: Wind rose at HKZ wind farm location at 150m using DOWA data

6.2.2. Fatigue

The validation of the fatigue results is shown in table 6.3. Note that for the DOWA hourly results, the turbulence intensity is used that was found by the site measurements. This is done because when using the turbulence intensity results found by the LES runs, the results would be too different and the purpose of the validation procedure would be lost. It should be kept in mind that the turbulence intensity values found by the measurements are assumed to be too high, but in order to be able to validate the DOWA data it is important to compare fatigue results with the same turbulence intensity value of 12%. For the results of the 10-minute LES values however, the turbulence intensity value of 6% is used that was found in chapter 5. From the table, it is clear that the flap-wise fatigue damage is most sensitive to turbulence intensity, which was already concluded previously. The Borssele location again shows larger differences between simulation and measurement data than the HKZ location. The 10-minute LES results are very inaccurate because of the turbulence intensity values used when performing the simulations. The DOWA hourly simulations still underpredict the flap-wise fatigue damage at Borssele by 11%, which is significant even though the same turbulence intensity is used, meaning the difference is caused entirely by the difference in Weibull distribution. For the HKZ location, the flap-wise fatigue damage is overestimated by 4%. Fatigue validation is not performed for the $15MW$ reference turbine because for a turbulence intensity of 12%, FAST encountered an error leading to a negative rotor speed. This error can have multiple causes such as numerical instabilities of the AeroDyn submodule or the chosen pitch or torque control strategy. Fixing this error would require changes that increase the uncertainty of the results, making it hard to use them for the validation procedure.

Table 6.3: Validation of 5MW turbine energy fatigue results

Location	Parameter	Site measurements	DOWA 1 hour values	LES 10 minute values	DOWA/ measurements	LES/ measurements
Borssele	Edgewise fatigue damage	2.5354e-10	2.4564e-10	1.7985e-10	0.97	0.71
	Flap-wise fatigue damage	1.9075e-11	1.7036e-11	2.6675e-13	0.89	0.01
HKZ	Edgewise fatigue damage	2.1292e-10	2.1227e-10	1.6448e-10	1.00	0.77
	Flap-wise fatigue damage	1.0453e-11	1.0914e-11	1.2485e-13	1.04	0.01

7

Conclusions and recommendations

This chapter presents an overview of the main conclusions to be drawn from the results shown throughout the report and some recommendations will be made to improve the analyses in future work. The conclusions will be presented in section 7.1 and some recommendations for future work can be found in section 7.2.

7.1. Conclusions

The aim of this project was to define and quantify the applications and limitations of the DOWA for wind energy purposes by using it to calculate the energy yield and fatigue damage of two reference wind turbines at multiple locations in the North Sea, with special attention for atmospheric stability.

The calculations have been performed using hourly DOWA data. For the locations of Borssele, HKN and HKZ, data was also available of LES runs with a temporal resolution of 10 minutes. The main conclusions to be drawn on the atmospheric stability analysis is the fact that the results obtained in this report can differ significantly with the results found in literature. When validating the DOWA results against site measurements however, similar results are found. This means that the discrepancies between the results in this report and results in literature can be at least partially attributed to the method used to obtain the shear exponent, Obukhov length and temperature profile and the parameters used to divide them into stability classes. The turbulence intensity parameter is not part of the DOWA and cannot be calculated based upon its data. Therefore, LES data or site measurements have to be used to calculate the turbulence intensity for certain locations and extrapolated over the full DOWA domain. It was shown that the DOWA can be used to identify deviating wind profiles, like low level jets.

With respect to energy yield calculations, the DOWA data allows for a straightforward calculation of the annual energy yield of a wind turbine. This includes air density, wind shear and turbulence intensity corrections although the latter could not be performed based on DOWA data only as explained in the previous paragraph. The energy yield results obtained with this analysis allow for an accurate comparison of the energy yield of a single wind turbine across the North Sea, where further offshore locations correspond to a larger annual energy yield due to larger wind speeds as expected. A major component of the energy yield calculations is the Weibull fit. It was found that one should be careful when using DOWA data to obtain this Weibull fit, since a low number of wind speed values could introduce significant error. Comparison with site measurements revealed energy yield differences up to 2% for the Borssele wind farm. Note that a 2% energy yield difference could have significant impact on the cost of energy. The fact that DOWA has a temporal resolution of 1 hour instead of the 10-minute industry standard does not impact the Weibull parameters to a large extent. Although wind farm energy yield was not explicitly included in the analysis, some calculations were performed that can provide insight in the applications of DOWA with respect to wind farm design. It was shown that the dominant wind direction can be plotted across the North Sea to allow for easy comparison between different location. The dominant wind direction is of importance for wind farm design when considering e.g. wind turbine wakes. It was also shown that the DOWA wind direc-

tion is very accurate compared to site measurements. The DOWA can also be used to determine weather windows in order to optimise the installation and maintenance plan of a wind farm.

The fatigue analysis showed that, for the reference turbines, blade root fatigue is not a design driver. This does not mean that DOWA does not have applications with respect to fatigue since other turbines, like vertical axis wind turbines, might suffer from this phenomenon to a larger extent. Due to the fact that fatigue damage is very dependent on turbulence intensity, it is not possible to rely only on DOWA data for these calculations. Assumptions have to be made regarding turbulence intensity, compromising the accuracy of the analysis. Additionally, stability could not be included due to doubts about the correctness of the atmospheric stability results. Fatigue was assessed using a constant turbulence intensity with the IEC standard power law profile. This means that fatigue damage is closely tied to the Weibull distribution of the wind speeds, which yields larger values for further offshore locations. The effect of including half load cycles compared to full load cycles in the rainflow counting algorithm proved to be marginal, while the effect of increasing turbulence intensity was shown to be substantial. The effect of using hourly values compared to 10-minute values proved to have a significant impact on fatigue damage as well, especially for the flap-wise fatigue damage at the HKN location. In an attempt to include at least partially the effect of low level jets in the fatigue analysis, a sensitivity analysis was performed. This sensitivity analysis investigates the effect of a change in flap-wise blade root bending moment standard deviation, which is closely tied to low level jets, on the fatigue damage. This analysis showed that an increase in bending moment standard deviation causes a significant increase in fatigue damage. This increase is larger for larger wind turbines. The fatigue damage was also validated against site measurements. This validation procedure concluded that DOWA data performs relatively well for the calculation of edgewise fatigue damage, but errors up to 11% were found for the flap-wise fatigue damage.

In summary, this means that the DOWA has many application for wind energy. It can be used to determine the location of a new wind farm as it allows for a comparison of energy yield between different locations across the North Sea. Another application is the preliminary design of wind turbines or wind farms, where a first estimation is made about the energy yield and the general lay-out of the farm. For more detailed design however, it is recommended to use site measurements.

7.2. Recommendations

The analyses performed in this report revealed the many applications of the DOWA, but it also showed that it has limitations. Limitations do not only relate to the DOWA data itself, but also to the methods used throughout this report. To some extent, these limitations include lack of resources such as time and computational power. Based on this, recommendations will be formulated here.

First of all, one the biggest limitations of the DOWA encountered throughout this report is the lack of turbulence intensity information. In future wind atlases, it is recommended to include at least a rough estimate for this. An attempt to include turbulence intensity was made in the DOWA project by including LES runs of three offshore wind farm sites, but the main purpose of this was to capture the added turbulence intensity of wind farms.

Secondly, the atmospheric stability analysis in this report should be reiterated in order to be able to draw better conclusions on the accuracy of the DOWA in comparison to literature. This means that the methods should be reviewed as well as the parameters used to perform the stability classifications, including the heights at which this stability is analysed. When the confidence in the atmospheric stability results is increased, stability effects can be included in the fatigue analysis as well.

Thirdly, the analyses in this project relate to the year of 2017 only. This should be expanded to the full time domain of DOWA in order to achieve better results for e.g. the Weibull fit. This would increase the confidence in the results but requires either more computational power or more time.

Fourthly, the fatigue analysis should be reiterated to include the effect of mean stress, a more accurate turbulence intensity estimation and stability including low level jets. The fatigue analysis should also be expanded to include all aspects of the wind turbine life, not only the normal operation in power production mode. The inclusion of other aspects like downtime is something that should be included in the energy yield calculations as well. In addition to that, the implications of using Miner's rule to determine the accumulated

fatigue damage should be quantified.

Fifthly, additional validation should be performed for multiple locations across the North Sea since the amount of site measurements used in this report is limited. Efforts should be made to include different types of measurement instruments and measurement heights.

Finally, the applications of the DOWA for wind farms should be researched in more detail. This research could include the design of a wind farm where the possibilities are explored to use the DOWA in combination with site measurements or other wind atlases and simulation models in order to decrease the cost associated to site measurements in a wind energy project. Additionally, the mesoscale modelling possibilities of the DOWA should be explored.

Bibliography

[1] "Offshore wind in europe: Key trends and statistics 2019," WindEurope, Tech. Rep., Feb. 2020.

[2] European Commission. (). "Boosting offshore renewable energy for a climate neutral europe," [Online]. Available: `https://ec.europa.eu/commission/presscorner/detail/en/ip_20_2096`. (accessed: 16.03.2021).

[3] B. Hand and A. Cashman, "A review on the historical development of the lift-type vertical axis wind turbine: From onshore to offshore floating application," *Sustainable Energy Technologies and Assessments*, vol. 38, 2020. DOI: `https://doi.org/10.1016/j.seta.2020.100646`.

[4] I. Wijnant, A. . Stepek, M. Savenije, and H. van den Brink, *User manual of the (knmi north sea wind) knw-atlas*, version 9, Jun. 2016.

[5] I. Wijnant, G. Marseille, A. Stoffelen, H. van den Brink, and A. Stepek, "Validation of knw atlas with scatterometer winds," Royal Netherlands Meteorological Institute, Tech. Rep., Apr. 2015.

[6] european centre for medium-range weather forecasts (ECMWF). (). "Era-interim," [Online]. Available: `https://www.ecmwf.int/en/forecasts/datasets/reanalysis-datasets/era-interim`. (accessed: 22.09.2020).

[7] D. P. De, S. M. Uppala, A. J. Simmons, P. Berrisford, P. Poli, S. K. U. Andrae, M. A. Balmaseda, G. Balsamo, P. Bauer, P. Bechtold, A. C. M. Beljaars, L. van de Bergand J Bidlot, N. Bormann, C. Delsol, R. Dragani, M. Fuentes, A. J. Geer, L. Haimberger, S. B. Healy, H. Hersbach, E. V. Holm, L. Isaksen, P. Kallberg, M. Kohler, M. Matricardi, A. P. McNally, B. M. Monge-Sanz, J.-J. Morcrette, B.-K. Park, C. Peubey, P. de Rosnay, C. Tavolato, J.-N. Thepaut, and F. Vitart, "The era-interim reanalysis: Configuration and performance of the data assimilation system," *Quarterly Journal of the Royal Meteorological Society*, vol. 137, pp. 553–597, 2011. DOI: `https://rmets.onlinelibrary.wiley.com/doi/pdfdirect/10.1002/qj.828`.

[8] E. I. F. de Bruijn and W. C. de Rooy, "Evaluation of harmonie in the knmi parameterisation testbed," *Adv. Sci. Res.*, vol. 8, pp. 167–170, 2012. DOI: `https://doi.org/10.5194/asr-8-167-2012`.

[9] R. Stull, *Meteorology for Scientists & Engineers*. University of British Columbia, 2015, ISBN: 978-0-88865-178-5.

[10] M. Z. Jacobson, *Fundamentals of Atmospheric Modeling*. Cambridge University Press, 2005, ISBN: 9780521548656.

[11] J. Wagenaar, "Dutch offshore wind atlas public final report," TNO, Tech. Rep., Jun. 2020.

[12] european centre for medium-range weather forecasts (ECMWF). (). "Era5," [Online]. Available: `https://www.ecmwf.int/en/forecasts/datasets/reanalysis-datasets/era5`. (accessed: 24.09.2020).

[13] J. B. Duncan, "Representation of north sea wind conditions in the dowa and the emd-conwx european mesoscale dataset," TNO, Tech. Rep., Jun. 2019.

[14] I. Wijnant, B. van Ulft, B. van Stratum, J. Barkmeijer, J. Onvlee, C. de Valk, S. Knoop, S. Kok, G. Marseille, H. K. Baltink, and A. Stepek, "The dutch offshore wind atlas (dowa): Description of the dataset," Royal Netherlands Meteorological Institute, Tech. Rep., 2019.

[15] S. Knoop, P. Ramakrishnan, and I. Wijnant, "Dutch offshore wind atlas validation against cabauw meteomast wind measurements," *Energies*, vol. 13, no. 24, pp. 1–21, 2020. DOI: `https://doi.org/10.3390/en13246558`.

[16] M. Dörenkämper, B. T. Olsen, B. Witha, A. N. Hahmann, N. N. Davis, J. Barcons, Y. Ezber, E. García-Bustamante, J. F. González-Rouco, J. Navarro, M. Sastre-Marugán, T. Sīle, W. Trei, M. Žagar, J. Badger, J. Gottschall, J. S. Rodrigo11, and J. Mann, "The making of the new european wind atlas, part 2: Production and evaluation," EGU, Tech. Rep., Apr. 2020.

[17] I. Karagali, A. N. Hahmann, M. Badger, C. Hasager, and J. Mann, "New european wind atlas offshore," *Journal of Physics: Conference Series*, vol. 1037, pp. 1–10, 2018. DOI: `10.1088/1742-6596/1037/5/052007`.

[18] S. Watson, *Mass consistent and linearised wind flow models*, Lecture slides, Course 'AE4W30', 2019.

[19] R. J. Barthelmie, "The effects of atmospheric stability on coastal wind climates," *Meteorological Applications*, vol. 6, pp. 39–47, 1999.

[20] S. Wharton and J. K. Lundquist, "Assessing atmospheric stability and its impacts on rotor-disk wind characteristics at an onshore wind farm," *Wind Energy*, vol. 15, pp. 525–546, 2012. DOI: `10.1002/we.483`.

[21] J. S. Touma, "Dependence of the wind profile power law on stability for various locations," *Journal of the Air Pollution Control Association*, vol. 27, no. 9, pp. 863–866, 1977. DOI: `10.1080/00022470.1977.10470503`.

[22] G. P. van den Berg, "Wind turbine power and sound in relation to atmospheric stability," *Wind Energy*, no. 11, pp. 151–169, 2008. DOI: `10.1002/we.240`.

[23] J. Rohatgi, "An analysis of the influence of atmospheric stability on vertical wind profiles - its influence on wind energy and wind turbines," *Wind Engineering*, vol. 20, no. 5, pp. 319–332, 1996.

[24] M. C. Holtslag, W. A. A. M. Bierbooms, and G. J. W. van Bussel, "Estimating atmospheric stability from observations and correcting wind shear models accordingly," *Journal of Physics*, vol. 555, pp. 1–10, 2014. DOI: `10.1088/1742-6596/555/1/012052`.

[25] B. Lange, S. Larsen, J. Højstrup, and R. Barthelmie, "Importance of thermal effects and sea surface roughness for offshore wind resource assessment," *Journal of Wind Engineering*, vol. 92, no. 11, pp. 959–988, 2004. DOI: `10.1016/j.jweia.2004.05.005`.

[26] American Meteorological Society. (). "Glossary of meteorology," [Online]. Available: `https://glossary.ametsoc.org/wiki/Welcome`. (accessed: 20.01.2021).

[27] P. Baas, F. C. Bosveld, H. K. Baltink, and A. A. M. Holtslag, "A climatology of nocturnal low-level jets at cabauw," *Journal of Applied Meteorology and Climatology*, vol. 48, no. 8, pp. 1627–1642, 2009. DOI: `10.1175/2009JAMC1965.1`.

[28] P. Eecen and J. Wagenaar, Eds., *Dependence of Power Performance on Atmospheric Conditions and Possible Corrections*, (Brussels, Belgium), ECN, Mar. 2011.

[29] R. Wagner, I. Antoniou, S. M. Pedersen, M. S. Courtney, and H. E. Jørgensen, "The influence of the wind speed profile on wind turbine performance measurements," *Wind Energy*, vol. 12, no. 4, pp. 348–362, 2009. DOI: `10.1002/we.297`.

[30] H. J. Sutherland, "A summary of the fatigue properties of wind turbine materials," *Wind Energy*, vol. 3, no. 1, pp. 1–34, 2000. DOI: `http://dx.doi.org/10.1002/1099-1824(200001/03)3:1%C1::AID-WE28%3E3.0.CO;2-2`.

[31] J. Schijve, *Fatigue of Structures and Materials*. Springer, 2009, ISBN: 978-1-4020-6807-2.

[32] "International standard wind turbines – part 1: Design requirements," International Electrotechnical Commission, Tech. Rep., 2005.

[33] J. M. Jonkman and M. L. Buhl Jr., "Fast user's guide," National Renewable Energy Laboratory, Tech. Rep., Aug. 2005.

[34] B. Jonkman and J. Jonkman, "Fast v8.16.00a-bjj," National Renewable Energy Laboratory, Tech. Rep., Jul. 2016.

[35] E. Wiegant and R. Verzijlbergh, "Grasp model description & validation report," Whiffle Weather Forecasting, Tech. Rep., Dec. 2019.

[36] Wind @ Sea. (). "Locations," [Online]. Available: `https://www.windopzee.net/en/locations/`. (accessed: 16.12.2020).

[37] H. Verhoef, "Supply of meteorological and oceanographic data at borssele wind farm zone (bwfz): Monthly progress report: 11 june - 14 july 2015," ECN, Tech. Rep., Nov. 2015.

[38] ——, "Supply of meteorological and oceanographic data at borssele wind farm zone (bwfz) - lot 2: Monthly progress report: 12 february - 14 march 2016," ECN, Tech. Rep., Apr. 2016.

[39] RVO, "Supply of meteorological and oceanographic data at hollandse kust (zuid): Monthly data report: March 2017," Fugro Norway, Tech. Rep., May 2017.

[40] P. C. Kalverla, G.-J. Steeneveld, R. J. Ronda, and A. A. Holtslag, "An observational climatology of anomalous wind events at offshore meteomast ijmuiden (north sea)," *Journal of Wind Engineering and Industrial Aerodynamics*, vol. 165, pp. 86–99, 2017. DOI: `https://doi.org/10.1016/j.jweia.2017.03.008`.

[41] I. Troen and E. Lundtang Petersen, *European Wind Atlas*. Risø National Laboratory, 1989, ISBN: 87-550-1482-8.

[42] B. Jonkman, "Turbsim user's guide: Version 1.50," National Renewable Energy Laboratory, Tech. Rep., Sep. 2009.

[43] B. R. Resor, "Definition of a 5mw/61.5m wind turbine blade reference model," Sandia National Laboratories, Tech. Rep., Apr. 2013.

[44] V. Igwemezie, A. Mehmanparast, and A. Kolios, "Current trend in offshore wind energy sector and material requirements for fatigue resistance improvement in large wind turbine support structures – a review," *Renewable and Sustainable Energy Reviews*, vol. 101, pp. 181–196, 2019. DOI: `https://doi.org/10.1016/j.rser.2018.11.002`.

[45] P. Bortolotti, H. C. Tarres, K. Dykes, K. Merz, L. Sethuraman, D. Verelst, and F. Zahle, "Iea wind tcp task 37 on systems engineering in wind energy - wp2.1 reference wind turbines," NREL, Tech. Rep., May 2019.

[46] H. Kooijman, C. Lindenburg, D. Winkelaar, and E. van der Hooft, "Dowec 6 mw pre-design," ECN, Tech. Rep., Sep. 2003.

[47] S. SAHIN, *Wind turbine tower structure analysis according to wind load in terms of cost*, Szczecin, 2016.

[48] M. Seidel, S. Voormeeren, and J.-B. van der Steen, "State of the art design processes for offshore wind turbine support structures," *Stahlbau*, vol. 85, no. 9, pp. 583–590, 2016. DOI: `10.1002/stab.201610404`.

[49] K. Kluger, A. Karolczuk, and S. Derda, "Application of life-dependent material parameters to fatigue life prediction under multiaxial and non-zero mean loading," *Materials*, vol. 13, no. 7, pp. 1587–1604, 2020. DOI: `https://doi.org/10.3390/ma13071587`.

[50] J. Wieringa and P. J. Rijkoort, *Windklimaat van Nederland*. KNMI (Staatsuitgeverij), 1983, ISBN: 9012044669.

[51] DUWIND, *Inleiding windenergie*, Lecture notes CT5147.

[52] J. Jonkman, S. Butterfield, W. Musial, and G. Scott, "Definition of a 5-mw reference wind turbine for offshore system development," National Renewable Energy Laboratory, Tech. Rep., Feb. 2009.

[53] E. Gaertner, J. Rinker, L. Sethuraman, F. Zahle, B. Anderson, G. Barter, N. Abbas, F. Meng, P. Bortolotti, W. Skrzypinski, G. Scott, R. Feil, H. Bredmose, K. Dykes, M. Shields, C. Allen, and A. Viselli, "Definition of the iea wind 15-megawatt offshore reference wind turbine," National Renewable Energy Laboratory, Tech. Rep., Mar. 2020.

[54] N. Silva and A. Estanqueiro, "Impact of weather conditions on the windows of opportunity for operation of offshore wind farms in portugal," *Wind Engineering*, vol. 37, no. 3, pp. 257–268, 2013. DOI: `10.1260/0309-524X.37.3.257`.

[55] D. T. Griffith and T. D. Ashwill, "The sandia 100-meter all-glass baseline wind turbine blade: Snl100-00," Sandia National Laboratories, Tech. Rep., Jun. 2011.

[56] M. C. Holtslag, "Far offshore wind conditions in scope of wind energy," Ph.D. dissertation, Delft University of Technology, 2016. DOI: `https://doi.org/10.4233/uuid:3c66f401-6cff-4273-aa49-df4274ba767f`.

[57] N. Kelley, M. Shirazi, D. Jager, S. Wilde, J. Adams, M. Buhl, P. Sullivan, and E. Patton, "Lamar low-level jet project interim report," National Renewable Energy Laboratory, Tech. Rep., Jan. 2004.

[58] W. G. Rodriguez, "Low-level jet — wind turbine interactions and their impacts on performance, power production and mechanical responses: A numerical approach," Ph.D. dissertation, Texas Tech University, 2017.

[59] N. Cosack, S. Emeis, and M. K¨uhn, "On the influence of low-level jets on energy production and loading of wind turbines," *Wind Energy*, vol. 165, pp. 325–328, 2017. DOI: `https://doi.org/10.1007/978-3-540-33866-6_61`.

[60] J. M. Poveda and D. Wouters, "Wind measurements at meteorological mast ijmuiden," ECN, Tech. Rep., Feb. 2015.

A
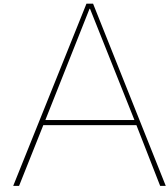
Stability

A.1. Vertical wind speed and temperature profiles
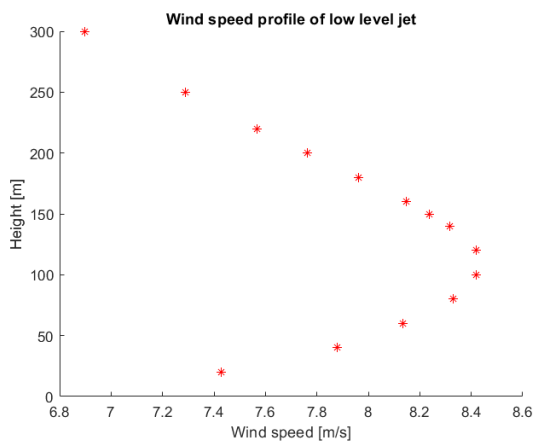
Figure A.1: Example of an identified low level jet
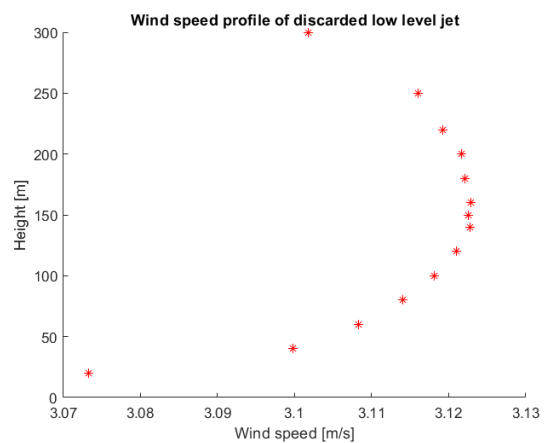
Figure A.2: Example of a wind profile that was not identified as low level jet because the wind speed difference is smaller than $0.5\frac{m}{s}$
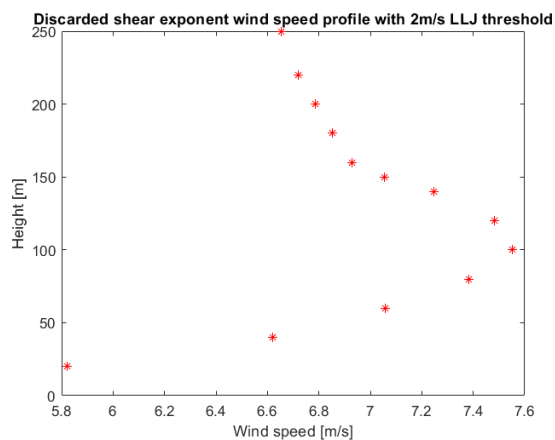
Figure A.3: Discarded shear exponent wind profile that should have been identified as LLJ
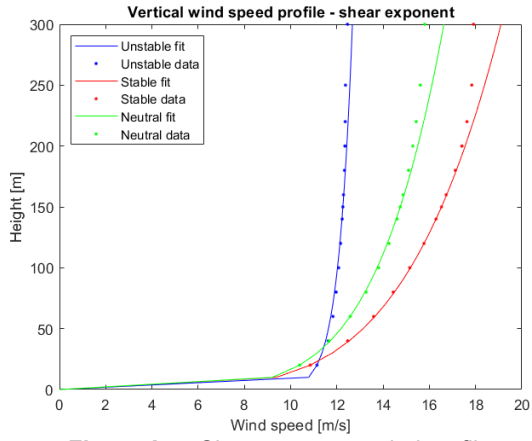
Figure A.4: Shear exponent wind profile
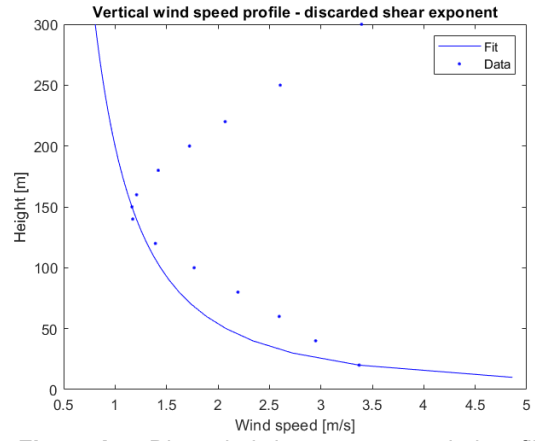
Figure A.5: Discarded shear exponent wind profile
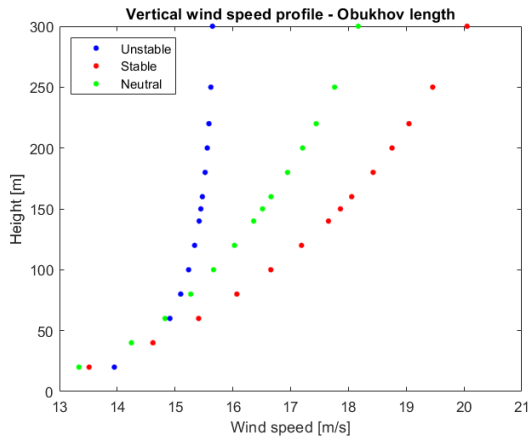
Figure A.6: Obukhov length wind profile
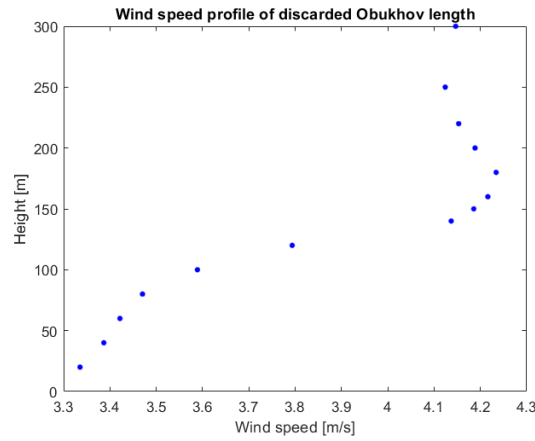
Figure A.7: Discarded Obukhov length wind profile
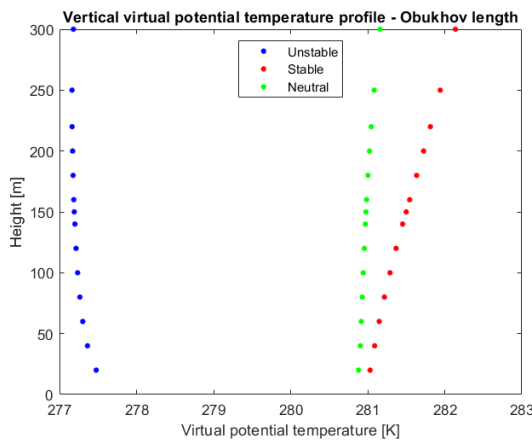
Figure A.8:
Obukhov length virtual potential temperature profile
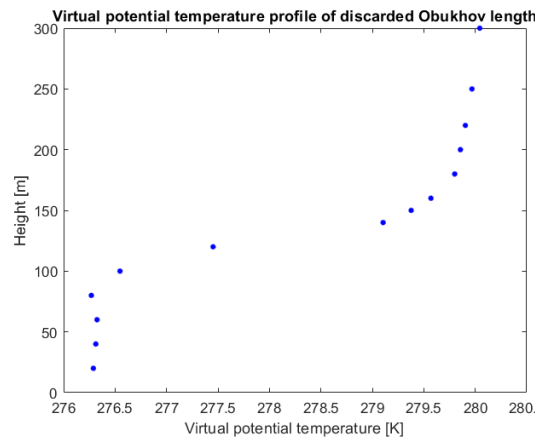
Figure A.9: Discarded
Obukhov length virtual potential temperature profile
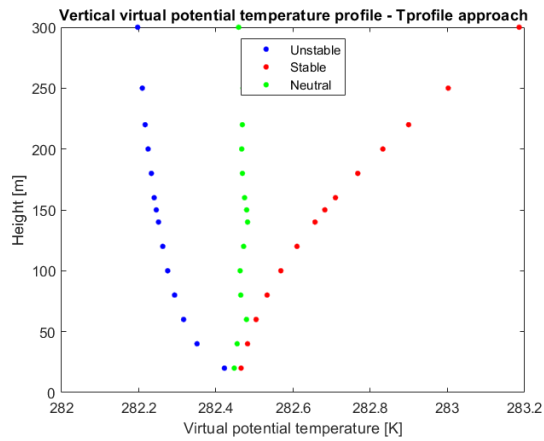
Figure A.10: Temperature profile approach - virtual potential temperature profile

A.2. Stability contour plots

A.2.1. Relative values
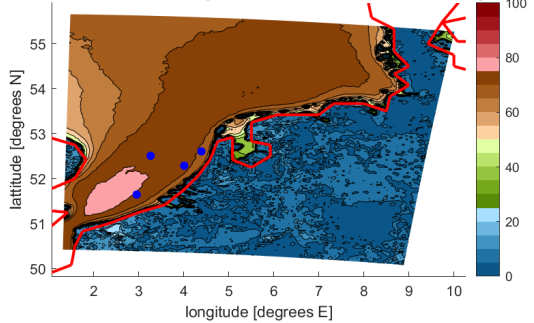
Figure A.11: Wind shear exponent, 150m, unstable
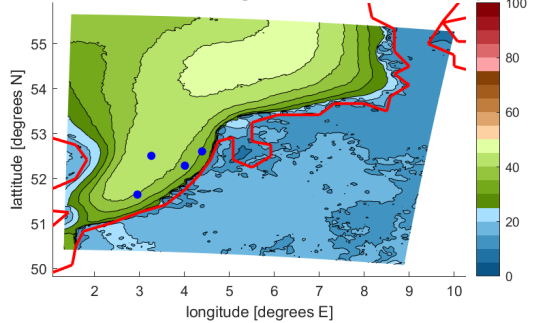
Figure A.12: Obukhov length, 150m, unstable
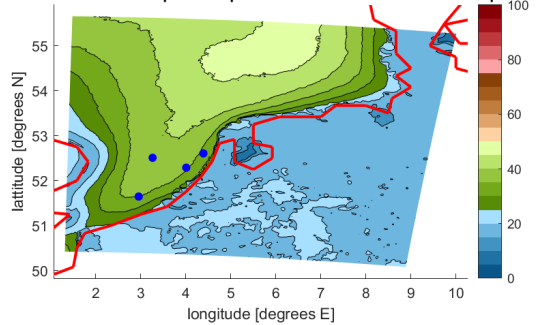
Figure A.13: Temperature profile, 150m, unstable
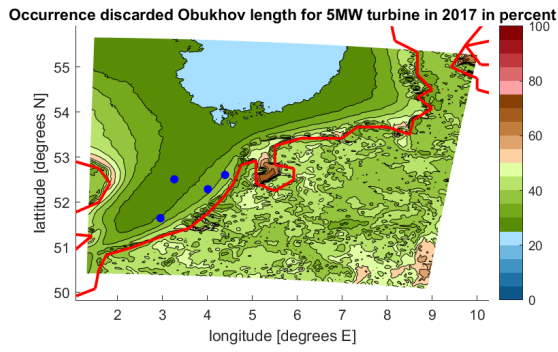
Figure A.14: Obukhov length, 90m, discarded
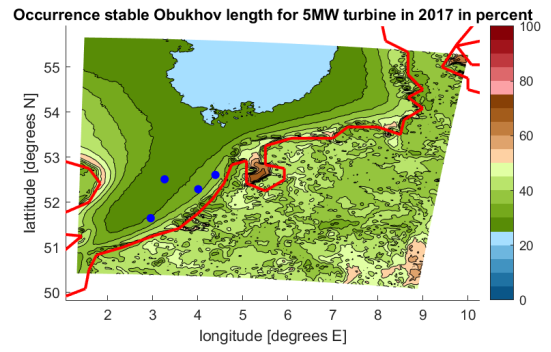
Figure A.15: Obukhov length, 90m, stable
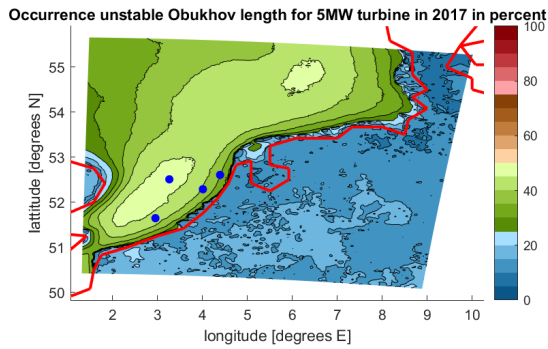
Figure A.16: Obukhov length, 90m, unstable
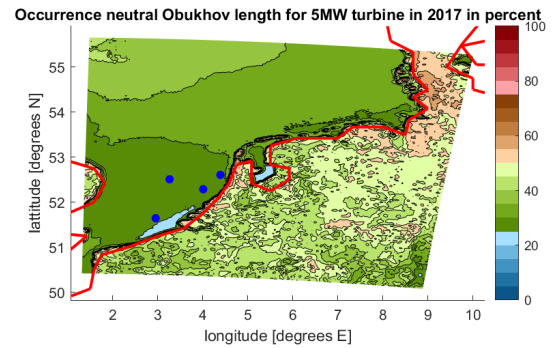
Figure A.17: Obukhov length, 90m, neutral

A.2.2. Absolute values
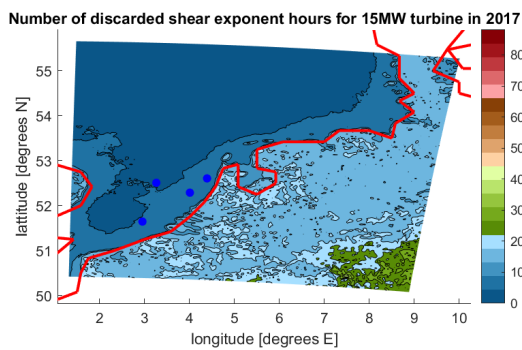
Figure A.18: Shear exponent, 150m, discarded
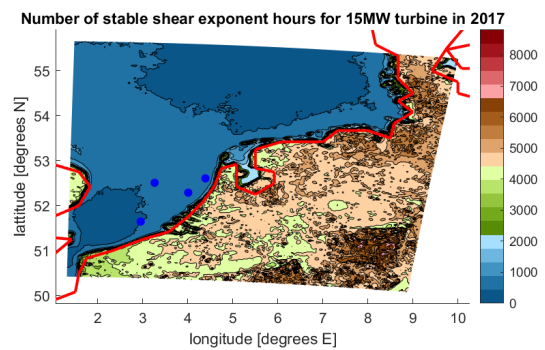
Figure A.19: Shear exponent, 150m, stable
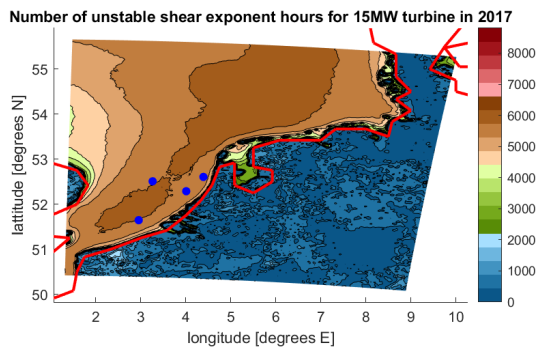
Figure A.20: Shear exponent, 150m, unstable
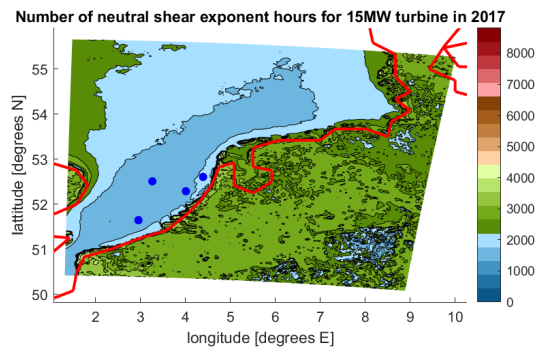
Figure A.21: Shear exponent, 150m, neutral
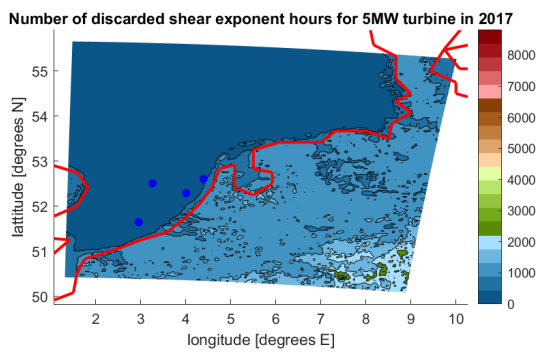
Figure A.22: Shear exponent, 90m, discarded
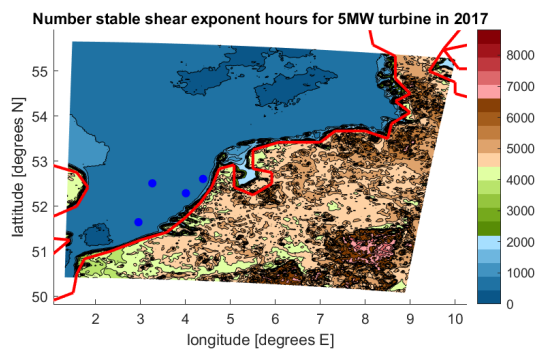
Figure A.23: Shear exponent, 90m, stable
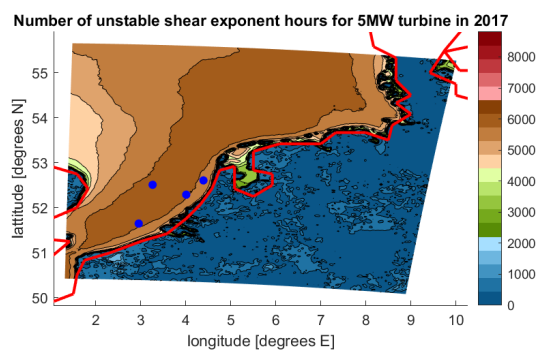
Figure A.24: Shear exponent, 90m, unstable
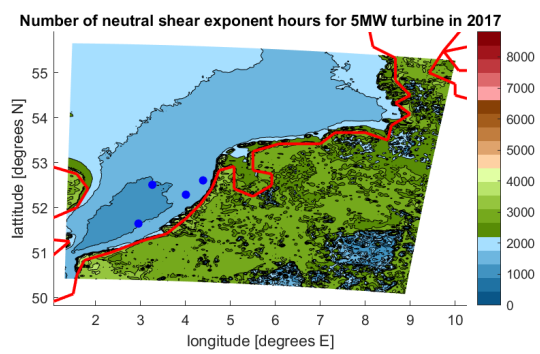
Figure A.25: Shear exponent, 90m, neutral
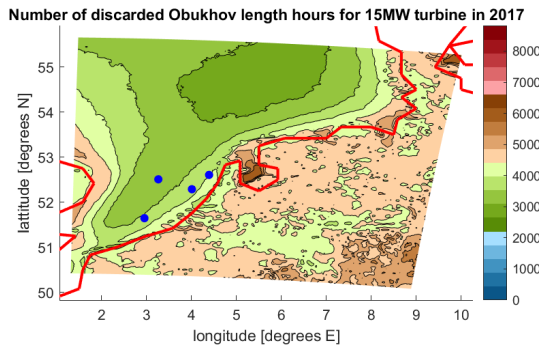
Figure A.26: Obukhov length, 150m, discarded
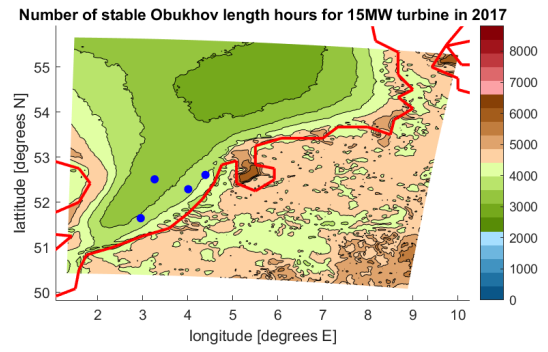
Figure A.27: Obukhov length, 150m, stable
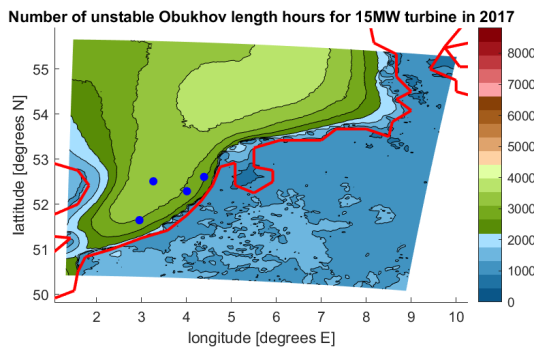
Figure A.28: Obukhov length, 150m, unstable
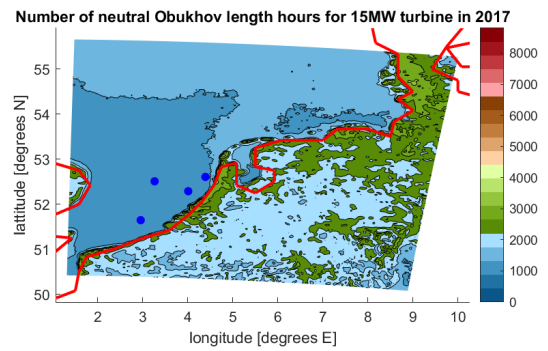
Figure A.29: Obukhov length, 150m, neutral
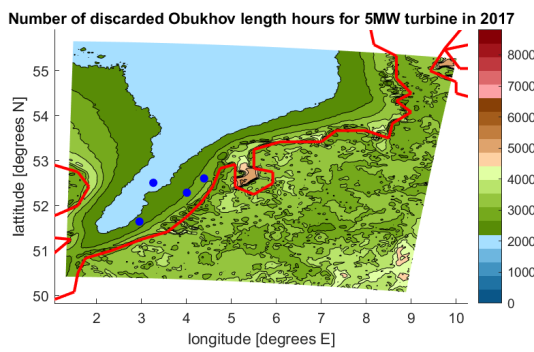
Figure A.30: Obukhov length, 90m, discarded
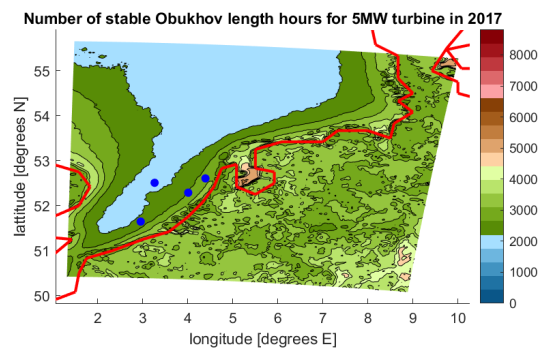
Figure A.31: Obukhov length, 90m, stable

Figure A.32: Obukhov length, 90m, unstable

Figure A.33: Obukhov length, 90m, neutral

Figure A.34: Temperature profile, 150m, stable

Figure A.35: Temperature profile, 150m, unstable

Figure A.36: Temperature profile, 150m, neutral

Number of stable temperature profile hours for 5MW turbine in 2017

Figure A.37: Temperature profile, 90m, stable

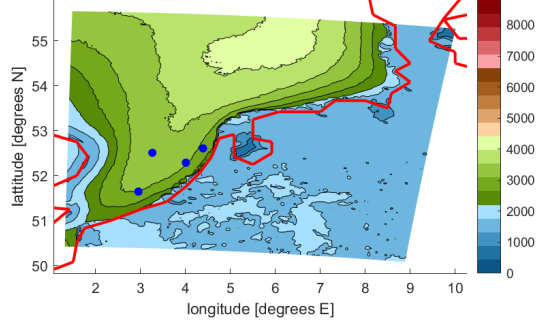**Number of unstable temperature profile hours for 5MW turbine in 2017**

Figure A.38: Temperature profile, 90m, unstable

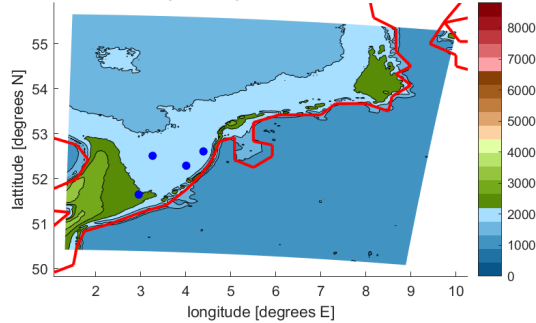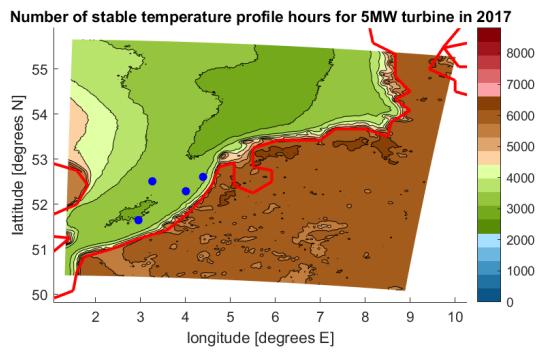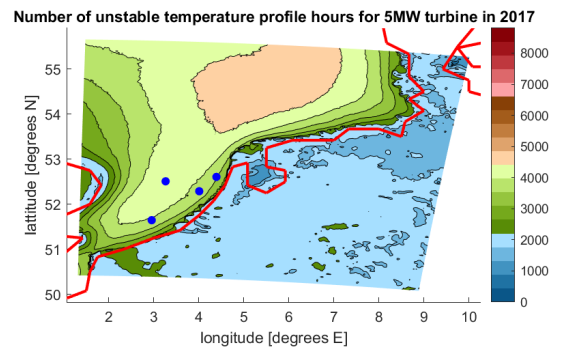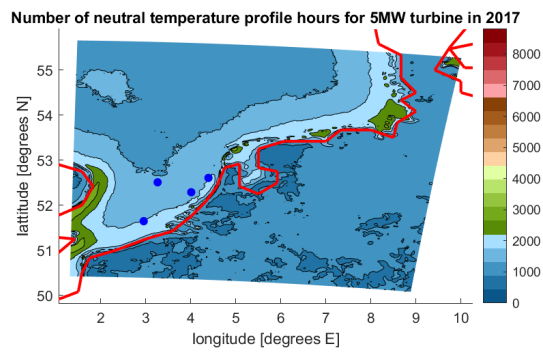**Number of neutral temperature profile hours for 5MW turbine in 2017**

Figure A.39: Temperature profile, 90m, neutral
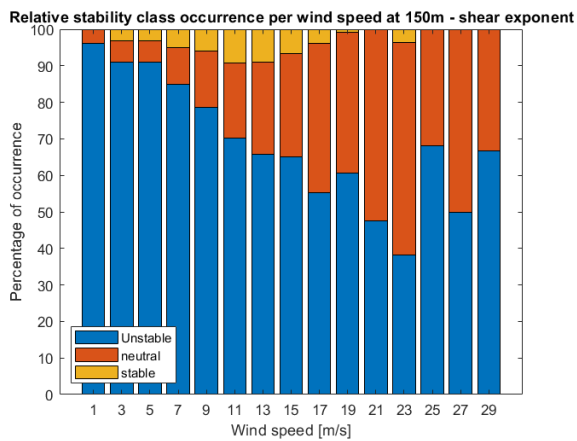
A.3. Stability histograms

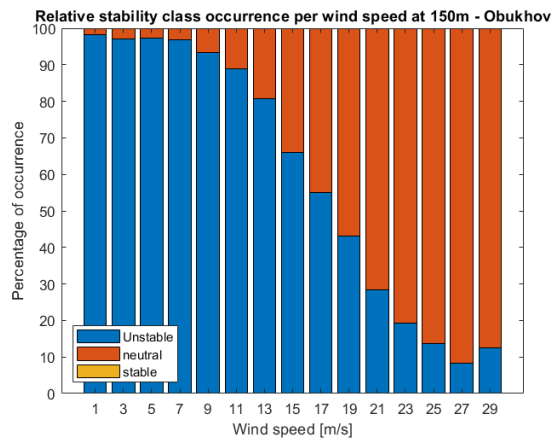**Figure A.40:**
Stability histogram Borssele - Obukhov comparison

Figure A.41: Stability histogram Borssele - shear exponent comparison
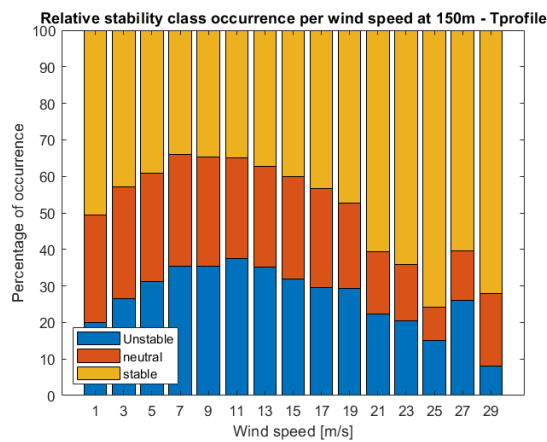

Figure A.42:
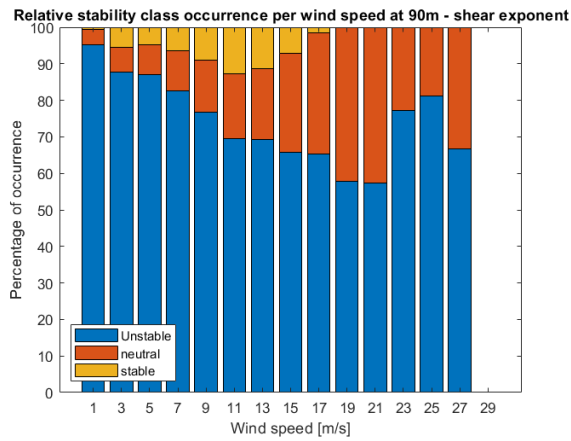Stability histogram Borssele - Tprofile comparison

Figure A.43: Stability histogram Borssele - shear exponent comparison
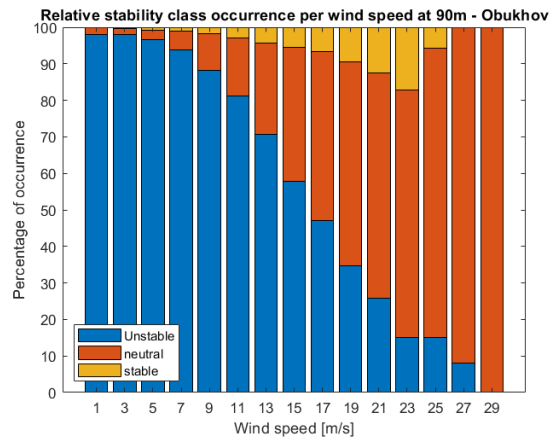

Figure A.44: Stability histogram Borssele - Obukhov length comparison
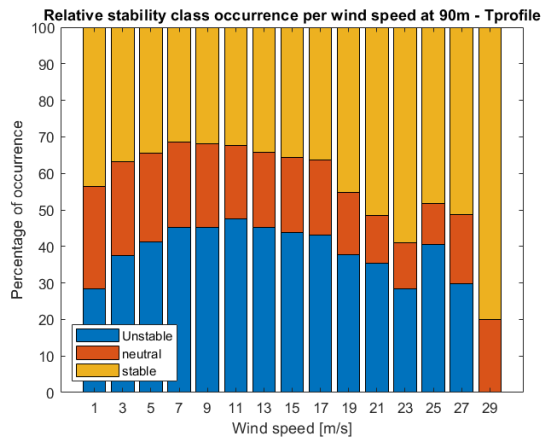
Figure A.45: Stability histogram Borssele - Tprofile comparison

Figure A.46: Stability histogram HKZ - shear exponent, 90m

Figure A.47: Stability histogram HKZ - Obukhov length, 90m

Figure A.48:
Stability histogram HKZ - temperature profile, 90m

Figure A.49:
Stability histogram HKZ - temperature profile, 150m

Figure A.50:
Stability histogram HKN - shear exponent, 90m

Figure A.51:
Stability histogram HKN - Obukhov length, 90m

Figure A.52:
Stability histogram HKN - temperature profile, 90m

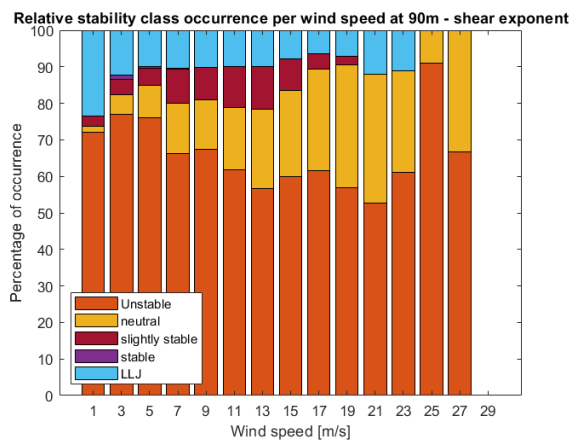**Figure A.53:**
Stability histogram HKN - temperature profile, 150m
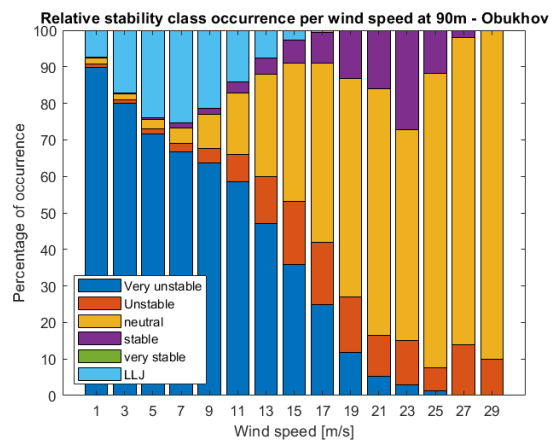
Figure A.54:
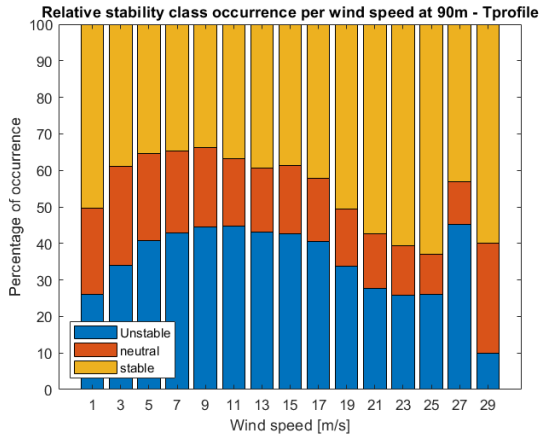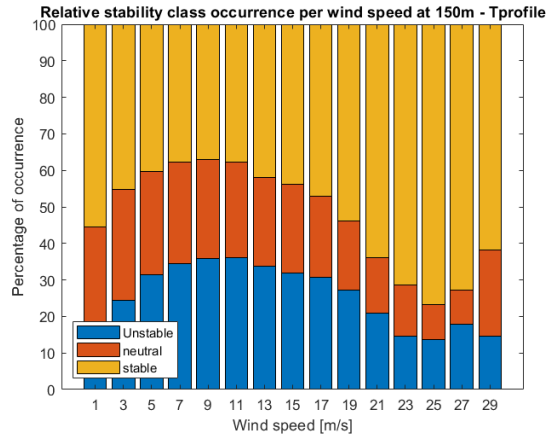Stability histogram MMIJ - shear exponent, 90m
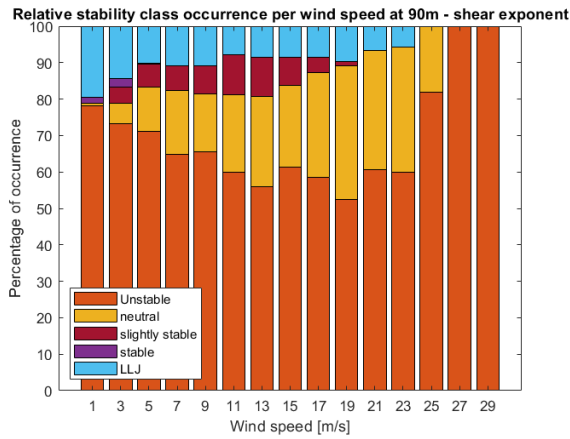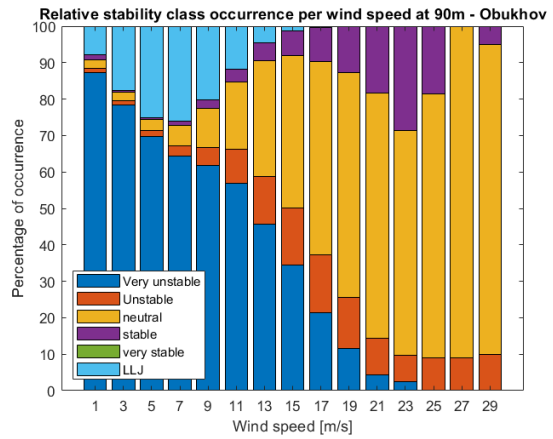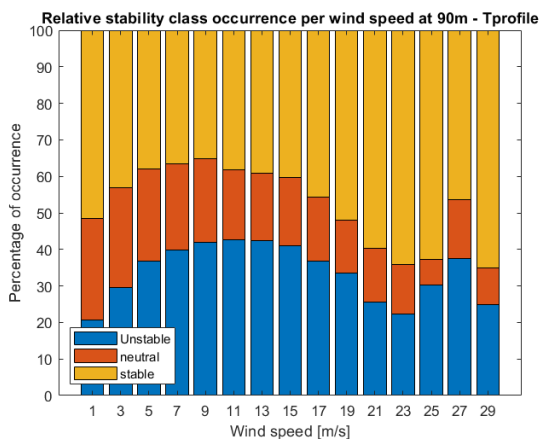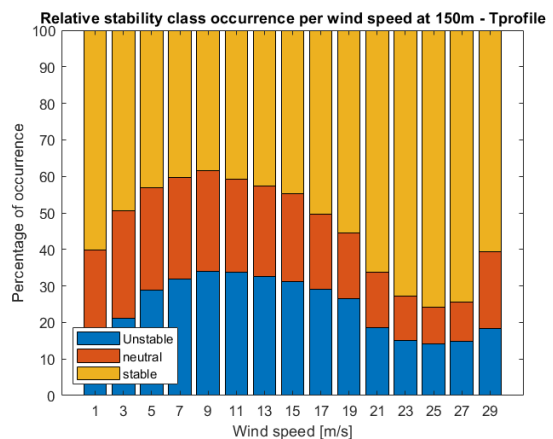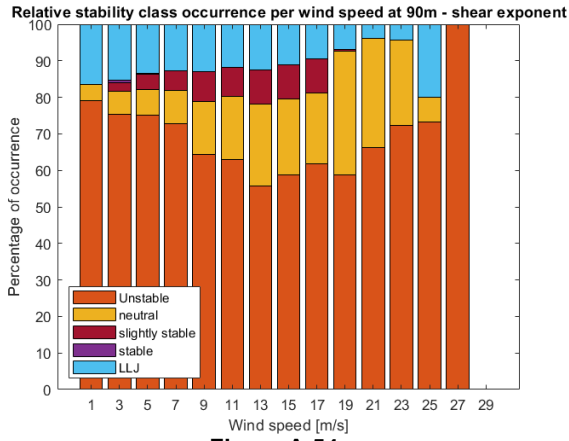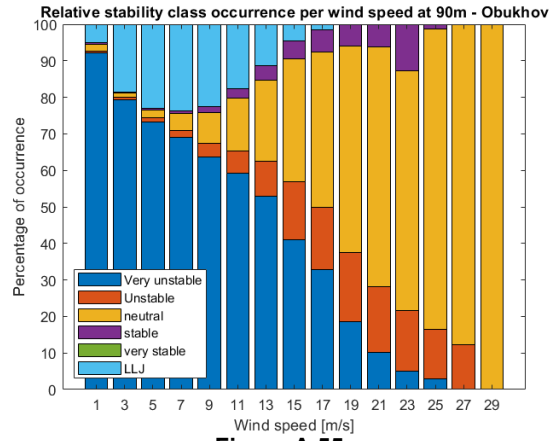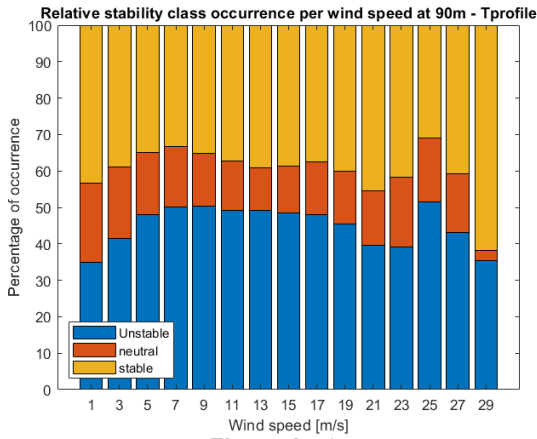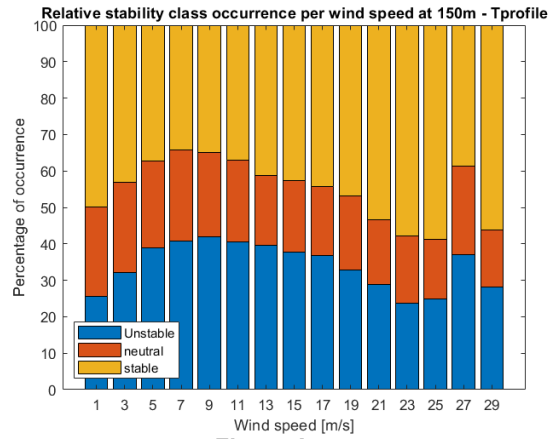

Figure A.55:
Stability histogram MMIJ - Obukhov length, 90m

Figure A.56:
Stability histogram MMIJ - temperature profile, 90m

Figure A.57:
Stability histogram MMIJ - temperature profile, 150m

B

Energy yield

B.1. TI correction verification

The turbulence intensity correction for energy yield given by equation 2.19 can be verified in FAST. In order to do this, two simulations are run. The first simulation includes turbulence intensity using the Normal Turbulence Model and IEC class 1C, corresponding to $TI = 0.12$. The second simulation is run for a steady wind, so without turbulence. The wind input files are plotted in figure B.1 and the power output is shown in figure B.2. The first 60 seconds of the simulation are discarded due to initialisation effects. The generator power output for both cases can be summed and compared. This analysis is performed for several wind speeds below the rated wind speed and for two different turbulence intensity values.
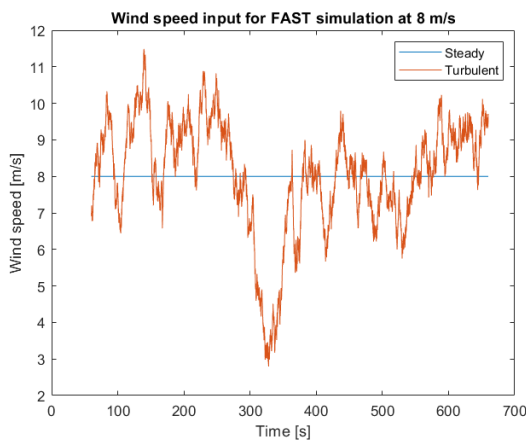
Figure B.1: Wind speed input for 5MW reference turbine and 8 m/s average
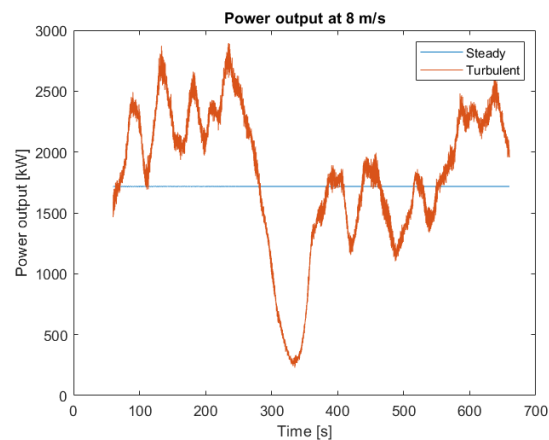
Figure B.2: Generator power output of 5MW reference turbine and 8 m/s average wind speed

The ratio of power generation with turbulence and without turbulence is shown in table B.1 for a turbulence intensity of 12% and in table B.2 for a turbulence intensity of 6%. In order to eliminate randomness in the simulations, three different seeds are used but they give exactly the same ratios. When equation 2.19 is applied to correct the wind speeds and the cube of these wind speeds is taken, the ratio of the cube of the wind speeds with turbulence intensity correction and without turbulence intensity correction is calculated to be 1.043 and 1.0108 for turbulence intensities of 0.12 and 0.06, respectively. When comparing to this the ratios found by the simulations, it can be seen that the difference is largest for a wind speed of $6\frac{m}{s}$. For some wind speeds the difference is negative, this means that the turbulence intensity correction actually underestimates the additional power output associated with turbulence intensity. However in most cases, the turbulence intensity correction equation will overestimate the additional power to be generated from

91

the turbulence, especially for low turbulence intensities. The reason for this is that for low turbulence intensities, the simulations show that the turbulence intensity has a negative effect on power output while the equation assumes that turbulence intensity always increases power output compared to steady wind.

Table B.1: Ratio of $\frac{P_{turbulence}}{P_{steady}}$ with TI=0.12

Wind speed [m/s]	Equation ratio	Simulation ratio seed 1	Simulation ratio seed 2	Simulation ratio seed 3	Difference [%]
4	1.0432	1.0437	1.0437	1.0437	-0.05
5	1.0432	1.0656	1.0656	1.0656	-2.24
6	1.0432	0.9926	0.9926	0.9926	5.06
7	1.0432	1.0106	1.0106	1.0106	3.26
8	1.0432	1.0600	1.0599	1.0599	-1.68
9	1.0432	1.0524	1.0524	1.0524	-0.92

Table B.2: Ratio of $\frac{P_{turbulence}}{P_{steady}}$ with TI=0.06

Wind speed [m/s]	Equation ratio	Simulation ratio seed 1	Simulation ratio seed 2	Simulation ratio seed 3	Difference [%]
4	1.0108	0.9656	0.9656	0.9656	4.52
5	1.0108	0.9865	0.9865	0.9865	2.43
6	1.0108	0.9692	0.9692	0.9692	4.16
7	1.0108	0.9794	0.9794	0.9794	3.14
8	1.0108	0.9934	0.9934	0.9934	1.74
9	1.0108	0.9929	0.9929	0.9929	1.79

B.2. Energy yield contour plots
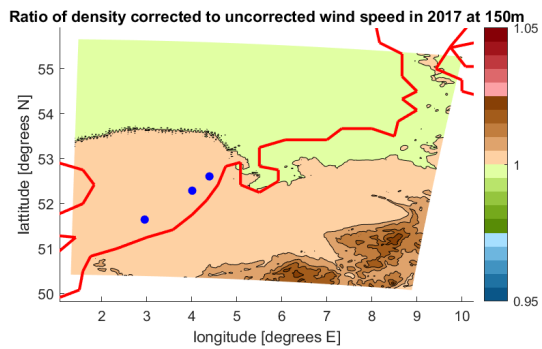
Figure B.3:
Ratio of wind speed with and without density correction
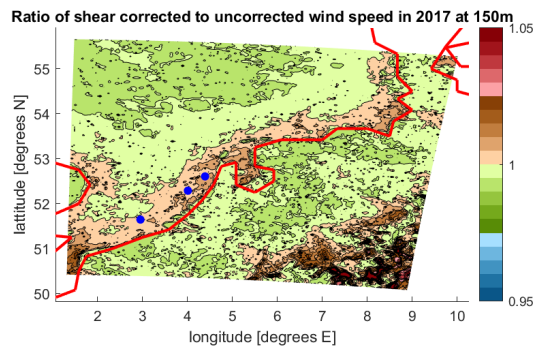
Figure B.4:
Ratio of wind speed with and without shear correction
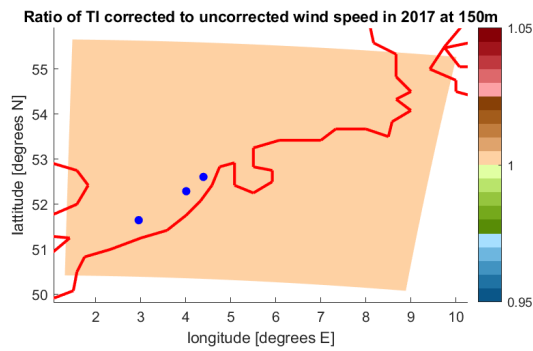
Figure B.5:
Ratio of wind speed with and without TI correction
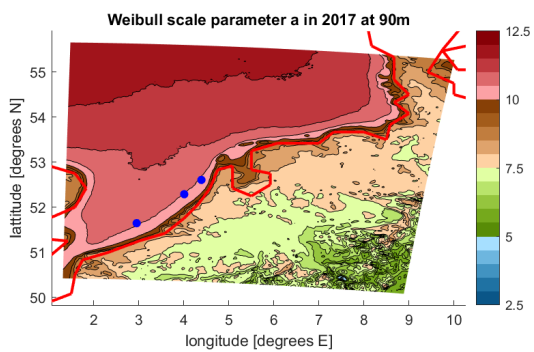
Figure B.6:
90m Weibull scale parameter with stability correction
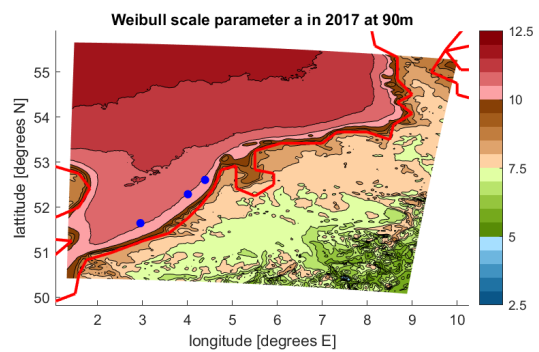
Figure B.7:
90m Weibull scale parameter without stability correction
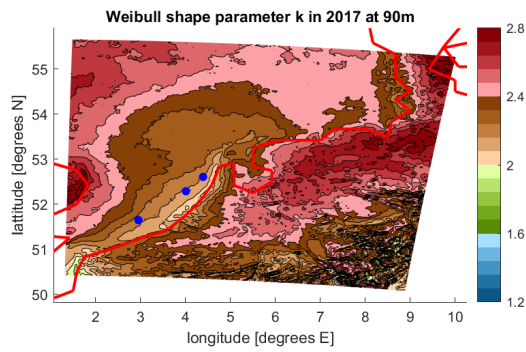
Figure B.8:
90m Weibull shape parameter with stability correction
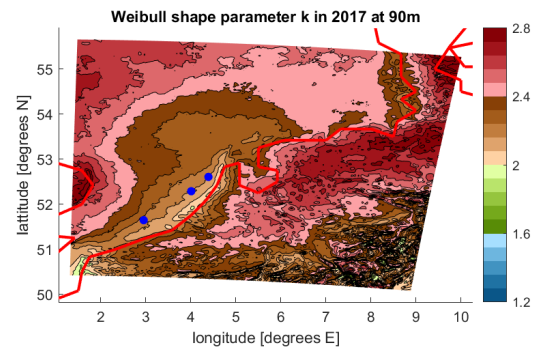
Figure B.9:
90m Weibull shape parameter without stability correction

Table B.3:
Weibull parameters and energy yield for three wind farm locations at $90m$ using 10-minute and hourly values

Parameter		a[-]	k[-]	Energy yield [GWh]
Borssele	DOWA nondirectional	10.6	2.2	23.3
	DOWA hourly	-	-	23.4
	DOWA data	-	-	23.5
	Analytical	-	-	23.3
	LES hourly	10.1	2.1	21.9
	LES 10-minute	10.1	2.1	21.9
HKZ	DOWA nondirectional	10.5	2.2	23.0
	DOWA hourly	-	-	23.1
	DOWA data	-	-	23.1
	Analytical	-	-	23.1
	LES hourly	10.3	2.1	22.2
	LES 10-minute	10.3	2.1	22.2
HKN	DOWA nondirectional	10.5	2.2	22.9
	DOWA hourly	-	-	22,8
	DOWA data	-	-	22.9
	Analytical	-	-	23.0
	LES hourly	10.5	2.2	22.7
	LES 10-minute	10.5	2.2	22.7

B.3. Wind roses
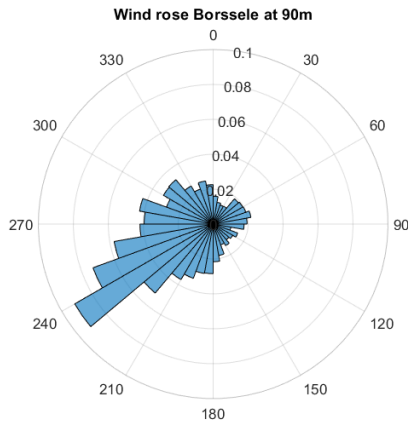
Figure B.10:
Wind rose at Borssele location at 90m using DOWA data
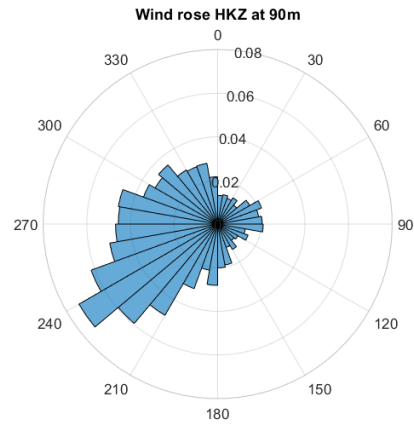
Figure B.11:
Wind rose at HKZ location at 90m using DOWA data
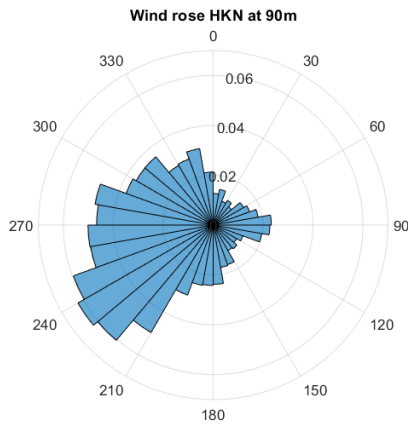
Figure B.12:
Wind rose at HKN location at 90m using DOWA data
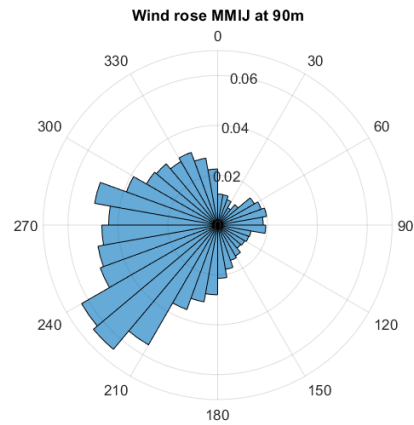
Figure B.13:
Wind rose at MMIJ location at 90m using DOWA data
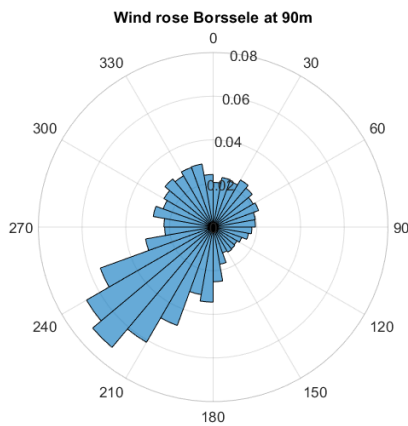
Figure B.14: Wind rose
at Borssele location at 90m using site measurements
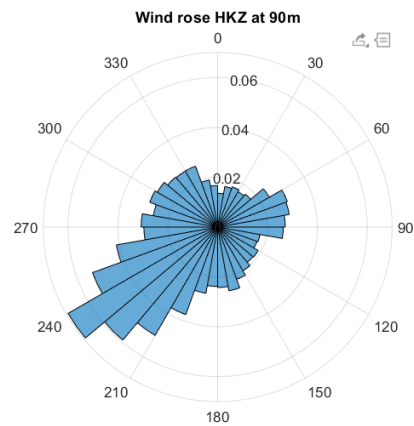
Figure B.15: Wind
rose at HKZ location at 90m using site measurements

B.4. Weibull fit verification

This section is to verify that the Weibull fit code written for the analyses in this report satisfies the condition that the energy content of the fit should be the same as the energy content as the data, as dictated by the European Wind Atlas method. This verification is performed for the HKZ wind farm location at $150m$, for which the Weibull fit of the sector $60° - 90°$ was already shown in figure 5.55. The energy content of the data and the fit as well as the ratio between them is shown for every sector in table B.4. Note that the energy content is represented by $\sum p \cdot U^3$, where p is the probability of occurrence and U is the wind speed. It can be seen that there are minor differences between the energy content in the data and the Weibull fit. These are likely caused by the discretisation of $0.5 \frac{m}{s}$ that was used for this verification.

Table B.4: Weibull fit verification of energy content

Sector [°]	$\sum p_{data} \cdot U_{data}^3$	$\sum p_{fit} \cdot U_{fit}^3$	$\frac{\sum p_{data} \cdot U_{data}^3}{\sum p_{fit} \cdot U_{fit}^3}$
0-30	1090.8	1081.1	1.0089
30-60	1203.6	1199.0	1.0039
60-90	1407.5	1410.5	0.9979
90-120	1732.7	1732.6	1.0001
120-150	1280.5	1274.8	1.0045
150-180	2393.2	2383.2	1.0042
180-210	4464.9	4381.2	1.0191
210-240	5207.9	5175.2	1.0063
240-270	4674.7	4674.7	1.0000
270-300	3123.9	3127.5	0.9989
300-330	2480.4	2477.0	1.0014
330-360	2343.7	2345.7	0.9991

C
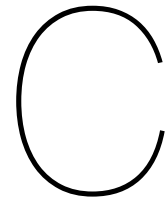
Fatigue

C.1. FASTTool user guide

In order to use the simulink interface with GUI created by the Data-Driven Controls department of the TU Delft, the FASTTool should be downloaded from the GitHub repository [1]. The corresponding directory should be opened in MATLAB, after which the file 'FASTTool.m' should be run. This will open the GUI that contains several modules to change input parameters, linearise input files and run simulations. In order to start using the program, an input file has to be loaded. The 'NREL5MW.mat' file can easily be opened as it is already included in the GitHub download. In order to perform simulations for the $15MW$ reference turbine, an input file should be written. To do this, the 'NREL5MW.mat' file can be used as a starting point and the parameters should be changed according to subsection C.2.2.

All simulations in this report are performed with the 'Certification' module under the 'Run' tab. In this module, the wind speed, run time and seed number can be changed according to the parameters specified in section 4.3. It is possible to specify multiple wind speeds and seed numbers, for example if $[5:0.5:10]$ is entered in the wind speed field, FASTTool will run the simulation for all wind speeds in the range of 5 to $10\frac{m}{s}$ with a step size of 0.5. The same can be done for the seed number, where for example $[1,3,6]$ will run seed numbers 1, 3 and 6. Furthermore, the NTM should be used during power production. The IEC classes to be used were already discussed in section 4.3. Specify an output file name and simply click 'run' to perform the simulation.

In order to obtain the results described in this report, some minor changes have to be made to the FAST-Tool code to allow for different inputs of turbulence intensity. These changes are as follows:

- Open the file 'Wind.fig' (to be found in the subfunctions folder) in GUIDE, this can be done by right-clicking 'Wind.fig' and selecting 'Open in GUIDE'. Right-click the button related to IEC class A and choose the 'Object Browser' option. Double-click 'UIControl(WindTurbulence"A")' and click on the editing icon in the row corresponding to the 'String' variable. Here, add options 'D' and 'E' to the list in order to allow for selection of these options in the GUI. Save the figure and continue with the next step.
- In the file 'Wind.m' (to be found in the subfunctions folder), after line 634, add the following code:

```
elseif get(handles.WindTurbulence,'Value')==4
    Iref=0,05
elseif get(handles.WindTurbulence,'Value')==5
    Iref=0.06
```

This will make sure the correct wind input file is written based on I_{ref}
- In the file 'InflowWind.m', change line 124 and 125 to the following code:

```
ABCDE = 'ABC56';
IECturbc = ABCDE(Wind.Class(2));
```

---

[1] https://github.com/TUDelft-DataDrivenControl/FASTTool

This will make sure the correct value is used for the TurbSim input file. TurbSim takes 'A','B' or 'C' as input values for the corresponding IEC classes, but it will also take turbulence intensity values in percent. In this case, when class 'D' is selected it will take 5% as input value and if class 'E' is selected it will take 6% turbulence intensity.

- In case an error is shown during the simulation stating that the Mach number over the airfoil exceeds the value of 1, the following change should be made. In the file 'AeroDyn.m', in line 29, change the type of skewed-wake correction model from 2 to 1. This means the model is changed from 'Pitt-Peters' to 'uncoupled' and should resolve the issue. Note that in newer versions of AeroDyn, this error should not occur in the first place.

C.2. Reference turbines

Two reference turbines are used during the calculations in this report. Subsection C.2.1 will provide information regarding the NREL 5MW offshore reference turbine while the IEA 15MW offshore reference turbine will be outlined in subsection C.2.2. The overview provided in this section will be focused mainly on the parameters needed to run FAST simulations.

C.2.1. NREL 5MW offshore reference turbine

The most important parameters of the NREL $5MW$ offshore reference wind turbine will be outlined in this subsection. These parameters include the blades, airfoils, tower, nacelle, control properties and drive train configuration. The power curve of this wind turbine is given in figure C.1 and some general are given in table C.1.
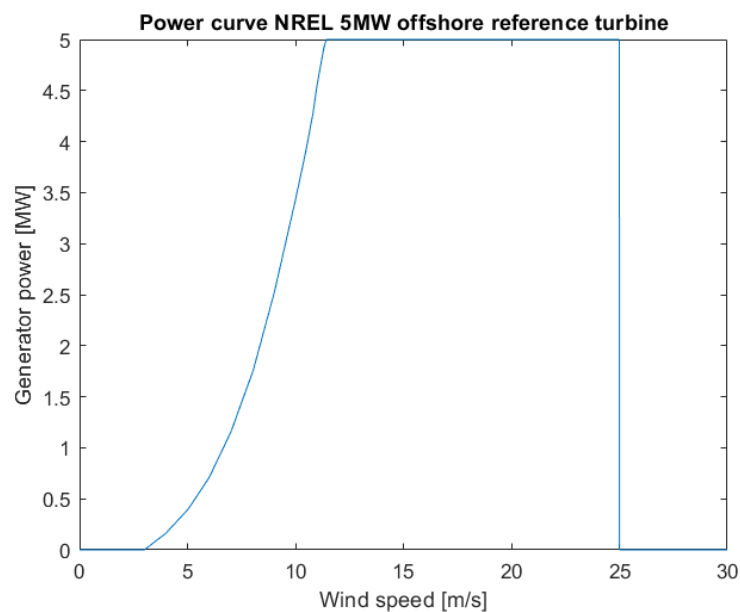
Figure C.1: Power curve NREL 5MW offshore reference turbine [52]

Table C.1: $5MW$ reference turbine general properties

Rated power [MW]	5
Rated wind speed [m/s]	11.4
Speed range [rpm]	9-12.1
Optimal tip speed ratio [-]	7.6
Peak power coefficient [-]	0.478

Blades

Table C.2 shows the blade properties of the $5MW$ wind turbine blade. The airfoils are not exactly the same as the ones provided in the original NREL report but have similar properties. Data for these airfoils is publicly available. The blades are made out of the composite materials E-LT-5500 which is uni-axial in the $0°$ direction and Saertex which is a double bias material in the $\pm45°$ directions. An additional material is used called SNL Triax, this is a combinations of the aforementioned materials, meaning it will have three fibre directions; $0°$ and $\pm45°$. All materials have an EP-3 resin and the relevant fatigue parameters can be found in the DOE/MSU composite fatigue database. The root section of the blade consists only out of SNL Triax material, where in the further root buildup a combination of SNL Triax and the other two materials is used (for example in the spar caps).

Table C.2: $5MW$ reference turbine blade properties

| Radius [m]	Chord [m]	Twist [degree]	Airfoil	Mass density [kg/m]	Flapwise stiffness [Nm^2]	Edgewise stiffness [Nm^2]
1.5000	3.3860	13.3080	Cylinder 1	678.9350	1.8110e+10	1.8114e+10
2.7000	3.5230	13.3080	Cylinder 1	773.3630	1.9425e+10	1.9559e+10
3.7000	3.6371	13.3080	Cylinder 1	740.5500	1.7456e+10	1.9498e+10
4.7000	3.7513	13.3080	Cylinder 1	740.0420	1.5287e+10	1.9789e+10
5.7000	3.8654	13.3080	Cylinder 1	592.4960	1.0782e+10	1.4859e+10
6.7000	3.9799	13.3080	Cylinder 1	450.2750	7.2297e+09	1.0221e+10
7.7000	4.0945	13.3080	Cylinder 2	424.0540	6.3095e+09	9.1447e+09
8.7000	4.2088	13.3080	Cylinder 2	400.6380	5.5284e+09	8.0632e+09
9.7000	4.3231	13.3080	Cylinder 2	382.0620	4.9801e+09	6.8844e+09
10.7000	4.4371	13.3080	DU 99-W-405	399.6550	4.9368e+09	7.0092e+09
11.7000	4.5513	13.3080	DU 99-W-405	426.3210	4.6917e+09	7.1677e+09
12.7000	4.5790	13.1810	DU 99-W-405	416.8200	3.9495e+09	7.2717e+09
13.7000	4.6022	12.8480	DU 99-W-405	406.1860	3.3865e+09	7.0817e+09
14.7000	4.6254	12.1920	DU 99-W-350	381.4200	2.9337e+09	6.2445e+09
15.7000	4.6485	11.5610	DU 99-W-350	352.8220	2.5690e+09	5.0490e+09
16.7000	4.6118	11.0720	DU 99-W-350	349.4770	2.3887e+09	4.9485e+09
17.7000	4.5645	10.7920	DU 99-W-350	346.5380	2.2720e+09	4.8080e+09
19.7000	4.4698	10.2320	DU 99-W-350	339.3330	2.0501e+09	4.5014e+09
21.7000	4.3688	9.6720	DU 99-W-350	330.0040	1.8283e+09	4.2441e+09
23.7000	4.2668	9.1100	DU 97-W-300	321.9900	1.5887e+09	3.9953e+09
25.7000	4.1516	8.5340	DU 97-W-300	313.8200	1.3619e+09	3.7508e+09
27.7000	4.0336	7.9320	DU 91-W2-250	294.7340	1.1024e+09	3.4471e+09
29.7000	3.9090	7.3210	DU 91-W2-250	287.1200	875800000	3.1391e+09
31.7000	3.7827	6.7110	DU 91-W2-250	263.3430	681300000	2.7342e+09
33.7000	3.6610	6.1220	DU 91-W2-250	253.2070	534720000	2.5549e+09
35.7000	3.5410	5.5460	DU 93-W-210	241.6660	408900000	2.3340e+09
37.7000	3.4210	4.9710	DU 93-W-210	220.6380	314540000	1.8287e+09
39.7000	3.3010	4.4010	DU 93-W-210	200.2930	238630000	1.5841e+09
41.7000	3.1810	3.8340	DU 93-W-210	179.4040	175880000	1.3234e+09
43.7000	3.0610	3.3320	NACA 64-618	165.0940	126010000	1.1837e+09
45.7000	2.9410	2.8900	NACA 64-618	154.4110	107260000	1.0202e+09
47.7000	2.8210	2.5030	NACA 64-618	138.9350	90880000	797810000
49.7000	2.7009	2.1160	NACA 64-618	129.5550	76310000	709610000
51.7000	2.5810	1.7300	NACA 64-618	107.2640	61050000	518190000
53.7000	2.4610	1.3420	NACA 64-618	98.7760	49480000	454870000
55.7000	2.3410	0.9540	NACA 64-618	90.2480	39360000	395120000
56.7000	2.2687	0.7600	NACA 64-618	83.0010	34670000	353720000
57.7000	2.1857	0.5740	NACA 64-618	72.9060	30410000	304730000
58.7000	2.1026	0.4040	NACA 64-618	68.7720	26520000	281420000
59.2000	2.0128	0.3190	NACA 64-618	66.2640	23840000	261710000
59.7000	1.8905	0.2530	NACA 64-618	59.3400	19630000	158810000
60.2000	1.7688	0.2160	NACA 64-618	55.9140	16000000	137880000
60.7000	1.6468	0.1780	NACA 64-618	52.4840	12830000	118790000
61.2000	1.5248	0.1400	NACA 64-618	49.1140	10080000	101630000
61.7000	1.4028	0.1010	NACA 64-618	45.8180	7550000	85070000
62.2000	1.2807	0.0620	NACA 64-618	41.6690	4600000	64260000
62.7000	1.1587	0.0230	NACA 64-618	11.4530	250000	6610000
63	1.0855	0	NACA 64-618	10.3190	170000	5010000

Tower

Table C.3 shows the tower dimensions of the $5MW$ reference turbine with a hub height of $90m$.

Table C.3: $5MW$ turbine tower dimensions

Height [m]	Diameter [m]	Wall thickness [m]
0	6	0.0350
8.7600	5.7870	0.0340
17.5200	5.5740	0.0330
26.2800	5.3610	0.0320
35.0400	5.1480	0.0310
43.8000	4.9350	0.0300
52.5600	4.7220	0.0290
61.3200	4.5090	0.0280
70.0800	4.2960	0.0270
78.8400	4.0830	0.0260
87.6000	3.8700	0.0250

Nacelle

Figure C.2 shows the nacelle properties of the $5MW$ reference turbine. The most important parameters are the hub mass of $56{,}780kg$ and the nacelle mass of $240{,}000kg$ with a tilt angle of $5°$.
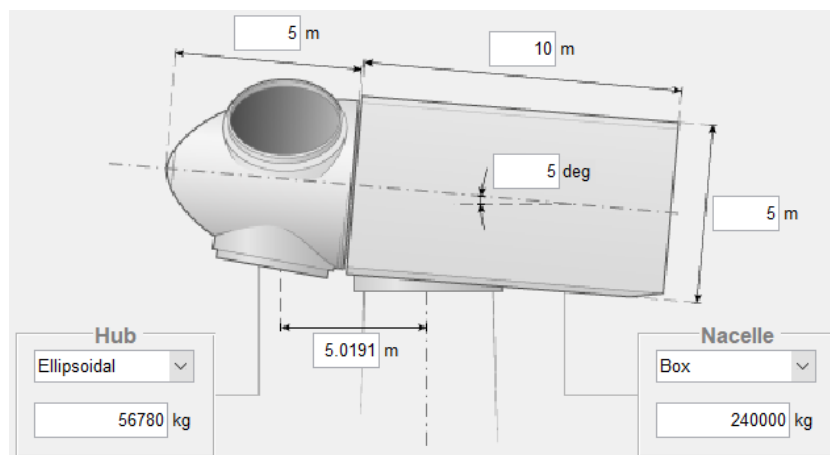
Figure C.2: Nacelle properties of the $5MW$ reference turbine

Control

For the control parameters, a cut-in wind speed of $3\frac{m}{s}$ and a cut-out wind speed of $25\frac{m}{s}$ are specified. All other relevant control parameters are summarised in table C.4. This wind turbine uses pitch control with a PI controller and constant gain as well as a 1st order low-pass filter. The brake is located on the high speed shaft. Indices A, B, B2 and C relate to the control regions.

**Table C.4:** $5MW$ reference turbine control parameters

Pitch control	
Fine pitch angle [deg]	0
Max. pitch angle [deg]	90
Min. pitch angle [deg]	-2
Max. pitch rate [deg/s]	8
Min. pitch rate [deg/s]	-8
Start-up pitch angle [deg]	45
Start-up pitch rate [deg/s]	1
Speed for start-up [rpm]	0.25
Low pass filter cut-off frequency [rad/s]	3
Kp [-]	-0.003
Ki [-]	-0.001
Torque control	
Demanded torque [Nm]	43093.55
Torque minimum [Nm]	200
Torque limit [Nm]	47403
Torque slew rate [N]	15000
Generator speed, A [rpm]	670
Generator speed, B [rpm]	871
Generator speed, B2 [rpm]	1150.9
Generator speed, C [rpm]	1173.7
Optimal mode gain [(Nm)/(rad/s)^2]	2.3323
Generator speed low-pass cut-off [rad/s]	3
Brake	
Brake torque [Nm]	28116
Deploy time [s]	0.6
Delay [s]	1.5

Drive train

The drive train of the $5MW$ reference turbine consists of a generator with an efficiency of 94.4% and an inertia of $534.116 kgm^2$. It is attached to a gearbox with 100% efficiency and a gearboc ratio of 97.

C.2.2. IEA 15MW offshore reference turbine

The most important parameters of the IEC $15MW$ offshore reference wind turbine will be outlined in this subsection. These parameters include the blades, airfoils, tower, nacelle, control properties and drive train configuration. The power curve of this turbine is shown in figure C.3 and some general properties are given in table C.5.
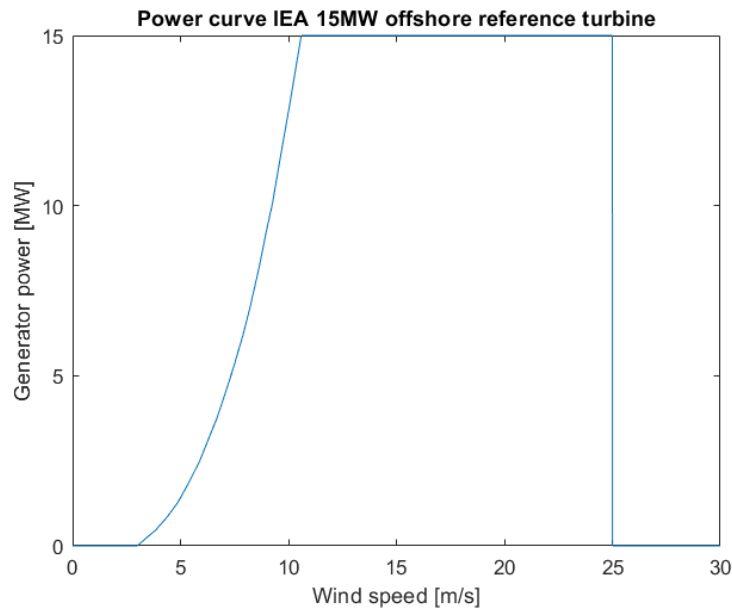
Figure C.3: Power curve IEA 15MW offshore reference turbine [53]

Table C.5: $15MW$ reference turbine general properties

Rated power [MW]	15
Rated wind speed [m/s]	10.4
Speed range [rpm]	5.5-7.6
Optimal tip speed ratio [-]	9.2
Peak power coefficient [-]	0.498

Blades

Table C.6 provides an overview of the blade properties of the $15MW$ reference turbine. Note that the airfoils are numbered, the specific airfoil coordinates and properties can be found in the IEA GitHub repository [2] in 'IEA-15-240-RWT/OpenFAST/IEA-15-240-RWT/Airfoils/'. The composite material of the blades is considered to be the same as for the $5MW$ reference turbine.

---

[2]`https://github.com/IEAWindTask37/IEA-15-240-RWT`

Table C.6: 15*MW* reference turbine blade properties

| Radius [m]	Chord [m]	Twist [Degree]	Airfoil	Mass density [kg/m]	Flapwise stiffness [Nm^2]	Edgewise stiffness [Nm^2]
1.5000	5.2000	15.5946	Cylinder 1	3180	1.5253e+11	1.5241e+11
2.3400	5.2083	15.5911	Cylinder 1	3050	1.3961e+11	1.3719e+11
4.6800	5.2357	15.4281	02	2920	1.2398e+11	1.2119e+11
7.0200	5.2889	14.9867	03	2640	1.0323e+11	1.0306e+11
9.3600	5.3606	14.3216	04	2300	8.1628e+10	8.4366e+10
11.7000	5.4433	13.4875	05	2000	6.1775e+10	6.8627e+10
14.6250	5.5510	12.2907	06	1700	4.2747e+10	5.1347e+10
17.5500	5.6501	11.0223	07	1340	3.2373e+10	3.8985e+10
19.7770	5.7110	10.0746	08	1100	2.8273e+10	3.1953e+10
22.0040	5.7521	9.1945	09	855	2.4819e+10	2.6958e+10
24.2310	5.7672	8.4292	10	700	2.1956e+10	2.3761e+10
26.4579	5.7545	7.7771	11	620	1.9671e+10	2.2085e+10
28.6849	5.7026	7.1825	12	550	1.8052e+10	2.1066e+10
31.1324	5.6007	6.5270	13	515	1.6718e+10	2.0352e+10
33.5798	5.4632	5.8950	14	490	1.5450e+10	1.9962e+10
36.0273	5.3095	5.2942	15	470	1.4253e+10	1.9713e+10
38.4747	5.1488	4.7345	16	455	1.3012e+10	1.9135e+10
41.0566	4.9911	4.2005	17	455	1.1771e+10	1.8309e+10
43.6384	4.8498	3.7259	18	447	1.0631e+10	1.7266e+10
46.2203	4.7276	3.3070	19	435	9.6129e+09	1.6059e+10
48.8021	4.6047	2.9200	20	425	8.6322e+09	1.4703e+10
51.3840	4.4821	2.5610	21	413	7.6702e+09	1.3064e+10
53.6887	4.3738	2.2620	22	395	6.8502e+09	1.1618e+10
55.9934	4.2673	1.9803	23	383	6.0805e+09	1.0231e+10
58.2981	4.1630	1.7136	24	371	5.3772e+09	8.9572e+09
60.6028	4.0617	1.4580	25	360	4.7536e+09	7.8812e+09
62.9076	3.9635	1.2156	26	345	4.2082e+09	6.9454e+09
65.2601	3.8669	0.9879	27	333	3.7188e+09	6.0485e+09
67.6127	3.7730	0.7751	28	322	3.2788e+09	5.2139e+09
69.9652	3.6813	0.5754	29	306	2.8855e+09	4.4368e+09
72.3177	3.5907	0.3802	30	295	2.5337e+09	3.7594e+09
74.6703	3.5008	0.1860	31	278	2.2205e+09	3.1919e+09
76.9023	3.4151	-0.0019	32	268	1.9443e+09	2.7603e+09
79.1342	3.3288	-0.2033	33	257	1.6797e+09	2.4551e+09
81.3662	3.2416	-0.4253	34	246	1.4338e+09	2.2325e+09
83.5981	3.1551	-0.6835	35	229	1.2064e+09	2.0242e+09
85.8301	3.0695	-0.9819	36	222	996610000	1.8140e+09
88.0621	2.9840	-1.2832	37	194	817140000	1.6088e+09
90.2940	2.8980	-1.5752	38	176	665040000	1.4098e+09
93.6000	2.7682	-1.9369	39	140	476310000	1.1404e+09
95.7938	2.6796	-2.1076	39	121	371310000	870060000
97.9875	2.5882	-2.1666	39	102	289390000	704190000
100.1813	2.4939	-2.1761	39	90	226410000	550740000
102.3750	2.3974	-2.1612	39	82	172310000	430150000
104.5688	2.2986	-2.1185	39	73	127010000	340100000
106.7625	2.1977	-2.0489	39	65	89341000	269690000
108.9563	2.0947	-1.9514	39	52	59192000	208350000
111.1500	1.9895	-1.8152	39	42	36186000	151880000
114.0750	1.8483	-1.5679	39	28	15636000	88937000
120	0.5000	-1.2424	39	10	188850	1920700

Tower

Table C.7 shows the tower dimensions of the $15MW$ reference turbine with a hub height of $150m$.

Table C.7: $15MW$ turbine tower dimensions

Height [m]	Diameter [m]	Wall thickness [m]
0	10	0.0411
28	10	0.0395
41	9.9260	0.0365
54	9.4430	0.0338
67	8.8330	0.0322
80	8.1510	0.0307
93	7.3900	0.0291
106	6.9090	0.0272
119	6.7480	0.0240
132	6.5720	0.0208
144.5820	6.5000	0.0240

Nacelle

Figure C.4 shows the nacelle properties of the $15MW$ reference turbine. The most important parameters are the hub mass of $190,000kg$ and the nacelle mass of $630,888kg$ with a tilt angle of $6°$.
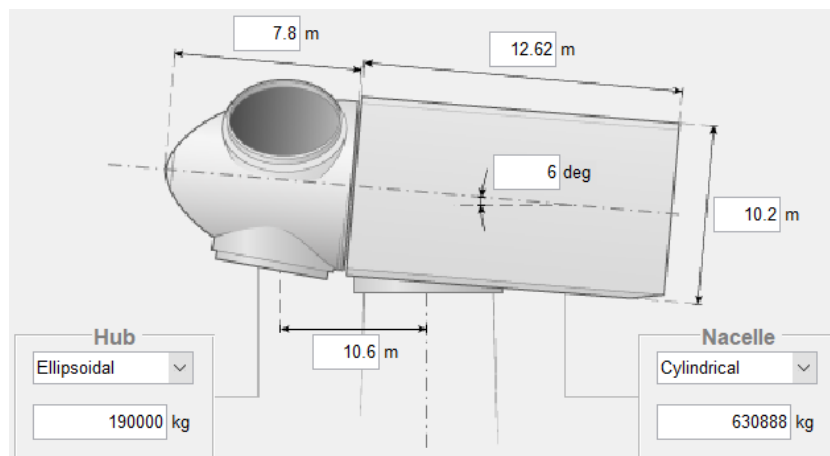
Figure C.4: Nacelle properties of the $15MW$ reference turbine

Control

For the control parameters, a cut-in wind speed of $3\frac{m}{s}$ and a cut-out wind speed of $25\frac{m}{s}$ are specified. All other relevant control parameters are summarised in table C.8. This wind turbine uses pitch control with a PI controller and constant gain as well as a 2nd order low-pass filter. The brake is located on the high speed shaft. Indices A, B, B2 and C relate to the control regions.

Table C.8: 15MW reference turbine control parameters

Pitch control	
Fine pitch angle [deg]	0
Max. pitch angle [deg]	90
Min. pitch angle [deg]	-2
Max. pitch rate [deg/s]	2
Min. pitch rate [deg/s]	-2
Start-up pitch angle [deg]	45
Start-up pitch rate [deg/s]	1
Speed for start-up [rpm]	0.25
Low pass filter cut-off frequency [rad/s]	1.0081
Kp [-]	-0.6402
Ki [-]	-0.0862
Torque control	
Demanded torque [Nm]	19624047
Torque minimum [Nm]	200
Torque limit [Nm]	21586451
Torque slew rate [N]	15000
Generator speed, A [rpm]	5
Generator speed, B [rpm]	5.5
Generator speed, B2 [rpm]	7
Generator speed, C [rpm]	7.56
Optimal mode gain [(Nm)/(rad/s)^2]	30221700
Generator speed low-pass cut-off [rad/s]	1.0081
Brake	
Brake torque [Nm]	28116
Deploy time [s]	0.6
Delay [s]	1.5

Drive train

The drive train of the 15MW reference turbine consists of a generator with an efficiency of 96.55% and an inertia of $3222631 kg m^2$. It is a direct drive generator so no gearbox is present (gearbox ratio=1).

C.3. FAST outputs
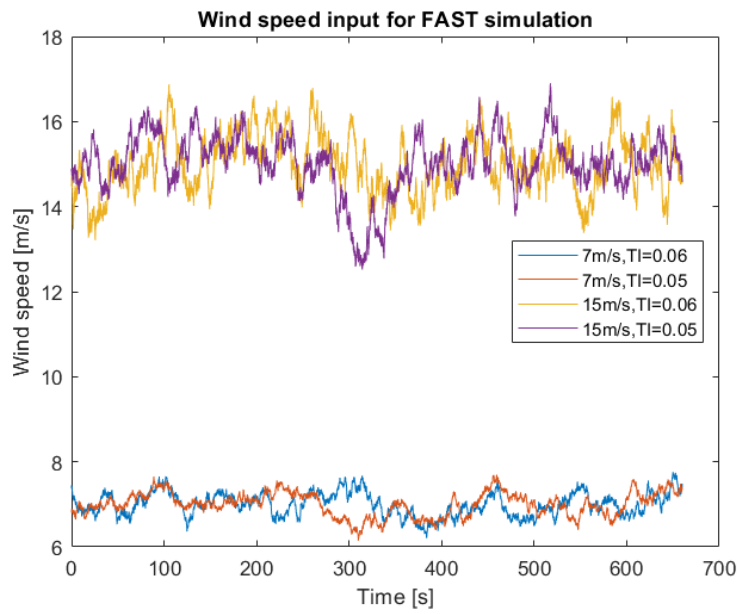
Figure C.5: Wind speed input in FAST
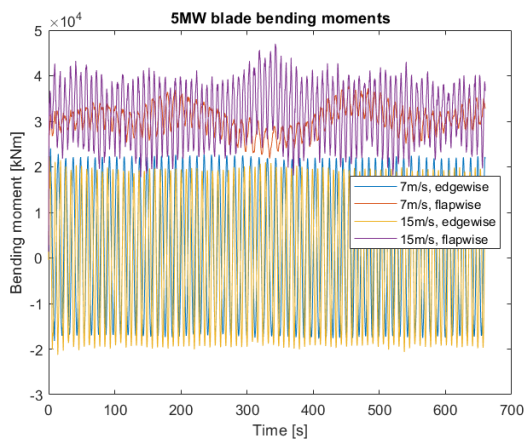
Figure C.6:
Blade root bending moment of 5MW reference turbine
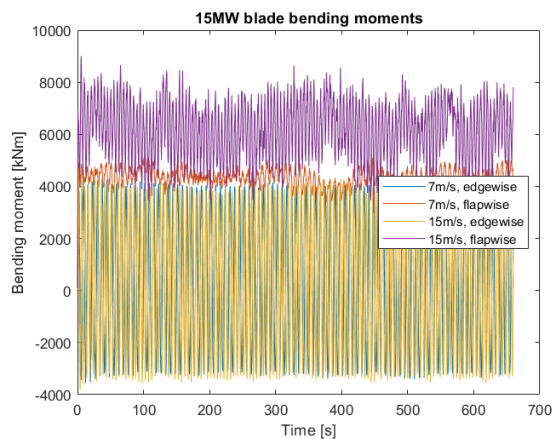
Figure C.7:
Blade root bending moment of 15MW reference turbine
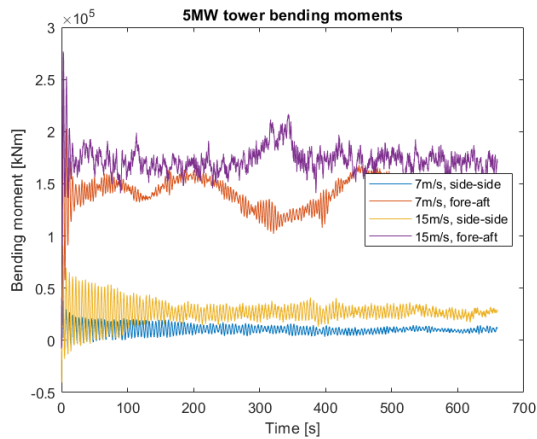
Figure C.8:
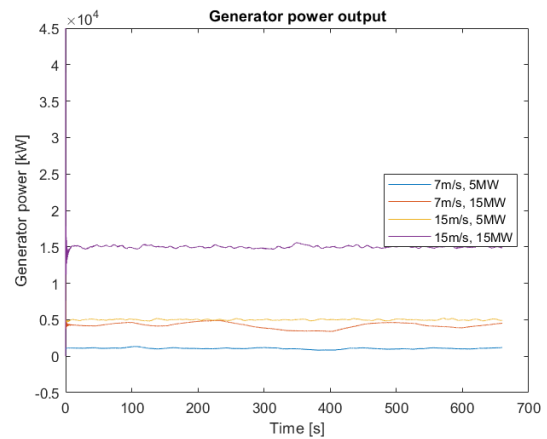Tower base bending moment of 5MW reference turbine
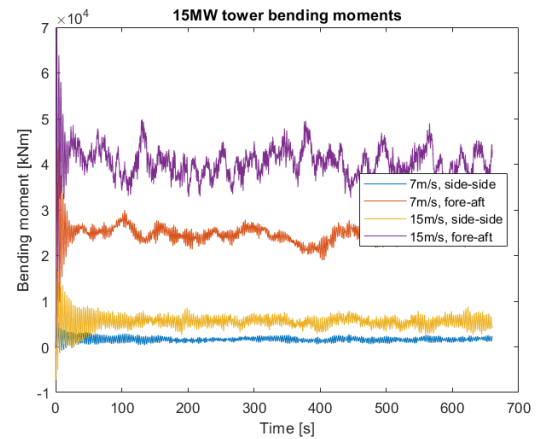
Figure C.9:
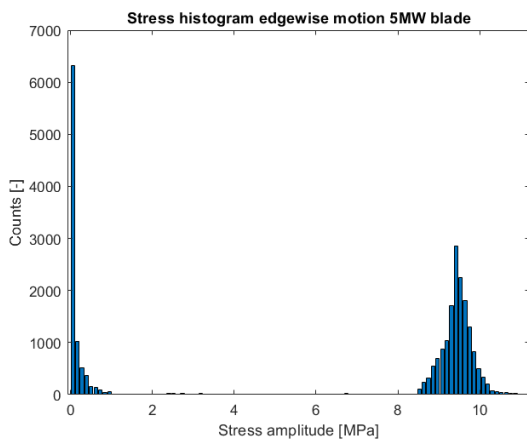Tower base bending moment of 15MW reference turbine
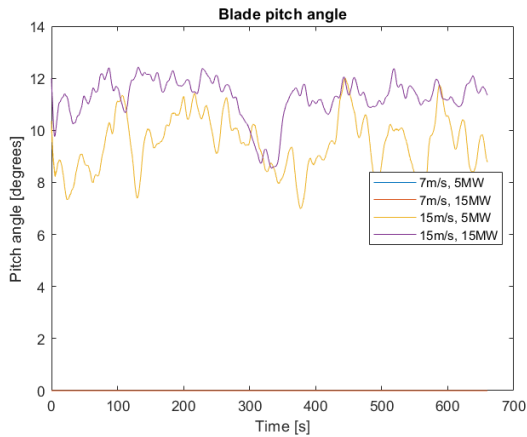
Figure C.10:
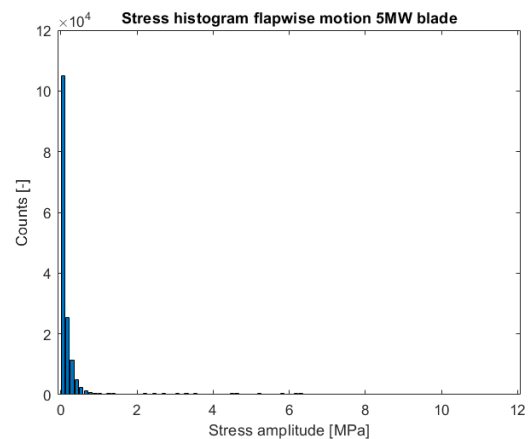Blade pitch angle response in FAST simulation
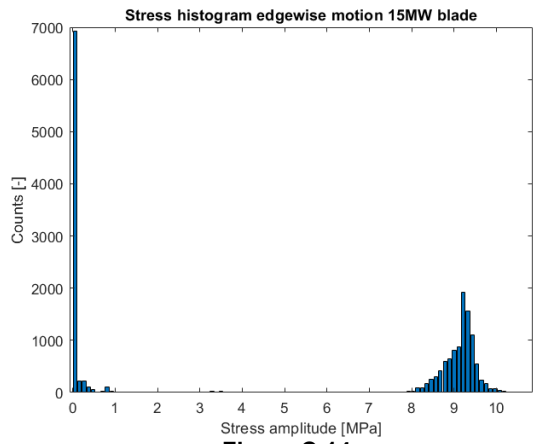

Figure C.11: Generator power output in FAST simulation
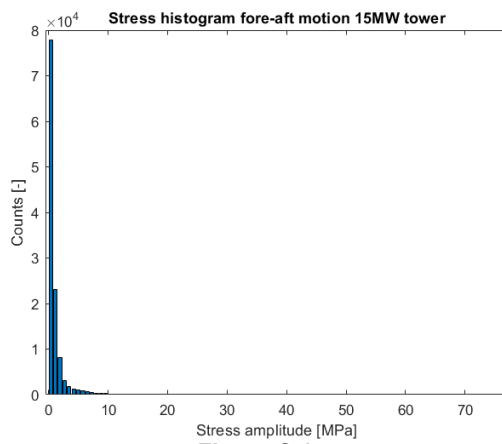
C.4. Stress histograms

Figure C.12:
Stress histogram of 5MW blade edgewise motion

Figure C.13:
Stress histogram of 5MW blade flapwise motion

Figure C.14:
Stress histogram of 15MW blade edgewise motion
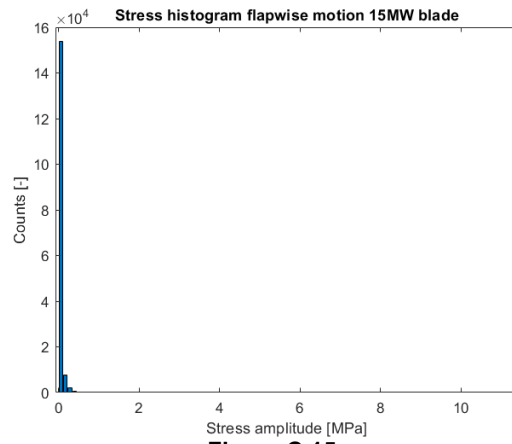
Figure C.15:
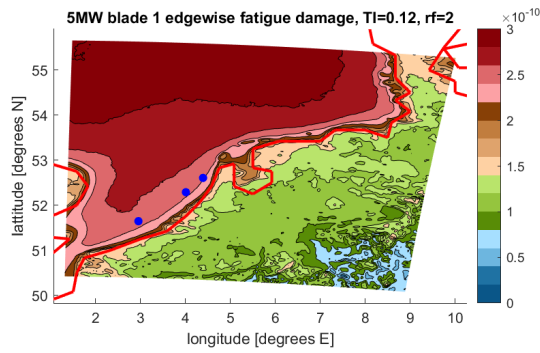Stress histogram of 15MW blade flapwise motion
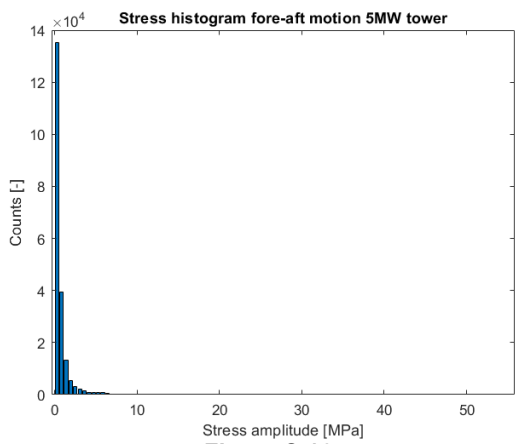
Figure C.16:
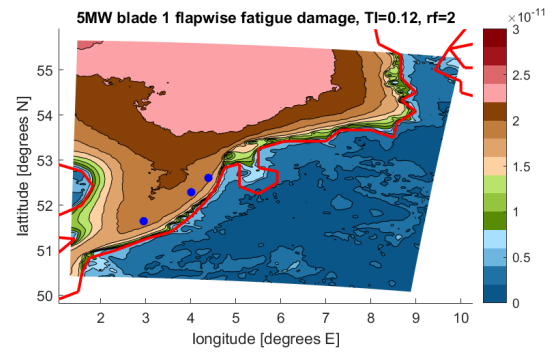Stress histogram of 5MW tower fore-aft motion

Figure C.17:
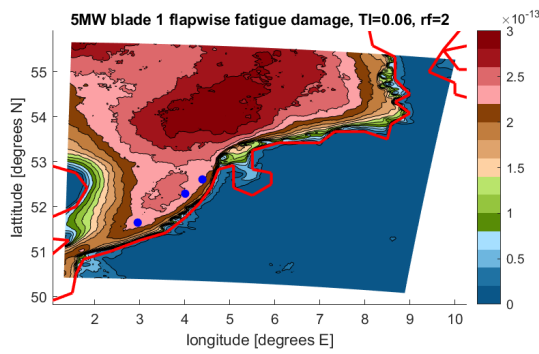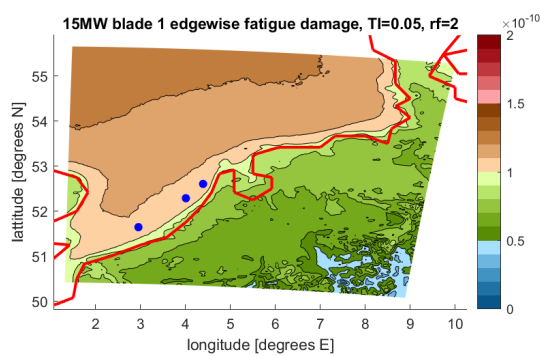Stress histogram of 15MW tower fore-aft motion

C.5. Fatigue contour plots

Figure C.18: Edgewise
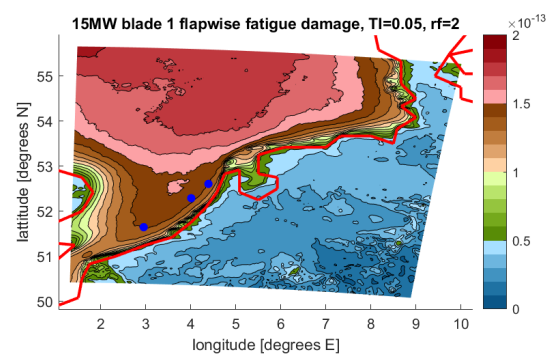fatigue damage of $5MW$, simple rainflow, 12% TI

Figure C.19: Flap-wise
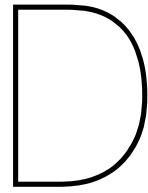fatigue damage of $5MW$, simple rainflow, 12% TI

Figure C.20: Flap-wise
fatigue damage of $5MW$, simple rainflow, 6% TI

Figure C.21:
Edgewise fatigue damage of $15MW$, simple rainflow

Figure C.22:
Flapwise fatigue damage of $15MW$, simple rainflow

D

Assumptions

D.1. Stability

- The Obukhov length does not change with height for a certain location
- All non-discarded shear exponent values follow the power law wind profile
- No local perturbations in the wind speed profile due to obstacles such as trees or wind farms are present

D.2. Energy yield

- The density correction assumes dry air
- In the calculation of the rotor equivalent wind speed, it is assumed that the wind speed in each section corresponds to the wind speed of that entire section
- The turbulence intensity found for the three wind farm locations applies to the full DOWA domain
- There is no downtime due to e.g. maintenance or failure
- The wind speed data for every direction sector follows a Weibull distribution

D.3. Fatigue

- The fatigue damage of each cycle can be linearly added to the total accumulated lifetime damage (Miner's rule)
- The FAST simulations using the NTM model assume a power law wind profile with a shear exponent of $\alpha = 0.2$
- In the simple rainflow counting algorithm, a full load cycle is assumed for each stress amplitude found
- The material of the blade root of both wind turbines is SNL Triax
- Composite materials do not have a fatigue limit
- The 10-minute damage fraction is $\frac{1}{6}^{th}$ of the hourly damage fraction
- Each blade experiences the same loads over its lifetime
- The fatigue damage accumulated during power production under normal operating conditions only is representative for the total lifetime fatigue damage
- The fatigue damage accumulated for wind speeds of $3\frac{m}{s}$ can be neglected